MASTER THESIS

Ultrasound-based navigation for surgical removal of liver lesions

A feasibility study of MRI-ultrasound fusion in the operation theatre

Jasper Namle Smit

A thesis submitted in fulfillment of the requirements for the degree of Master of Science

in

Technical Medicine with the track Medical Imaging and Interventions
Faculty of Science and Technology (TNW)

September 5, 2017

Graduation Committee

Chairman and clinical supervisor:	prof. dr. T.J.M. Ruers Department of Surgery, NKI-AVL, Amsterdam Professor Oncology and Biomedical Imaging, University of Twente, Enschede
Technological supervisor:	dr. ir. F. van der Heijden Department of Robotics and Mechatronics University of Twente, Enschede
Mentor:	drs. B.J.C.C. Hessink-Sweep Department of Technical Medicine University of Twente, Enschede
Additional member:	dr. O. Ivashchenko Department of Surgery, NKI-AVL, Amsterdam
External member:	prof. dr. S. Misra Department of Biomedical Engineering University of Twente, Enschede

University of Twente

Abstract

Master of Science

Ultrasound-based navigation for surgical removal of liver lesions

by Jasper Namle Smit

Surgical navigation is needed for precise localization of liver lesions and the surrounding structures, however, conventional navigation is not applicable. While preoperative surgery plans based on preoperative imaging give detailed information about the patient-specific anatomy, this is not up-to-date in the intraoperative situation due to flexibility and deformation of the liver. Therefore, navigation for liver surgery requires real-time fusion of preoperative surgery plans and MR scans with intraoperative ultrasound. In this thesis, the goal was to determine the feasibility of ultrasound-based navigation for surgical resection of liver lesions. For that purpose, the PercuNav co-registration ultrasound system was used.

For this thesis, a deformable multimodal liver phantom was developed to test MR-US co-registration. Raw data analysis of the used co-registration software was impeded, hence alternative accuracy assessment methods have been developed. With and without deformation, this resulted in registration errors of 5-10 mm in the -2 and +2 cm areas around the registration center after point-based registration. Similar registration errors were achieved in *ex vivo* environments. In these experiments, three resected liver specimens with multiple lesions were used. Point-based registration showed good matching of the tumor regions between MR and US images. Deformation of the specimens due to a lack of blood flow and vessel collapse made further analysis difficult. Automatic detection of points for co-registration accuracy assessment was tested to replace manual point selection. The SIFT-based algorithm that was developed, was not sufficient between these modalities.

Due to logistical limitations, intraoperative introduction of the setup was performed once. Possible benefits have been demonstrated in the case of vanishing and isoechoic lesions, as well as restrictive limitations of the current setup. A different transducer, EM field generator, co-registration method and image interface are preferred. These factors are taken into account for the development of an in-house system, for which development steps are described.

It is concluded that ultrasound-based navigation by means of electromagnetic tracking is possible and shows feasibility for its intraoperative introduction during open liver surgery. Further implementation was impeded by limitations of the used system. It is expected that a satisfactory accuracy of 5-10 mm in a 4.0x4.0x4.0 cm volume is feasible in the to-be developed system, just as in the used system during this thesis.

Acknowledgements

During an internship in my second master's year, my interests for the working field of surgical oncology increased. The ongoing studies in the NKI-AvL, where medical care and research form a powerful combination, perfectly match with my interests for medical technology. The opportunity to work in a multidisciplinary setting as this one, on a challenging project as this turned out to be, was something that turned my choice for an interesting graduation internship into an easy decision.

Assessing feasibility of this thesis' subject turned out to be an interesting task. Logistically, there have been a lot of challenges and therefore I am happy with the measurements that were accomplished in the end. I've learned a lot not only about several aspects which are involved in such a project, but also that such a work field is something I would like to proceed with in the future.

During this year-long internship, I was lucky to have Sasha Ivashchenko and Bas Pouw as my daily supervisors. Thanks for all the time you had to help me and make this a useful year for me, especially when things did not go as planned or hoped for. Bas, with your role as technical physician you've taught me a lot on how to act in the multidisciplinary settings. Sasha, especially your constructive feedback really put me into a lot of thinking and you have challenged me in so many ways. I thank Koert Kuhlmann for the clinical supervision during this project, you always had time to discuss project-related subjects but also regarding my development during this year. I want to thank Theo Ruers as head of the research group, for always being critical during the research meetings, for taking place as my chairman in the graduation committee and as replacing clinical supervisor. I want to thank Ferdi van der Heijden for the fruitful meetings we had. You have challenged me in several ways to become a more critical and better researcher. Bregje Hessink-Sweep, during the intervisions you always asked the right questions and let me and the other group members develop to our own needs. Next to that, I really appreciated the personal conversations we've had this year. Additionally, I look back at our group meetings as nice and meaningful for which I thank Else, Klaske, Lara and Eline.

Furthermore, I want to thank everyone who has contributed (even if it is just a little bit) to this fruitful year. Niels, Daan and Gerard, thank you: with you guys graduating at the same time, the internship became a lot more fun. Also, I want to thank my parents and my sister Lotte for their unconditional support for not only this graduation year but the past seven years, my friends for all the distracting fun and laughter, and Lieve for always being there.

Jasper Smit
September 2017

Contents

List of Figures

List of Abbreviations

CLM	Colorectal liver metastasis
CT	Computed tomography
DOF	Degrees of freedom
DoG	Difference of Gaussian
EBL	Effective blood loss
EM	Electromagnetic
EMTS	Electromagnetic tracking system
FG	Field generator
FDG	Fluorodeoxyglucose
FNH	Focal nodular hyperplasia
FOV	Field of view
FRE	Fiducial registration error
HCC	Hepatocellular carcinoma
IGLS	Image-guided liver surgery
LRE	Local registration error
MRI	Magnetic resonance imaging
MSER	Maximally stable extremal region
MWA	Microwave ablation
NDI	Northern Digital Inc.
NKI-AvL	Netherlands Cancer Institute – Antoni van Leeuwenhoek
PACS	Picture archiving and communication system
PET	Positron emission tomography
PFG	Planar field generator
PLUS	Public library for ultrasound
PVA	Polyvinyl alcohol
RFA	Radio frequent ablation
RMSE	Root-mean-square error
RTV	Room-temperature-vulcanization
SD	Standard deviation
SIFT	Scale-invariant feature transform
SCU	System control unit
SIU	System interface unit
SN	Surgical navigation
TPU	Thermoplastic polyurethane
TRE	Target registration error
TTFG	Tabletop field generator
US	Ultrasound

Chapter 1

Introduction

Summary

Relevant backgrounds on a medical and technical level are described in this chapter. As a clinical introduction, the current options in diagnostics and treatment options for patients with liver lesions are briefly discussed. Subsequently, the rationale for this thesis is elucidated. This brings us to the technical background which consists of several components relevant to the current treatment options and the research described in this thesis. Lastly, the goals of this thesis are listed.

1.1 Clinical Background

Local treatment of focal liver lesions in general, and colorectal metastases in particular, is complex and consists of different possibilities. Usually, a combination of systemic and focal treatment is used as approach. After describing diagnostic methods, the focal treatment options of liver lesions will be discussed, with a focus on surgical resection. Ultimately, the rationale behind this research is explained.

1.1.1 Liver Lesions

Focal liver lesions are divided into benign and malignant lesions. Most benign liver lesions, such as focal nodular hyperplasia (FNH), cysts, hemangiomas, and hamartomas, do not require treatment after coincidental finding during conventional diagnostics. In the case of liver adenomas, treatment might be needed if the lesion is of substantial size. In general, liver metastases are asymptomatic and found during diagnostics of a malignancy which has presented in other ways.

Malignant lesions in the liver can be divided in primary and secondary tumors. Primary malignant tumors, in the case of cholangiocarcinoma or hepatocellular carcinoma (HCC) in a non-cirrhotic liver, are often detected in an advanced stage after diagnosis with nonspecific abdominal complaints. However, the large majority of hepatocellular carcinomas occurs in patients with liver cirrhosis. Being secondary liver lesions, colorectal liver metastases are considered the largest group of tumors in the liver. In general, liver metastases are diagnosed during follow-up of a primary tumor occurring in 30-50% the patients suffering from colorectal cancer [1–3]. Most common sites of primary malignancy are carcinomas in the gastrointestinal tract via portal circulation, breast cancer, lung cancer, urogenital cancer or melanoma.

1.1.2 Options in Diagnostics

Diagnostics will be described for malignant liver lesions, since benign liver lesions are mostly coincidental findings during conventional diagnostics for other purposes. Diagnosis of a liver lesion consist of a detailed history, physical examination, radiological tests, and pathological assessment. While ultrasound is often chosen as first diagnostic tool because of being inexpensive, non-invasive and radiation free, contrast-enhanced magnetic resonance imaging (MRI) or contrast-enhanced computed tomography (CT) is advised to acquire afterwards for additional and complete assessment of the liver's anatomy.

For primary liver lesions, ultrasound is often used as first diagnostic tool. When a patient is clinically suspected with cholangiocarcinoma, an additional MRI or CT should be obtained. Patients with chronic liver disease, e.g., with cirrhosis as the final stage of liver fibrosis, are at a risk of development of HCC as a primary tumor. Also, ultrasound is used as first diagnostic tool here. When an ultrasound shows a lesion of >1 cm, an MRI or triple-phase CT should be obtained in these patients. Diagnosis of a HCC can be made if the lesion shows enhancement in the arterial phase with washout in the delayed venous phase, until otherwise proven.

For secondary liver lesions, contrast-enhanced CT is acquired as standard procedure for diagnosis of a primary tumor, e.g., in the case of a primary colorectal lesion. In general suspicion of liver lesions, MRI is additionally used. Next to that, fluorodeoxyglucose positron emission tomography in combination with CT (FDG-PET-CT), or chest CT can be acquired, to demonstrate potential extrahepatic tumor activity and therewith indicate a change of treatment. FDG-PET is not considered as a primary diagnostic tool due to limited resolution for small lesions (<1 cm).

In this institute, protocols of a diagnostic MR scan of a patient with liver lesions are performed with multi-phase MR sequences with a gadolinium-based liver-specific contrast agent gadoxetic acid (Gd-EOB-DTPA, Primovist) [4–6]. The multiphase contrast-enhanced mDIXON sequence for this dynamic MR scan was optimized in the Netherlands Cancer Institute - Antoni van Leeuwenhoek (NKI-AvL) and is used as a routine diagnostic liver scan for detection of liver tumors [7]. This sequence consists of five consequent phases that are acquired during the early stage of contrast's filtration and one late phase showing the hepatocytes-specific filtration of the contrast at 20 minutes post injection (p.i.). Scans of the different phases are acquired as follows: blanco, early arterial, later arterial, portal venous, late venous and 20 minutes p.i., with each scan acquired in controlled breath-hold in expiration for 12 seconds (Figure 1.1). Especially in the case of colorectal metastases, MRI is preferred over CT thanks to a better detection of lesions <10 mm. Next to clear visualization of portal and hepatic veins and small lesions, large bile ducts and arteries can be detected.

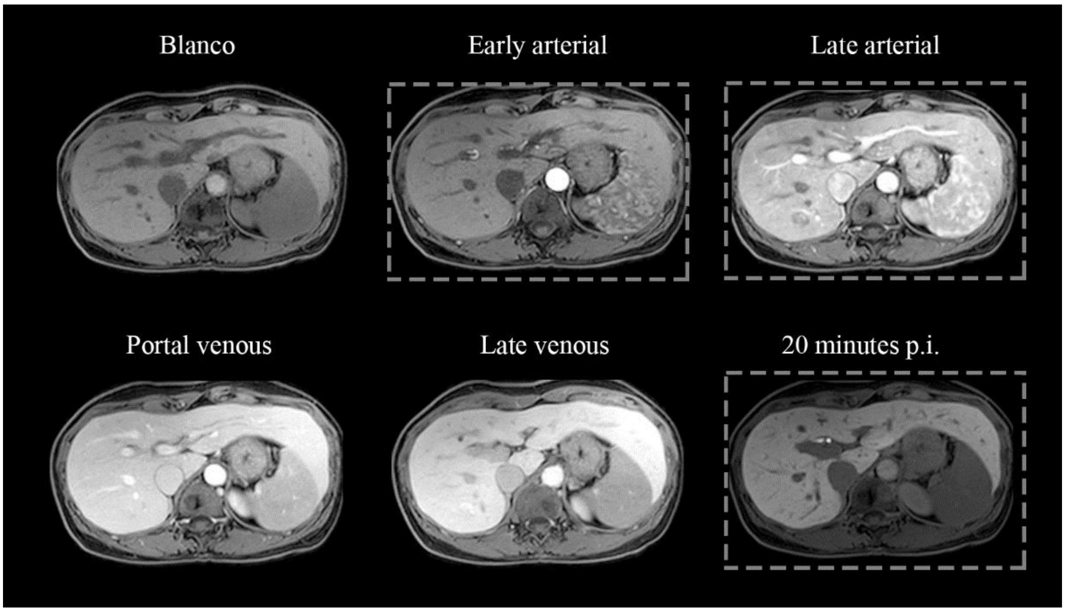

FIGURE 1.1: All phases of the diagnostic multi-phase MR liver scan acquired with the liver-specific contrast agent used as a routine diagnostic liver scan for detection of liver tumors. The dynamic frames that are required for segmentation of the liver, with hepatic vasculature and biliary anatomy are depicted with gray frames.

1.1.3 Treatment Options

Depending on the exact location and stage of the tumor, there are various options for treatment plans including surgery, local radio frequency ablation (RFA) or microwave ablation (MWA) and neoadjuvant therapy.

Neoadjuvant treatment is a powerful instrument that contributes positively to the total survival of patients with colorectal cancer [8]. It can be used to downstage the patient or convert patients with non-resectable metastases into resectable ones [9, 10]. A small number of patients receiving neoadjuvant treatment show complete radiological disappearance hence so-called "vanishing lesions" [11, 12]. Nonetheless, a large majority of these patients still receive local treatment.

In the last decade, techniques for local treatment of the disease (RFA and MWA) and minimally invasive surgery are achieving more acceptance [13–16]. These procedures can take place percutaneously, performed by interventional radiologists. Nevertheless, laparotomy might be preferable considering the tactile feedback, organ mobilization, vascular control, parenchymal transection and better accessibility in cases of difficult tumor localization [17, 18]. RFAs and MWAs can be performed during surgical interventions as well, when multiple lesions are present and require different approaches.

In general, the most effective treatment of liver lesions is surgical removal and is therefore preferred as "gold standard". Thanks to the regenerative ability of the liver, 80% of the liver can be resected if the remaining parenchyma is optimal, with a sufficient inflow and outflow [19]. It is important to have insights in the relation between the resectable region and its bile and vessel structures, in afferent (portal) and efferent (hepatic) vessels. Defined by Couinaud, the bile and vessel structures divide the liver in eight segments, in a left (segments II, III and IV) and right lobe (segment V, VI, VII and VIII; Figure 1.2). Segment 1, the caudate lobe, is considered as a separate entity. One speaks of anatomical resection when a resection is performed according to the anatomical boundaries of these segments. A non-anatomical resection, or wedge resection, can be performed if a lesion is situated at the edge of the parenchyma and if vascularization and gall drainage are not endangered. The decision to perform this type of resection depends on factors as preoperative chemotherapy, pre-existing liver disease, risk of recurrence and the tumor burden [20].

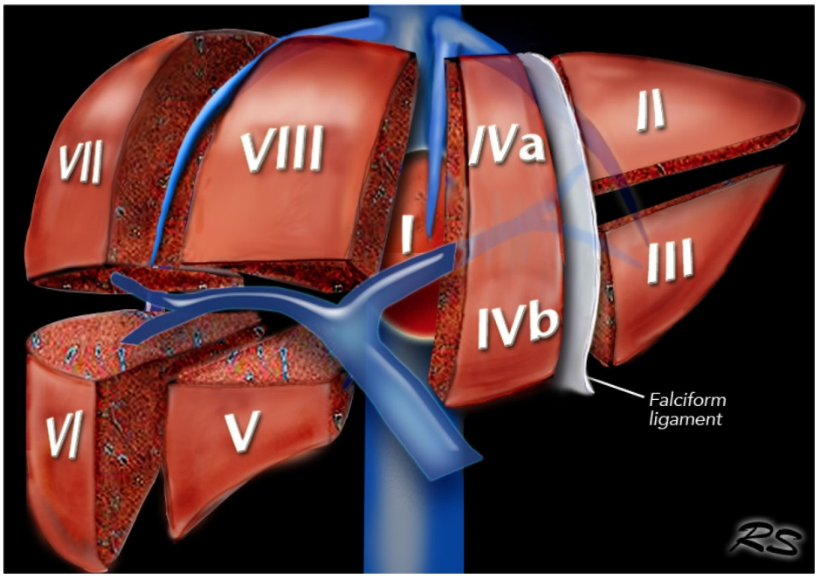

FIGURE 1.2: Segmental anatomy according to Couinaud. Image reproduced from The Radiology Assistant [21].

Blood loss and the extent of liver tissue resection are two large contributing factors to influence the postoperative outcome from hepatic resection [22]. Shortly, these two factors will be described.

To limit the effective blood loss (EBL) during surgical resection, different techniques are available. First of all, anesthetic actions should restrict the blood inflow into the liver by prevention of overfilling of the patient. Additionally, portal triad clamping (or the Pringle manoeuver) limits the inflow, by temporarily applying a clamp on the portal vein and the hepatic artery. This technique is preferably not performed due to several postoperative complications [23]. If necessary, different approaches can be chosen for this manoeuver, i.e., continuous and intermittent (with periods of reperfusion). Another method for reducing blood loss is total hepatic vascular exclusion, in which temporary occlusion of hepatic vessels limits retrograde hepatic vein bleeding. However, negative hemodynamic effects and postoperative complications are hereby induced [24, 25]. A third option to limit EBL, intrahepatic pedicle ligation can be performed. This involves ligating the branch that supplies the liver portion that is planned for resection. Once the required portal pedicle clamped, a vascular stapler is used to transect this pedicle therewith inhibiting further blood flow for that part of the liver.

After blood flow is restricted in one of the described ways, parenchymal transection can take place. For this, a variety of suture ligation, bipolar electrocautery, vessel sealing devices and vascular clips can be used.

Ultrasonic dissection is used to divide liver parenchyma by combining ultrasonic energy with powerful aspiration, e.g., in this institute with the Cavitron Ultrasonic Surgical Aspirator (CUSA, Tycho Healthcare, Mansfield, MA, USA). Skeletonization is in this way performed, exposing the blood vessels and biliary structures that subsequently can be divided. For that purpose, sealing devices can be used. Sealing devices aim at sealing small vessels before division, therewith combining parenchymal division with vessel hemostasis. This leads to usability in non-anatomical or laparoscopic resections. Sealing can take place in forms of bipolar vessel sealing, saline-linked radiofrequency sealing, water-jet dissection and vascular stapling.

When surgical resection of a lesion is impossible due to positioning, e.g., adjacent to the vena cava, ablation techniques can be used to locally treat a lesion with curative intents. Ablation minimizes loss of healthy liver parenchyma, and can be useful in patient with minimal liver function or in cases of bilobar disease [26]. In this institute, RFA and MWA are used in laparoscopic and open approach. In the case of RFA, radio frequent radiation (in the range of 350-500 KHz) generates heat at the tip of an ablation probe. This heat causes coagulation and therewith necrosis in a spherical region of 5 cm at maximum. In MWA, local hyperthermia is created by applying a local EM field (300 MHz – 300Ghz) that causes frictional heating, due to oscillation of polar molecules.

Other treatment possibilities consist of stereotactic radiotherapy, vascular treatment as trans arterial chemo embolization and radio embolization. These techniques will not be described because focusing on surgical options.

1.1.4 Rationale for This Research

Precise localization of the lesions and detailed knowledge of the patient-specific vascular and biliary structures helps to prepare for complex liver surgeries, it also contributes to successful surgical resections of tumors, with higher preservation of functional liver tissue [27–29]. Thus, in this institute, the surgeon is regularly provided with a detailed three-dimensional (3D) model of the organ's anatomy. This 3D model, based on pre-operative contrast-enhanced computed tomography or magnetic resonance imaging, is reconstructed in a virtual planning environment. However, applying the preoperatively constructed model into supportive use during surgery remains a difficult fulfillment.

The liver has a high natural mobility and flexibility, and its shape is significantly affected by deformation due to mobilization during open surgery [30, 31]. This causes a difficult correlation of the 3D model to the intraoperative situation to the preoperative 3D model which is based on breath-hold CT or MRI. In open liver surgery, surgeons sometimes spend a lot of time on exploring to find lesions. This increases total surgery time, leading to potential harm for the patient along with increased costs. Furthermore, sometimes incorrect ablations are performed in the case of small or vanished lesions. Hence, surgical navigation in liver resection is needed.

Image-guided navigation surgery aims at providing the surgeon with detailed real-time information of the surgical site. In the case of oncological procedures, contribution to a negative tumor resection margin is desired by connecting preoperative anatomical information to the real-time anatomical situation of the patient during surgery. Surgical navigation (SN) is already implemented in diverse applications, such as orthopedics, facial surgery and neurosurgery [32–36]. However, implementation of SN applicable to highly-deformable organs is still scarce. For liver surgery, surgical navigation can take place either solely based on preoperative images (e.g., MR and CT) either solely based on real-time intraoperative imaging (e.g., US), or, alternatively, based on fusion of images from pre- and intraoperative modalities.

Conventional navigation systems, solely based on preoperative data, are not suitable for liver surgery due to intraoperative deformation of the organ as a whole. No rigid alignment of the preoperative planning with the intraoperative situation can be performed when the whole organ is used for registration.

Real-time image-guided liver surgery (IGLS) is desired since the preoperative situation has presumably changed or has been influenced by preoperative chemo- or radiation therapy. Intraoperative 3D ultrasound has been used routinely for tumor localization as a helpful addition in liver resection [37]. However, the use of solely US for image-guidance can be difficult. Target lesions may not be visible, or the imager may not be confident that a lesion identified with US corresponds with the lesion identified with CT or MRI. Furthermore, isoechoic or vanishing lesions are not visible on US images as well as arteries and bile ducts.

To elaborate the previously described features, the surgeon wants to be able to distinguish critical anatomical structures such as the bile ducts, main hepatic or portal veins and hepatic arteries in the area around the lesion. Possible complications after RFA or hepatectomy, which ideally should be prevented, are adverse arterial bleeding, biloma or bile duct injury due to the anatomical variation of the biliary system and its limited real-time information [38–40]. Arterial structures can be extracted from multi-phase CT acquisition; however, this requires an additional CT scan with unwanted radiation exposure. Since biliary anatomy is not visible on CT scans except for extreme cases of dilated bile ducts, non-ionizing contrast-enhanced MRI is desired to extract all required anatomical liver information. Arterial and biliary structures can be distinguished in multi-phase MR liver imaging, resulting in scans with clear localization of main bile ducts, the correct location and size of small lesions and the location of main arteries and veins.

When we take all aforementioned challenges into account, it is evident that navigation for liver surgery requires real-time fusion of preoperative surgery plans (based on MR) with intraoperative ultrasound. Fusion of these images is already possible to a certain extend when non-linear soft tissue deformation is not taken into account [41, 42]. While rigid registration of intraoperative imaging with the preoperative planning data is considered as not feasible due to non-rigid deformation of the organ as a whole, expected is that with careful and controlled mobilization a rigid alignment of preoperative data can give satisfactory accuracy for the local navigation [28].

In this institute, a new era has started with the implementation of surgical navigation on an electromagnetic (EM) tracking based system. In this institute, this navigation is applied during pelvic surgery where anatomical structures are assumed as rigid [43, 44]. Further application of this system is currently being researched in this institute in fields such as colorectal and head-neck-surgery, from now on as well in liver surgery. Question is if this navigation surgery is applicable when we take the problems of liver deformation into account. In this institute, we have the possibilities to use the PercuNav Ultrasound system from Philips for research properties that is currently available in the department of radiology. PercuNav has image fusion and navigation capabilities and is currently used for percutaneous liver biopsies and percutaneous ablation of liver lesions [45]. The aim of this research is to assess the feasibility and the potential added value of ultrasound-based navigation, with help of PercuNav in particular, for open liver surgery.

1.2 Technical Background

Information from preoperative imaging is desired to take into account during surgery. For that, navigation technology is used for which technological background is provided. Specific implementation techniques in this institute are described that are useful for ultrasound-guided navigation during surgery, as well as current options in ultrasound-guided navigation techniques. Subsequently, options for accuracy assessment of image co-registration are outlined.

1.2.1 Electromagnetic Navigation Tracking

For liver surgery, surgical navigation can take place in three different ways, i) solely based on preoperative images such as MR or CT, ii) solely based on real-time intraoperative imaging such as US, or, alternatively, iii) based on fusion of images from pre- and intraoperative modalities. Because the first two approaches, fully preoperative or real-time images based systems, are not suitable for navigation in open liver surgery, our focus will be on the third method.

We focus on combination of preoperative information with the real-time intraoperative situation. To accomplish this, we need a tracking system that provides a link between preoperative and intraoperative situation. Tracking can be performed based on optical tracking or electromagnetic tracking of a sensor with a known relation to the target area. Tracking of an optical sensor requires a direct line-of-sight between the operating field and the camera system which is a problem in cluttered operating theaters. On the other hand, the use of ferromagnetic surgical equipment influences the accuracy and the application of EM tracking [46]. In this work, we will use the Aurora electromagnetic tracking systems (EMTS; Northern Digital Inc. [NDI], Waterloo, Ontario, Canada) that are available in this institute. Two types of field generators will be used for application concerning the liver (Figures 1.3, 1.4). The planar field generator (PFG) is mounted on a flexible positioning arm. The tabletop field generator (TTFG), which is suitable for placement underneath the patient for less interference in the surgical field, is slid inside a Perspex casing positioned underneath the patient's mattress [47, 48]. Both field generators generate an electromagnetic field with a pre-determined field of view (FOV; Figures 1.3, 1.4). Within the FOV, multiple EM sensors with five or six degrees of freedom (5DOF/6DOF) can be tracked. The field generator produces a constant magnetic field. Field sensors have weak currents passing through them. Currents in the sensors induce electromagnetic induction when they move inside the EM field. The sensors, in tips of devices or fiducials placed on the patient, calculate their locations by iteratively measuring the magnetic induction vector produced from the field generator. In this way, sensor positions are determined in relation to the field generator [49]. Electrical signals from the sensors are amplified and digitized by a system interface unit (SIU) and are connected with the host computer of the system through a system control unit (SCU).

1.2.2 MR-US Registration

For fusion of US and MR data and for EM navigation, it is important to realize that these images and the EM data each have their own coordinate systems that must be registered.

In the MR scan, the xy-plane is set as the axial transection leaving the z-axis orientated in the direction from caudal to cranial. The three-dimensional coordinate system of the MR scan is Cartesian (x, y, z). Herein, any point in three-dimensional space is specified with signed distances to the point from three mutually perpendicular directed lines, measured in the same unit of length.

The coordinate system from the EM field generator is Cartesian as well. However, orientations of the axes and positions of origins are different. Unlike in the MR scan, z-axis of the WFG is orthogonal to the opening of the generator and is not aligned with the longitudinal axis of the

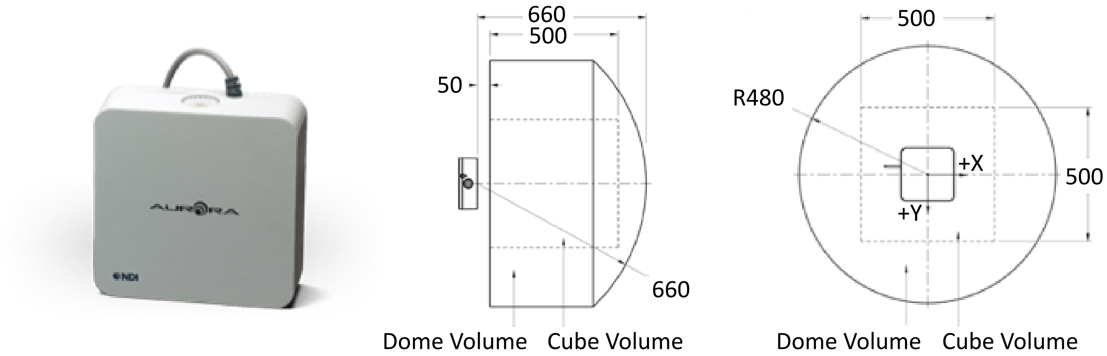

FIGURE 1.3: On the left side the planar field generator, with on the right its characteristic field of view (dimensions in mm) [47].

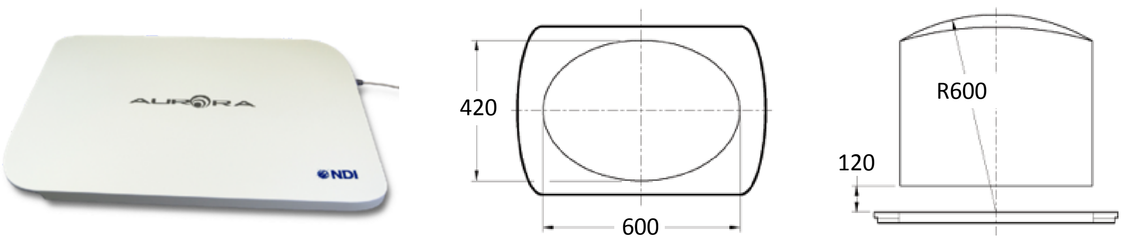

FIGURE 1.4: On the left side the table top field generator, with on the right its characteristic field of view (dimensions in mm) [47].

human body. Transformation between this coordinate system and the MR coordinate system is linear if expressed in homogeneous coordinates.

In contrast to the EM and MR systems, coordinate systems of 2D ultrasound are given in cylindrical coordinates (r,θ, z). In 2D US, any point in the scanning plane is defined at a radial distance r with an angular coordinate θ. Height in the partially cylindrical volume is defined by z. (Figure 1.5).

Fusion of two modalities is possible when the spatial link is provided with the EM tracking. The first step in co-registration requires calculation of the transformation matrix between the systems with rotations and translations, to correctly describe the spatial relation between the datasets. For this, several methods are available. First of all, a set of registration points can be defined in the ultrasound images as well as the preoperative imaging volume on common anatomical structures or fiducials. Calculating the translation and rotation between these sets of points leads to a transformation matrix. Second, plane-based registration can take place after assigning a plane from the US image to a plane in the MR volume. The transformation matrix between these images determines the image registration. While the point-based and plane-based registrations are performed manually, a third, an automatic co-registration can be performed based on vessel extraction in both modalities.

Several steps of calculation are necessary to determine a correct co-registration, visualized in Figure 1.5. One EM sensor is attached at the region of interest as reference, being the patient reference (5DOF) tracker, while another EM sensor is clipped on and calibrated on the US probe. Transformation from the US image (US) to the tracked US transducer (PR) is denoted as

${}^{PR}\mathbf{T}_{US}$. The relation between the tracked probe and the reference is established by continuously updating the transformation matrix ${}^{EM}\mathbf{T}_{PR}$. Now, image registration is performed by linking the preoperative MR volume to the EM field. Ultimately, this transforms a point ${}^{US}\mathbf{p}$ in the initial ultrasound image to the updated position ${}^{MR}\mathbf{p}$ in the transformed MR volume:

$$ {}^{MR}\mathbf{p} = {}^{MR}\mathbf{T}_{EM} \cdot {}^{EM}\mathbf{T}_{PR} \cdot {}^{PR}\mathbf{T}_{US} \cdot {}^{US}\mathbf{p} \tag{1.1} $$

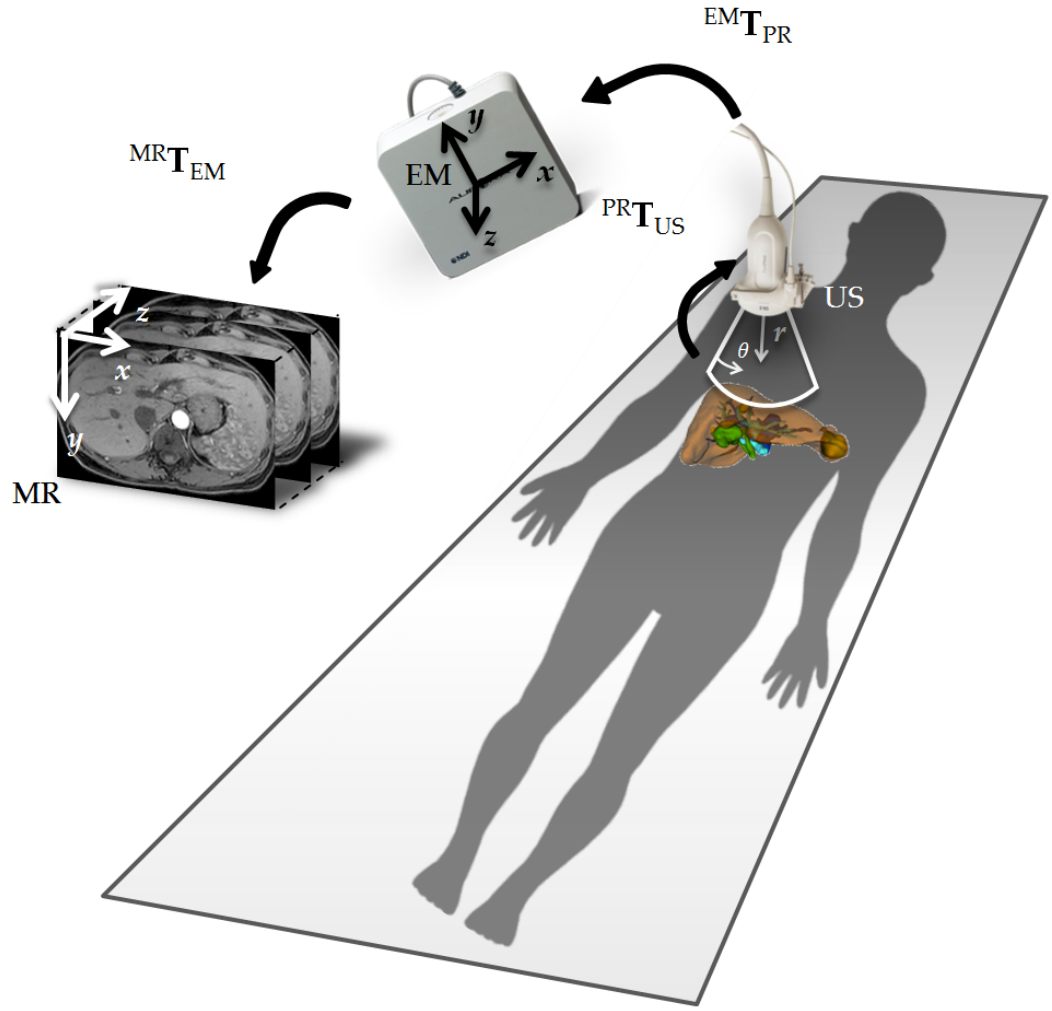

FIGURE 1.5: Visualization of the different coordinate systems' orientations. The planar FG has its Cartesian coordinates (middle), as well as the diagnostic MR scan (left). On the other hand, the 2D ultrasound probe is orientated with a cylindrical coordinate system (right).

1.2.3 PercuNav Ultrasound Platform

The EPIQ7 ultrasound platform with PercuNav software (Philips, The Netherlands) allows clinicians to fuse different diagnostic scans (e.g., CT, MRI, PET/CT) with live ultrasound images. Prior to the intervention (e.g., percutaneous RFA/MWA), data from one of diagnostic scans (CT or MRI) is loaded into the PercuNav system via the picture archiving and communication system (PACS) or directly from the hard drive. Subsequently, co-registration of the diagnostic scan with real-time ultrasound should be performed, with several possibilities for (only rigid) co-registration. Manually, this can be achieved by landmark or point-based registration, and by plane-based registration. Point-based registration is performed by assigning a fiducial on an anatomical structure in an ultrasound image to a fiducial of corresponding anatomy in the other modality, e.g., the MR volume. After performing this step for several fiducial sets, co-registration of the two modalities takes place. The second method, plane-based registration, is achieved by selecting an internal plane in the diagnostic scan that matches the current ultrasound image.

Next to manual registration, PercuNav supports two methods for automatic co-registration in abdominal applications: vessel-based and contour-based registration. In this combination, vessel-based registration is the default method. In the less common cases, where vessel-based registration is not possible, a fusion of two volumes through co-registration of organ's surfaces can be executed automatically.

In automatic vessel-based registration (Figure 1.6), the 3D vessel tree of the liver is automatically extracted from the diagnostic scan. This segmentation is performed based on the central line extraction of vessel-like (e.g. tubular) structures [50]. After this 3D vessel tree reconstruction, an ultrasound sweep of the liver is acquired in such a way that some vessels are included within the field of view. Thereafter, an automatic rigid co-registration between the 3D vessel trees from the diagnostic scan and the vessel branches visible on the US is performed.

In the case of automatic contour-based registration, the 3D surface of the liver is extracted from the CT or MR scan. Next, an ultrasound sweep is acquired in such a way that a part of the diaphragm is visible on the image. At last, a contour-based alignment between the liver surface from the CT or MRI volume and the ultrasound is performed.

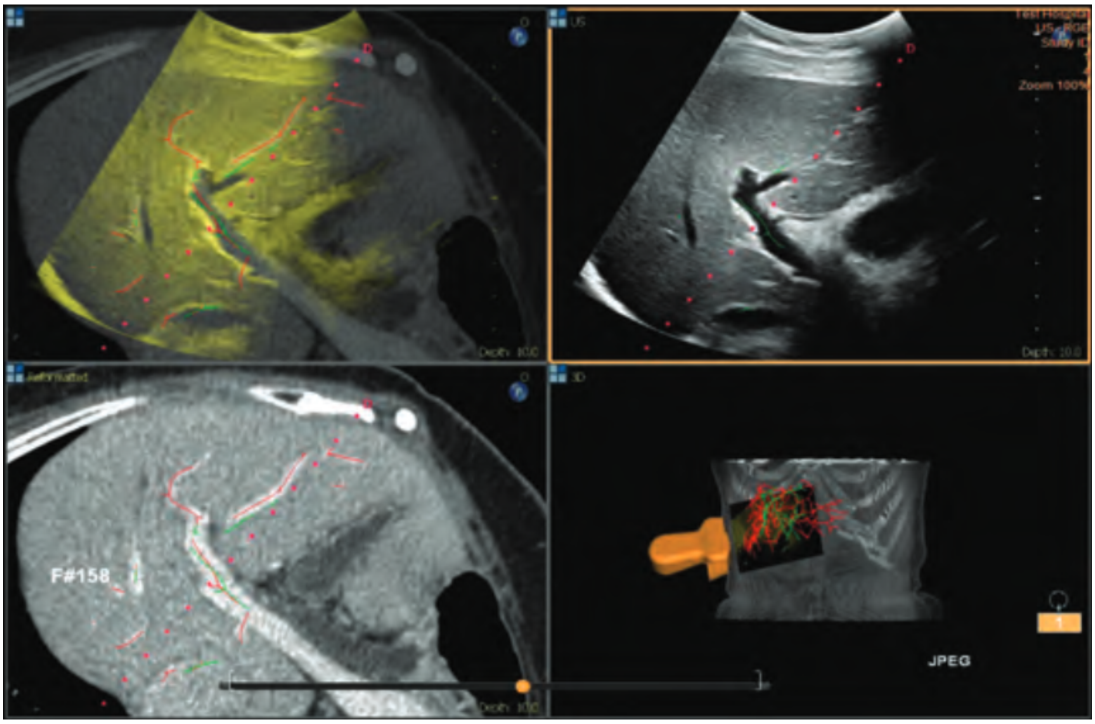

FIGURE 1.6: Auto Registration using a vessel based segmentation of the portal vasculature in the liver, here combining pre-existing CT with real-time ultrasound. In the upper right image only US is visible, in the lower left image only CT. A fusion of CT and US is depicted in the upper left image and a 3D rendering of the probe location with respect to the human body can be seen in the lower right image. Image reproduced from [45].

1.2.4 Registration Accuracy Assessment

Assessment of MR-US co-registration is required to ensure a safe and reliable implementation. Several aspects can affect the accuracy of the co-registration of images, in different parts of the registration process. In various parts of this study, reasons for inaccuracy are diverse and depending on the type of the experiment. While qualitative validation of co-registered images involves subjective evaluation, in this section, quantitative methods for measuring the registration accuracy are described. For quantitative accuracy assessment, not one "gold standard" is present in the clinical environments. When a local accuracy is estimated, it is advised to include reliability bounds since often no reference accuracy is known. A measure of registration accuracy is more easily applied in controlled phantom studies, where local registration errors can be quantified with relatively higher certainty than in clinical application [51].

Image registration accuracy is commonly defined by the root mean square error (RMSE) of the target registration, defined as the mean of the distances between point-correspondences:

$$RMSE = \sqrt{\frac{1}{n}\sum_{i=1}^{n}(p_{1,i} - p_{2,i})^2} \tag{1.2}$$

where the average Euclidean distance between two series $p_{1,i}$ and $p_{2,i}$ with sample size n is calculated.

Many commercial image registration packages and image guided-surgery systems use an error measure referred to as the RMS error, residual error or fiducial registration error (FRE), also in commercially available systems used for real-time ultrasound fusion with preoperative modalities [52].

A commonly used approach as quantitative method for registration accuracy is calculation of the target registration error (TRE), using two sets of corresponding fiducials in a registered pair of volumes. In this way, the Euclidean distance between two sets of points after co-registration is calculated based on points correspondence, therewith providing the user with information about a registration accuracy of the whole target. In a set of points, not only the translation error is determined, rotational error is also optional. When it is desired to calculate a local registration error, fiducial registration error is calculated giving a Euclidean distance of only one pair of points instead of several, thus being equal to the root-mean-square error in fiducial alignment between image space and physical space.

1.2.5 Scale-Invariant Feature Transform

Manual selection of fiducials can influence the registration accuracy substantially. Firstly, interobserver and intra-observer variability can take place in point selection and result in false fiducial matches. Secondly, the process of manual selection is time-consuming. These reasons necessitate the use of a more robust (semi-)automatic method in selection of a pair of anatomical fiducials in ultrasound and its co-registered image set. In the case of multimodal co-registration, here with MR-US, different types of images are matched. Scale-invariant feature transform (SIFT) is explored for the validation of co-registration as an alternative to a registration error value that is returned by a system used for multimodal co-registration. It is important to note that while we are dealing with a 3D MR and a 3D ultrasound volume, we will apply SIFT to the 2D slices of these volumes. Therewith, we aim for an approximation of the locations of detected points in the original 3D volume. This is performed as a 2.5D approach, with a custom-made algorithm. Further application of the described SIFT algorithm is explained in Section 3.2.3.

Lowe's SIFT algorithm is used to detect and describe local features in images [53]. Using scale-space theory [54], keypoints invariant to image scaling and rotation are detected and descripted with the assignment of a local gradient orientation. In this way, theoretically, matching one feature from image A can be correctly matched with high probability to a feature from image B providing a basis for object recognition. The SIFT algorithm is empirically proven to show good performance, being robust to image rotation, scale, intensity change and resistant to moderate affine transformation [55]. This principle is used in e.g., the fusion of color images with fluorescein angiographic images in retinal image registration [56] and multimodal image registration of T1 and T2 weighted MR scans of the human brain [57]. Regarding this study, we are interested in the possible applicability of the SIFT algorithm to assess accuracy of ultrasound-to-MR image registration. The SIFT algorithm is chosen because of its goal to detect local characteristics in one image and match with corresponding characteristics in another image. In this way, theoretically, an intrinsic fiducial that is automatically detected in an ultrasound slice could be detected in the co-registered MR slice as well. SIFT is expected to be useful since co-registered MR data will contain another image resolution, color windowing and contrast than the ultrasound image. Next to that, when the orientation of an anatomical fiducial in MR differs from the orientation of that the corresponding fiducial in ultrasound, still a match can be performed to assess the local registration accuracy.

Before matching of these detected features is possible, the SIFT algorithm is build up in four steps: scale-space extrema detection, keypoint localization, orientation assignment and keypoint description.

In the scale-space extrema detection, Difference of Gaussian (DoG) images are created by applying different sizes of Gaussian $G(x, y, \sigma)$ blurs to the same image $I(x, y)$.

$$L(x, y, \sigma) = G(x, y, \sigma) * I(x, y) \tag{1.3}$$

where $*$ is the convolution operation in x- and y-direction. In so-called octaves, a multiplicative factor k is applied to the image in different neighboring scales, where after subtraction with a k difference a DoG image $D(x, y, \sigma)$ is produced.

$$\begin{aligned}(x, y, \sigma) &= (G(x, y, k\sigma) - G(x, y, \sigma)) * I(x, y) \\ &= L(x, y, k\sigma) - L(x, y, \sigma)\end{aligned} \tag{1.4}$$

with L as the smoothed images. When an octave of DoG image is created, the Gaussian image is resampled with twice the initial value of σ. In this way, for each octave of scale space the original image is convolved with Gaussians. Subsequently, local extrema detection takes place in the scale-space. Each pixel from the DoG images is compared with pixels from the 26-connected neighborhood in the current and adjacent scales, therewith determining a local extremum (Figure 1.7).

As a result of this scale-space extrema detection there is a too high amount of (sometimes unstable) candidates for keypoints. Therefore, the potential keypoints must be refined. A 3D quadratic function, using a Taylor expansion approach of the scale-space function, is used to get true locations of extrema [58]. Detected potential extrema can also be discarded using this function, e.g., in the case of low contrast responses generated by noise [53]. Additionally, potential keypoints with a strong edge response in one direction are rejected as well. For that, the ratio of principal curvatures using the Hessian matrix is used to eliminate points that might belong to an edge. Afterwards, orientation assignment takes place, therewith describing the keypoint with information based on local image properties which now are invariant to image rotation. This information consists of the calculated local gradient and its orientation. This is calculated with help of the gradients calculated around the keypoint (Figure 1.8). Results of the feature calculation are stored and represented in a 128-dimensional feature vector (descriptor).

An extracted feature of one image A is compared to extracted features of the other image B, to find similar regions in two images. To accomplish this, for each descriptor of image A the matching algorithm will find the closest descriptor from image B, returning a match with a corresponding Euclidean distance between the locations of these features. Many features will not have any correct match since they arise from background noise or they don't have correspondence to features in the other image.

To be approved as a match, different conditions can be chosen. A global threshold on distance to the closest feature can be chosen, to exclude too improbable or ambiguous match pairs. The algorithm by Lowe [53] suggested a method for match rejection. This method matches a descriptor d_1 from image A to a descriptor d_2 from image B only if the distance d between these descriptors multiplied by a specified threshold T is not greater than the distance of d_1 to all other descriptors.

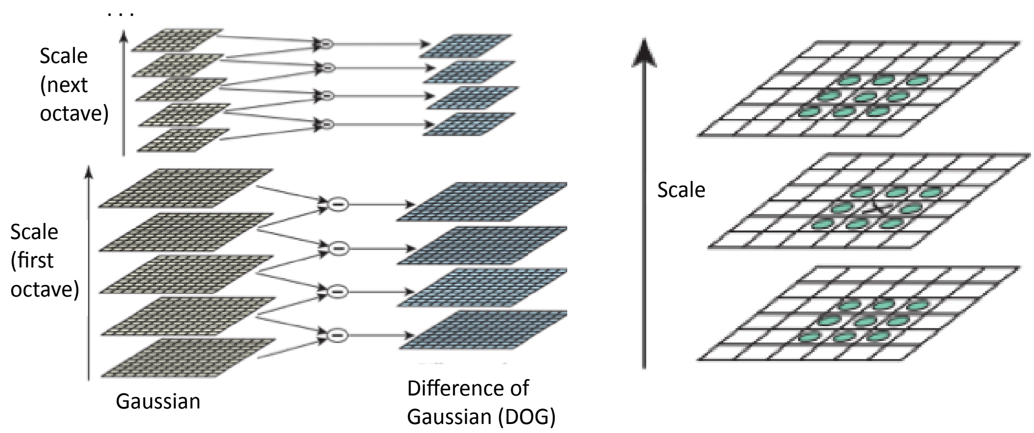

FIGURE 1.7: For each octave of scale space the original image is convolved with Gaussians (left column), where after subtraction of these adjacent Gaussian images results in difference of Gaussians (middle column). Consequently (right column), local extrema detection takes place by comparing a pixel (marked with X) from the DoG image to its surrounding pixels in the current and adjacent scales. Image reproduced from Lowe *et al.* [53].

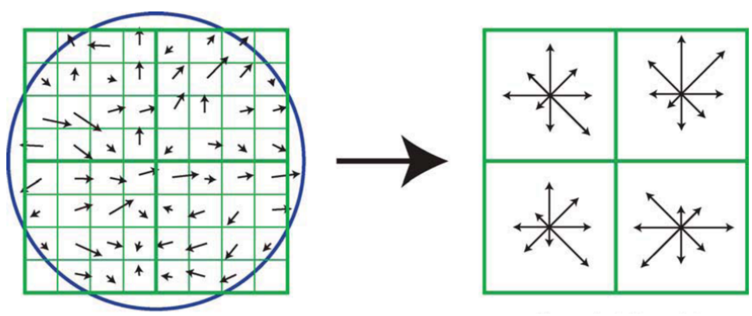

FIGURE 1.8: Image gradients are calculated around the keypoint location at each sample point. The blue overlaid circle indicates the Gaussian window that weights these sample points. Resulting orientation histograms divided per subregion show the resulting gradients of that subregion. Image reproduced from Lowe *et al.* [53].

1.3 Objectives

Primary objective

The main goal of this thesis is to determine the feasibility of ultrasound-based navigation for surgical resection of liver lesions and make the first steps towards clinical implementation.

Secondary objectives

- Assess whether rigid registration for local MR-US fusion leads to sufficient accuracy in phantoms and on *ex vivo* samples.
- Adapt the application's workflow to successfully incorporate US-based navigation into open liver surgery in a logistically approved and accurate way.
- Develop a completely implemented ultrasound-based navigation routine that can be used during open surgery of colorectal liver metastases with the use of Philips' PercuNav system.

Chapter 2

Phantom Study

Summary

Prior to implementation of ultrasound-based navigation into clinical practice of open hepatectomies, it is important to assess the accuracy of registration of intraoperative ultrasound to diagnostic MR/CT scans. This aspect needs to be accessed in a safe and controlled environment. The first goal of this work was to construct a multimodal liver phantom that is suitable for ultrasound, computed tomography, and magnetic resonance imaging. The second goal was to subject the developed phantom to artificially applied deformation similar to intraoperative deformation of the liver. The phantom is composed of three mimicked structure types: liver parenchyma, tumor and vasculature. Co-registration accuracy of real-time ultrasound to CT and MR images was calculated after plane-based and point-based registration, using Philips PercuNav registration software. Raw data retrieval from the system was impossible, for this reason an alternative post-processing method was developed. Distances between fiducial pairs of both US and CT or MR points were calculated using Euclidean distance computation at locations distributed around the center of registration. In measurements without deformation, registration accuracies were measured of 5 to 10 mm in the -2 to +2 cm area around the registration plane or average of four registration points. When deformation is applied on the phantom by tilting half of it with a 30° angle, registration accuracy stayed under 10 mm. These accuracies showed that possibilities of *in vivo* applications are present, which requires further research. In some of the experiments, registration accuracies under 5 mm were achieved, which also have been shown in other studies. Effects of deformation in terms of variation in local registration errors were not described before, from this research it is advised to keep the region of interest small to ensure an acceptable registration accuracy.

2.1 Introduction

Co-registration of magnetic resonance and real-time ultrasound images needs to be tested for navigation surgery purposes in open liver resections. Immediate implementation is not possible due to unknown accuracy and patient safety. Ideally, research towards a safe and accurate development of ultrasound-based navigation should be performed in a controlled and liver-simulating environment, e.g., on phantoms.

To create a liver-mimicking environment, phantoms must meet several major requirements. First of all, compatibility with ultrasound, computed tomography and magnetic resonance imaging is required. This includes the possibility to distinct different tissue-mimicking structures in the three imaging modalities and, additionally, safety of imaging (e.g., no magnetic materials in MRI) and a minimal effect of artifacts are essential. The second requirement is a degree of anatomical similarity. Preferably, a liver phantom consists of components with liver-like characteristics such as flexibility, tumor-like structures and deformable vessels-like structures.

In literature, several approaches have been proposed for the development of phantoms with the aim of mimicking soft tissue. For that, various materials can be used including, but not limited to: agarose and gelatin compounds, oil gel, room-temperature-vulcanization-silicone polyvinyl alcohol (RTV-PVA), polysaccharide gels, and flexible plastic [59]. While hydrogels based on agarose or gelatin are easily fabricated and have multimodal compatibility, they come with disadvantages such as vulnerability and lack of durability [60]. While degradation over time is limited in oil-based compounds, application in ultrasound is cumbersome due to a high density and too low attenuation of ultrasound waves [61]. RTV-silicone for mimicking soft tissue comes with the advantage of quick fabrication and high durability. However, due to a relatively high stiffness and long hardening time it is considered as not suitable for a liver-mimicking compound. PVA-based or polysaccharide compounds are durable over time and provide flexibility of the compound as a whole. Disadvantageous is that fabrication of PVA-based phantoms consists of several 12 hour freeze-thaw cycles and precise control of the temperature [62]. On the other hand, polysaccharide gels require precisely controlled gelling time and the gel-water ratio [63]. Additionally, air bubbles are incorporated in the compound which is problematic in ultrasound imaging. Flexible types of plastic can be heated and molded into a desired shape resulting in a firm and flexible phantom. However, during heating unwanted air bubbles are formed in the compound.

In this work, a multimodal liver-mimicking phantom was developed based on plastisol melting techniques described by Ungi *et al*. [64] in combination with the three-dimensional (3D) printing technique laser sintering. A phantom is fabricated that consists of three mimicked tissue types: hepatic and portal veins, tumors and liver parenchyma. Flexible hepatic and portal veins are 3D printed via laser sintering of thermoplastic urethane, based on a segmentation of a CT scan of the liver. For the tumors and the liver parenchyma, plastisol and plasticizer are heated and shaped in a mold, resulting in a flexible surrounding for the vessels.

Several systems are developed with the intention to percutaneously guide biopsy or ablation needles based on electromagnetic navigation, established by co-registration of live ultrasound with previously acquired CT or MR scans [49, 52]. However, in these cases, the liver is naturally fixated inside the abdomen. It is desired to investigate application in open liver surgery, hence effects of liver deformation need to be assessed with experiments.

In this chapter, experiments are divided in two parts, i) accuracy measurements with the liver phantom in a non-deformed setting and ii) accuracy measurements influenced by deformation. Accuracy measurements with the liver phantom in a non-deformed setting need to be carried out to determine the effects of different registration methods on local registration accuracy. These measurements are fundamental to ascertain the range of an acceptable accuracy when no deformation takes place as the best-case scenario. Afterwards, the effects of deformation on the local registration accuracy need to be determined. The objective is to indicate which settings are required for acceptable registration error and feasible application in circumstances with liver deformation. Therewith, the boundaries were determined of the region of interest in which MR-US fusion can safely be used with a satisfactory local registration accuracy. In literature, tissue registration error (TRE) and root-mean square error (RMSE) are established methods to quantify reliability for image fusion. However, interests lay in registration accuracy in relation to the registration area. Therefore, the local registration error (LRE) is introduced.

2.2 Materials and Methods

The compositions of the materials used for mimicking the liver and the used equipment are described below, divided per structure type. The phantom as a whole is constructed inside a stainless-steel mold to determine the shape (Figure 2.2c). First, the appropriate vessel structures are designed for and constructed with laser sintering. Second, several lesions is produced. Third, the liver parenchyma is produced that facilitates finalization of the phantom and preserves coherence of the whole phantom.

2.2.1 Preparation and 3D Printing of Vessels

To mimic liver vasculature, there is decided to use three-dimensional printing of portal and hepatic vessels. To do this, vessels of a randomly anonymized scan are segmented using liver segmentation tools in IntelliSpace Portal software (Philips Healthcare, Best, The Netherlands). To ensure a non-fragile structure for 3D printing, slightly thin branches are dilated and too thin distal branches are excluded (Figure 2.1).

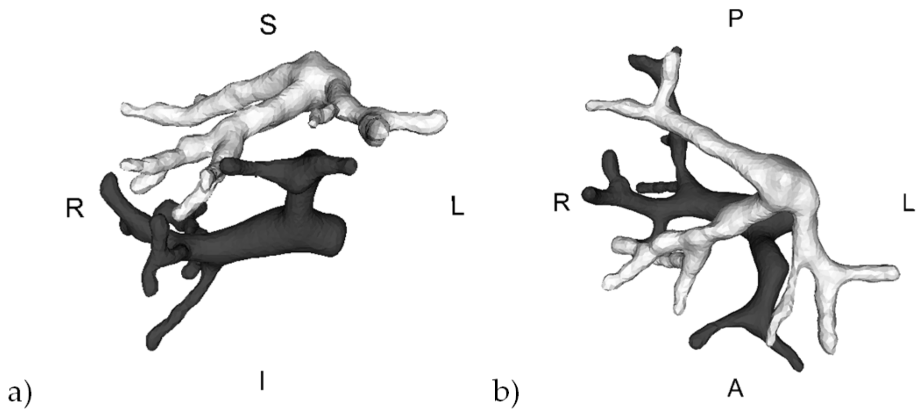

FIGURE 2.1: Visualization of the portal (black) and hepatic (white) veins, which are the structures selected for 3D printing. a) Anterior view, b) superior view. Main vessels are visible, together with some first and second order branches.

This resulted in two separate vessel structures that are printed by an external party (Materialise NV, Leuven, Belgium). Three-dimensional printing is performed with laser sintering. To mimic elastic properties, a rubber-like material is chosen named TPU 92A-1, which is a thermoplastic urethane [65]. This strong and flexible material has a melting temperature of 160°C. This temperature was required in the further construction of the phantom (Section 2.2.3). The portal vasculature was dyed black, and hepatic vasculature was dyed white, to facilitate distinction between the two different vasculatures inside the phantom.

2.2.2 Phantom Tumor Development

It is desired to mimic the surgical situation of a patient with several colorectal metastases. Next to that, we want to be able to assess the possibilities of MRI-US fusion when tumors are located in different anatomical situations. Therefore, it is decided to insert different tumor-like structures inside the developed phantom. To mimic realistic structural properties, elasticity is desired to be comparable to the phantom parenchyma. No plastic softener was added in the tumors' fabrication process with two goals. Firstly, tumor palpation in the liver phantom is hereby enabled. Secondly, not using plastic softener leads to a different density i.e. distinction from its surroundings. Thus, only plastisol is used in combination with a plastic coloring (M-F Manufacturing Co., Inc. Fort Worth, TX, USA).

The tumors need to be visible on CT and MRI. To that end, a small portion of magnesium oxide is administered in the fabrication process of the phantom tumors. Subsequently, a bit of liquid color is added resulting in non-transparent, differently colored tumors (Figure 2.2b).

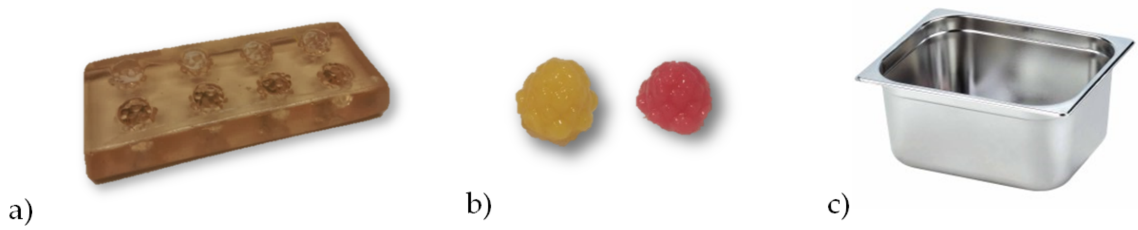

FIGURE 2.2: a) Mold used for construction of the tumors. b) Two examples of tumors with different coloring, created using the mold. c) Stainless-steel gastronomy container in which the phantom was constructed.

Plastisol is a heterogeneous mixture of PVC particles in a liquid plasticizer. Heating the mixture to 180°C causes mutual dissolution. After pouring it into a mold, cooling results in a set of flexible, plasticized tumors when a temperature lower than 60°C is reached. The phantom tumors are constructed in a mold (M-F Manufacturing Co., Inc. Fort Worth, TX, USA [Figure 2.2a]), before development of the parenchyma and finalization of the phantom. The diameter of the tumors is kept constant at approximately 13 mm.

2.2.3 Parenchyma Development

To mimic liver parenchyma, a flexible material is fabricated to surround the laser sintered vessels and the created phantom tumors. Just as the previously described vessels and tumors, the simulated parenchyma is desired to have elastic properties comparable to human liver parenchyma. To assure this, the elasticity and deformability of the phantom are chosen with help of two surgeons that are involved in this research project. For that, the same type of plastisol is used as in Section 2.2.2.

To increase flexibility of the parenchyma-mimicking compound, plasticizer is added to the plastisol. In total, 1650 mL of plastisol was mixed with 550 mL of plasticizer what resulted in

2200 mL liquid that was used for creation of the phantom's parenchyma. Phantom construction took place in a fume hood to limit exposure to chlorine gas release during the fabrication process. Two heaters with magnetic stirring were used during the preparation of the parenchyma volume. Heating of the liquid to 180°C was required to assist the progress of sufficient blending of the two compounds. Additionally, magnetic stirring had the purpose of reducing the amount of air bubbles in the mixture, since air bubbles induce problematic imaging in all of our three used imaging modalities.

2.2.4 Phantom Finalization

It was desired to mimic a realistic, however simplified, shape of the liver in the phantom. Therefore, a mold is chosen that can contain a large volume of liquid. A stainless-steel gastronomy container was used (Figure 2.2c), that is positioned at a 35° angle and gives the phantom's characteristic shape. When the temperature of the fluids dropped to 155-160°C, it was poured in the mold slowly, while simultaneously the vessel structures are submerged in the liquid compound. These structures were held in their desired positions for about 15 minutes. After this time, the liquid has cooled down and has become rigid enough to maintain the positioning of the vessel structures. At this moment, the tumors were maneuvered into the compound resulting in a permanent fixation inside the parenchyma. The whole setup was kept in this position for several hours until properly cooled down, resulting in a finalized phantom (Figure 2.3).

FIGURE 2.3: Top and side view on the multimodal liver phantom. The shape of the phantom mimics the significantly simplified natural shape of the liver. The transparency of the parenchyma enables visibility of all anatomical structures in the phantom.

2.2.5 Scan Acquisition

In preparation of the registration experiments, scans were acquired with different modalities. MR imaging was performed on an Achieva (Philips Medical Systems, Netherlands) 3.0-T system with the use of the body coil for transmission and reception of the signal. Standard diagnostic T2-weighted mDIXON liver scan protocol was used [66]. This resulted in 3D image volume with a spatial resolution of 1.0x1.0x1.5 mm voxels, providing suitable details of the phantom for MR-US fusion purposes (Figure 2.4a). Next, a dedicated helical CT scan (Toshiba, Acquilion) of the phantom was acquired with the same purposes. The CT scan was acquired according to the abdominal clinical diagnostics (Figure 2.4b) and reconstructed on a 1.0x1.0x1.0 mm voxel grid.

Afterwards, The MRI and CT scans are transferred through the picture archiving and communication system (PACS) to facilitate data selection for fusion at the PercuNav software module. The software module PercuNav on ultrasound platform EPIQ7 (Philips Healthcare, Best, The Netherlands), intended for percutaneous guidance of needles based on electromagnetic navigation, establishes fusion of live ultrasound with previously acquired CT or MR scans [67].

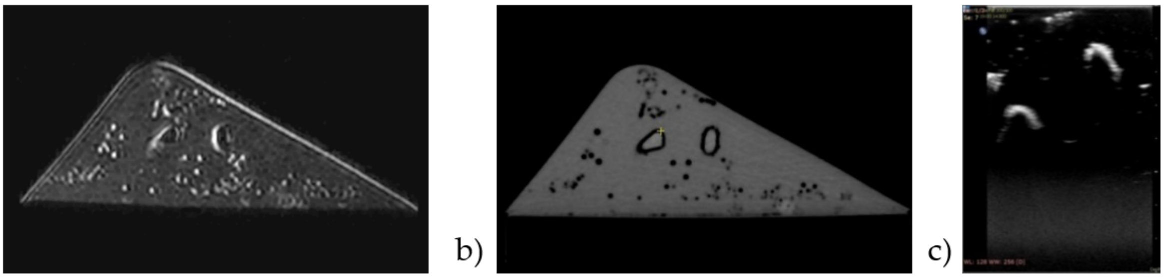

FIGURE 2.4: T2-weighted MR scan (a), CT scan (b) and ultrasound image (c). All scans are depicted at the same axial cross-section, taking into account the fact that the ultrasound image is acquired with the probe positioned perpendicularly on the right sloped surface visible in the scans.

2.2.6 Experiment Setup

To facilitate fusion of CT or MR scans with real-time ultrasound data, several preparations were performed. The experiment setup is performed at the interventional radiology suite. Ferromagnetic materials in the environment can cause distortions in the susceptibility of electromagnetic tracking systems (EMTSs). Therefore, interference of these materials is minimized by placing the phantom on a plastic surface on an imaging table. Next to that, any ferromagnetic object remains distant from the setup. When the phantom is placed correctly on the imaging table one electromagnetic (EM) sensor containing two five degrees of freedom (5DOF) sensors is fixated on the phantom's surface with a thin metal wire to serve as an additional reference in the EM field. An electromagnetically tracked sensor is mounted to the ultrasound transducer with a clip-on bracket [68], hereby facilitating tracking of the transducer inside the EM field.

In the setup of the phantom experiments, different components are compared for assessment of ultimate feasibility in liver surgery. First of all, the applicability of diverse transducer types is assessed since different transducers have specific properties in terms of depth and field of view. Therefore, accuracy measurements are performed using the following dedicated transducers: a 1-5 MHz curved-array transducer and a 5-12 MHz linear-array transducer. Experiments are performed with CT as well as MR scans to assess the possibilities of using different modalities for image fusion. For accuracy measurements in deformation setting, only the 5-12 MHz linear-array transducer is used in combination with MR scans.

To gain insights in terms of accuracy, possibilities and potential applications of the fusion software different settings are tested in different experimental circumstances. Regarding registration methods, three types are appealing for possible application concerning the liver, i.e., i) internal plane registration, ii) internal landmark registration, and iii) automatic registration based on automatic vessel or liver surface extraction. Automatic registration was not successfully performed due to non-executable vessel and liver surface extraction in the ultrasound images of the phantom. Hence, experiments have been performed only with registration based on internal planes and internal landmarks.

Experiments are divided in two parts, i) accuracy measurements with the liver phantom in a non-deformed setting and ii) accuracy measurements influenced by deformation (Figure 2.5).

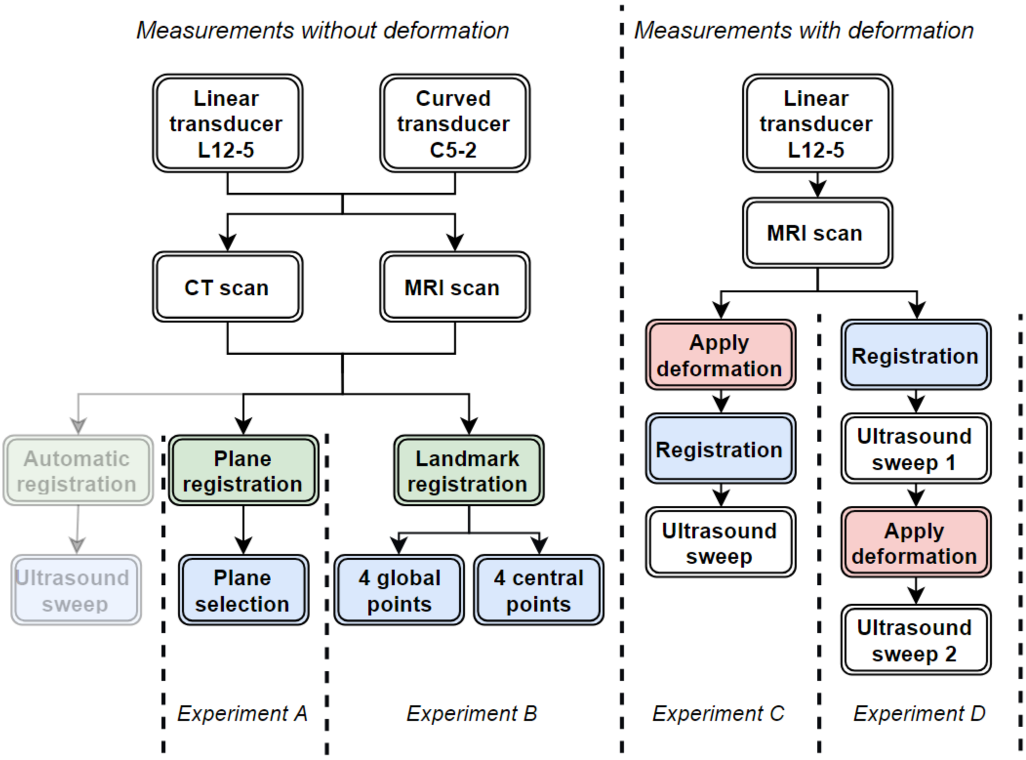

FIGURE 2.5: Illustration of the possible configuration for measurements. On the left, after transducer selection, CT or MR data for fusion is selected. Afterwards, the type of registration is selected. Automatic registration is not performed. Distinction is made between measurements with (left column) and without deformation (right column).

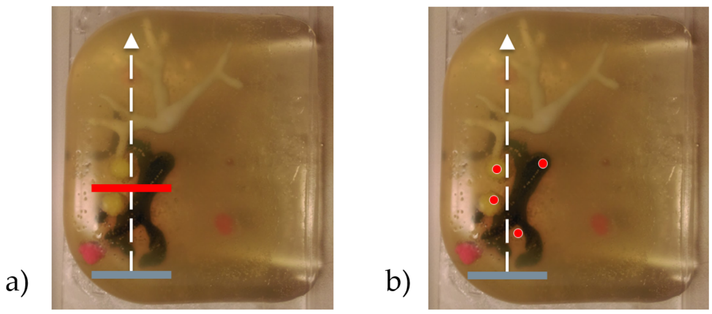

FIGURE 2.6: Illustration of the performed ultrasound sweeps. a) After plane-based registration in the red plane, the ultrasound probe is positioned perpendicular to the surface, starting at the grey bar and moving to the other side of the phantom. b) After point-based registration, a measurement is performed in the same way as for plane-based registration.

Measurements Without Deformation

Experiment A: Plane-based Registration

First, a 3D ultrasound sweep required for plane registration was performed. Next, a single axial plane was selected in both 3D ultrasound image and the MR or CT volume. After this, a rigid registration between two datasets was performed to match real-time and diagnostic images. At last, manual correction for residual rotational error in plane-based registration was performed. At this step, registration was finalized and stored, and the phantom was ready was ready for registration accuracy measurements.

For accuracy measurement, an ultrasound sweep was made from the caudal to the cranial part of the phantom. This sweep was performed along the site of registration, while attempting to maintain a constant pace (Figure 2.6). Comparison was made between co-registration with CT volume and co-registration with MR volume. Accuracy measurements were repeated five times for co-registration with CT, and three times for co-registration with MR volume.

Experiment B: Global versus Central Point-based Registration

For point-based registration, a 3D ultrasound sweep was performed. Next, multiple reference points were selected in both 3D ultrasound image and the CT volume. After this, a rigid match between two datasets was performed to register real-time and diagnostic images. At this step, registration was finalized and stored, and the phantom was ready for the registration accuracy measurements. In the selection of registration points, a distinction was made between either centrally (within 5 cm distance from each other) or globally selected (within 10 cm distance) selected points. Co-registration was performed only with CT volume, to minimize the influence of diagnostic scan type on the accuracy of registration with globally and centrally selected landmarks.

For accuracy measurements, an ultrasound sweep was made from the caudal to the cranial part of the phantom. Just as in experiment A, this sweep is performed along the site of registration while attempting to maintain a constant pace. The experiment was repeated three times for globally selected registration points, and three times for centrally selected registration points.

Measurements With Deformation

Experiment C: Registration on Deformed Phantom

In this experiment, the phantom was deformed by placing a wedge underneath one half of the phantom with an approximate 30° angle (Figure 2.7). The reference tracker was placed at the transition between the flat and the tilted part of the phantom surface. Afterwards, co-registration was performed with MR volume. Thereafter, plane-based registration was compared with point-based registration. For plane-based registration, the central plane, transitional between the flat and the tilted part of the phantom surface, was selected for plane-based registration. Four registration points within 5 cm of each other, around the described transition plane, were selected for point-based registration.

Both types of registration were performed in triplicate (Figure 2.6). In each of these measurements, the same registration planes in plane-based registration and the same reference points in a point-based registration were chosen. Similar to experiment A and B, after each accepted registration, an accuracy measurement was performed. This was done by making an ultrasound sweep from the caudal to the cranial part of the phantom, with the transition between the straight and tilted part of the phantom in the middle. This was done to evaluate if deformation-related errors in MR to US registration can be diminished by secondary registration on an already deformed organ.

Experiment D: Registration Accuracy Before and After Deformation
In this experiment, plane-based and point-based co-registration with MR volume are both used on the liver phantom. The reference tracker was placed in the same location as the experiment C, as well as the registration area in the center of the phantom. In contrast with previous experiments, two ultrasound sweeps are performed for accuracy measurements per accepted registration, i) on the non-deformed liver phantom and ii) after applying a 30° angle on half of the phantom (Figure 2.7). This was done to assess the severity of registration errors relation to the deformation, e.g., hereby simulating a registration error due to intraoperative manipulations of the liver after registration.

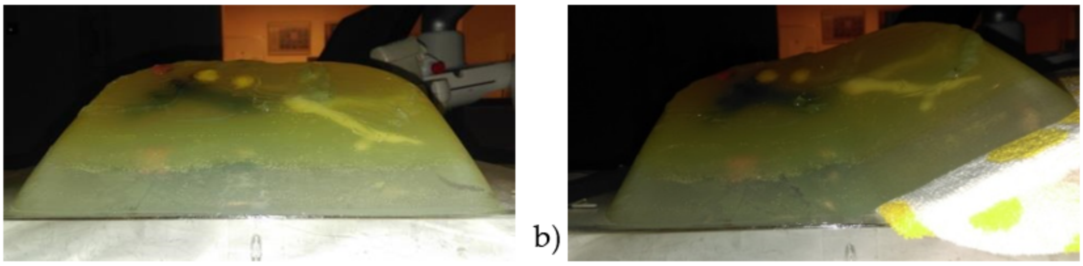
a) b)

FIGURE 2.7: Phantom before deformation (a) and after deformation (b), a 30° angle is applied in relation to the center of the phantom.

2.2.7 Post-processing

When a registration is performed, it is crucial to assess its accuracy. The possibilities of determining this accuracy are limited in the software package of PercuNav. Firstly, a Registration Fit Value, presumably a target registration error (TRE), is returned by the software after the registration. However, this error value is lacking information: the TRE does not provide us with any information regarding the distribution of local errors in the volume around the region of registration. Secondly, there is a strong limitation in analysis of the raw data. Output data of the fusion is not provided with the pose (position and orientation) of the ultrasound transducer in relation to the CT or MR volume. In the case of MR, this inhibits an accurate analysis of MR-US registration. Therefore, an alternative method is developed to analyze local registration errors. This method is divided in two parts. Firstly, in 3D Slicer, (version 4.6.2, research platform for analysis and visualization of medical images) fiducials are placed to compare a point in the MR volume to the corresponding place in the ultrasound image. Afterwards, accuracy is calculated in MATLAB (version 9, R2017a, The MathWorks, Natick, MA, USA).

DICOM data of the measurements is imported in 3D Slicer. In the case of co-registration of MR to US, output of one measurement is stored by the registration software in one DICOM volume in which four screens are visible: the MR slice, the corresponding US image, a 3D volume rendering and a MR-US fusion image. A fiducial is placed in the MR image, as well as a fiducial on the corresponding place in the US image. This is performed ten times in the DICOM volume, resulting a set of ten fiducials for MR volume and a set of ten fiducials for the US volume. The registration plane is saved as a fiducial in the case of plane-based registration, the four registration points are saved as four fiducials in the case of point-based registration.

In a three-dimensional Cartesian coordinate system, a point is described as (x, y, z) where distances can be denoted (e.g., in cm or mm). This is the case in image volumes such as MR or CT scans. However, image dimensions of a measurement, which are stored in a DICOM file, are saved in a coordinate system with an x- and y-axis and a temporal dimension on the z-axis (Figure 2.8). This strongly inhibits an easy 3D RMS error calculation. In this file, (x, y) can easily be converted from pixels to centimeters with help of the centimeter-scale of the ultrasound interface. In contrast, one slice in z-direction is 66 milliseconds. Therefore, rescaling of the z-axis from a temporal dimension to a spatial dimension is carried out. This is performed with help of the dimensions of the original MR volume. The most caudal and most cranial point of a measurement in the DICOM measurement file are specified with fiducials in the original MR data to determine the exact position in mm. With the z-coordinates of the most caudal and cranial point, now being spatial instead of temporal, rescaling of the intermediate points is performed. To enable this rescaling procedure, the assumption is made that the ultrasound moves with a constant pace.

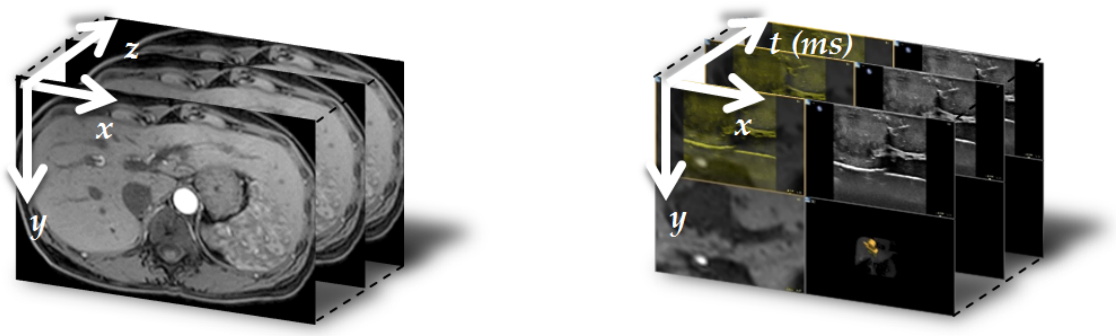

FIGURE 2.8: On the left, an illustration of the coordinate system with respect to an MR volume. All axes are spatially oriented. On the right, the output of the used ultrasound machine is shown with a temporal orientation along the z-axis, since it is a video recorded as a DICOM file.

2.2.8 Statistical Analysis

Statistical analyses were performed using Matlab (version 9, R2017a, The MathWorks, Natick, MA, USA). For all measurements, mean and standard deviation were derived as well as 68% confidence intervals (CI) of the mean. These statistical measures and this exact confidence interval were chosen due to the limited amount of measurements.

2.3 Results

Results of the accuracy measurements on the liver phantom are divided into two parts: measurements without deformation and measurements with deformation. During post processing, each measurement took approximately 30 minutes (placement of all fiducials and determining the rescaling of the z-coordinates). Assessment of registration accuracy is performed by calculating the Euclidean distance between a pair of corresponding fiducials in the ultrasound image and the CT or MR volume. For that, the resulting DICOM images retrieved from the PercuNav system are used (Figure 2.9). Euclidean distances are calculated for each of ten pairs of fiducials, resulting in ten local registration errors per performed ultrasound sweep.

Measurements Without Deformation

As a result of each post-processing of each measurement, Euclidean distances were calculated

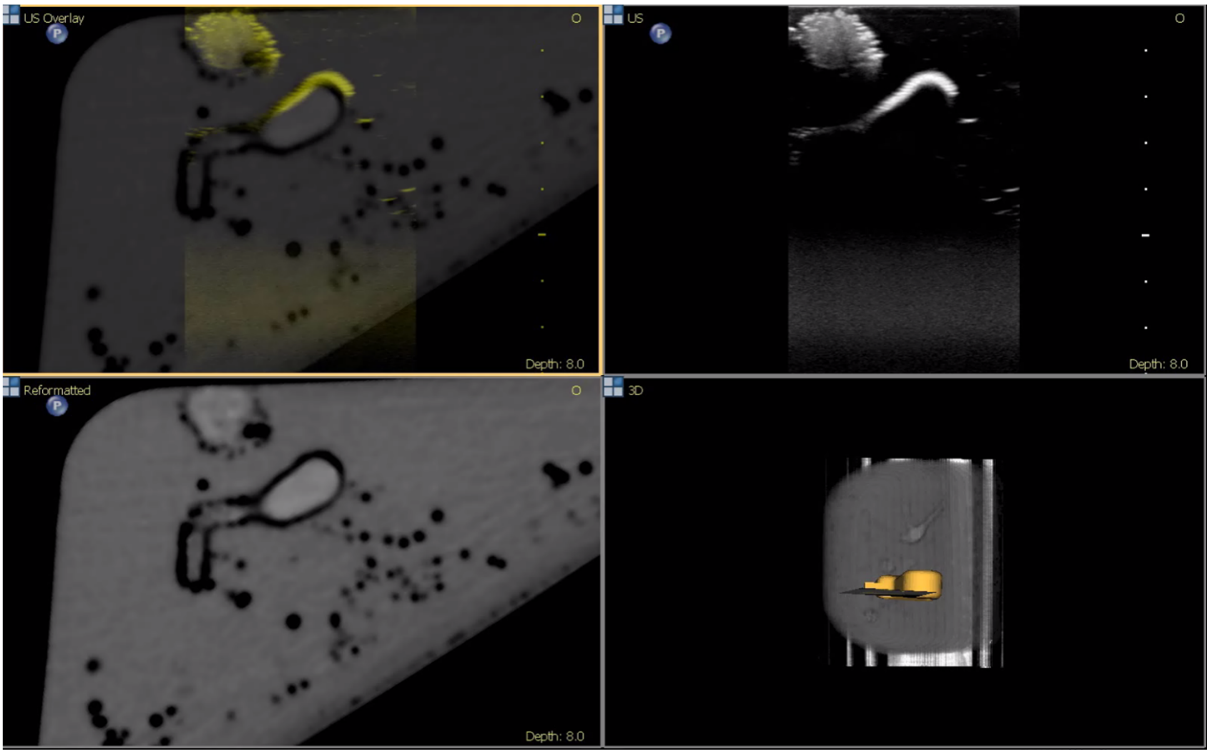

FIGURE 2.9: Resulting image from the DICOM volume after a successful CT-US registration, consisting of four quadrants: the US image, co-registered CT image, an overlay image and a 3D rendering are depicted.

and visualized in a 3D plot to assess incorrect fiducial placement. In case of plane-based registration, local registration errors of each measurement are visualized in proportion to the z-coordinate of the registration plane (Figure 2.10). In case of point-based registration, these errors are visualized in relation to the mean z-coordinate of the four registration points.

Experiment A: Plane-based Registration

For plane-based registration, five CT-based measurements were performed resulting in 50 local errors, while three MR-based measurements resulted in 30 local errors (Figure 2.11). Rescaling all measurements in relation to the registration plane enabled mutual comparison. Positions of the local errors for MR-US fusion measurements are less balanced than measurements for CT-US fusion. Trend lines of the local means in 2 cm regions show an increase of local registration error when further away from the plane of registration. Statistical comparison between CT-US and MR-US registration is not possible, however, the magnitude of local registration errors is comparable at the centers of registration and the -4 to -6 cm area.

Experiment B: Global versus Central Point-based Registration

For point-based registration, a comparison is made between four centrally and four globally selected points for registration. For each method, 3 times 10 local registration errors are calculated (Figure 2.12). For centrally selected registration points, the maximal distance between the points was approximately 5 cm. For globally selected registration points, this distance was roughly doubled to 10 cm. The locations where registration errors were measured were at maximum in range of the locations of the registration points. The distribution of the error measurements is unequal, for global point-based registration more than for central point-based

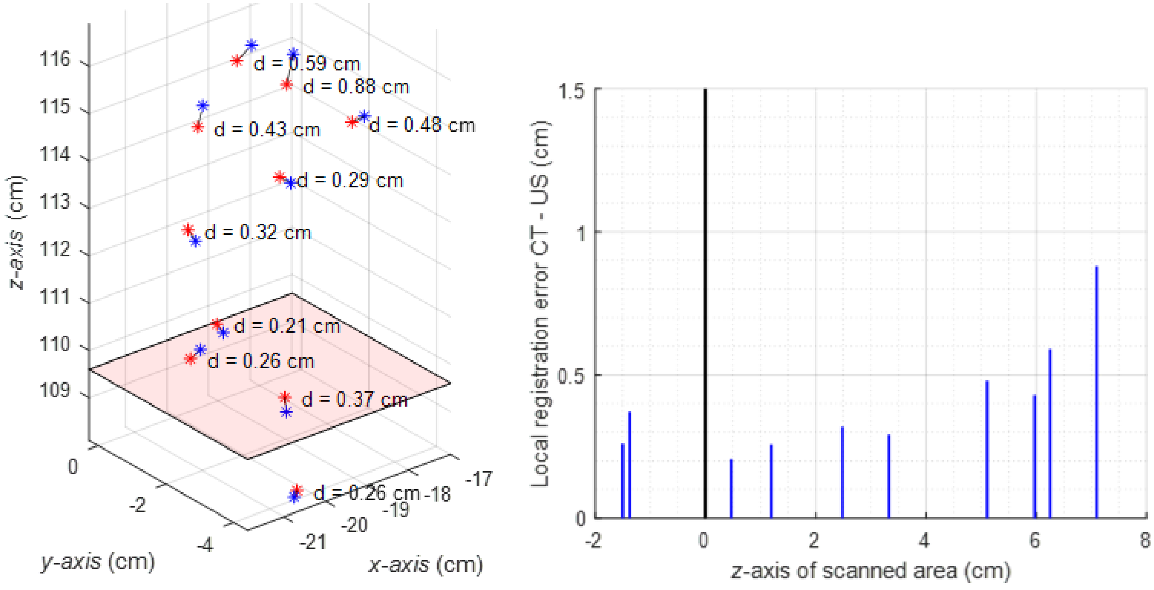

FIGURE 2.10: One plane-based registration of CT and ultrasound, acquired with a linear transducer. Local registration errors are visualized between a set of ultrasound (red) and CT (blue) fiducials in one measurement (left); the z-coordinate of the registration plane is depicted as a plane in red. The same errors are shown in proportion to the z-coordinate of the registration plane (black line, right).

registration. Trend lines with ±1 SD show a relatively constant local registration error for globally selected registration points in comparison to centrally selected registration points, where errors tend to decrease when further away from the average registration error.

Measurements with Deformation

Experiment C: Registration on Deformed Phantom

Local registration errors of plane-based and point-based registration on are visualized in Figure 2.13. In the ±2 cm areas next to the center of registration, high accuracy is achieved in plane-based registration (2.8 ± 1 mm) as well as in point-based registration (3.0 ± 2 mm). Trend lines based on the local mean show a decrease of local registration accuracy up to +1 cm when measuring more than 4 cm away from the center of registration. Corresponding error bars of these errors tend to increase when further away from the center of registration. While plane-based as well as point-based registrations both have been performed three times resulting in 30 registration errors each, the distribution of the measurements is not equal per bin but globally acceptable.

Experiment D: Registration Accuracy Before and After Deformation

The difference in registration errors before and after deformation is visualized in Figure 2.14. Experiments have been repeated three times for plane-based registration and point-based registration, both resulting in 30 local registration errors before and 30 after deformation. Distribution of measurements was acceptable per bin, with the exception that errors are mainly located at the left from the registration plane.

The local registration errors measured after plane-based registration do not differ from errors before deformation: ±1 SD error bars are comparable in size, as well as the locations of the local mean per bin.

As a result of the applied deformation with point-based registration, the mean local registration error is increased from 3.0 ± 1.5 mm to 6.3 ± 3.5 mm in the ±2 cm region of the average registration point. In the area of -4 to -6 cm away from the center, the local registration error increased from 8.2 ± 2.7 mm to 15.8 ± 5.7 mm.

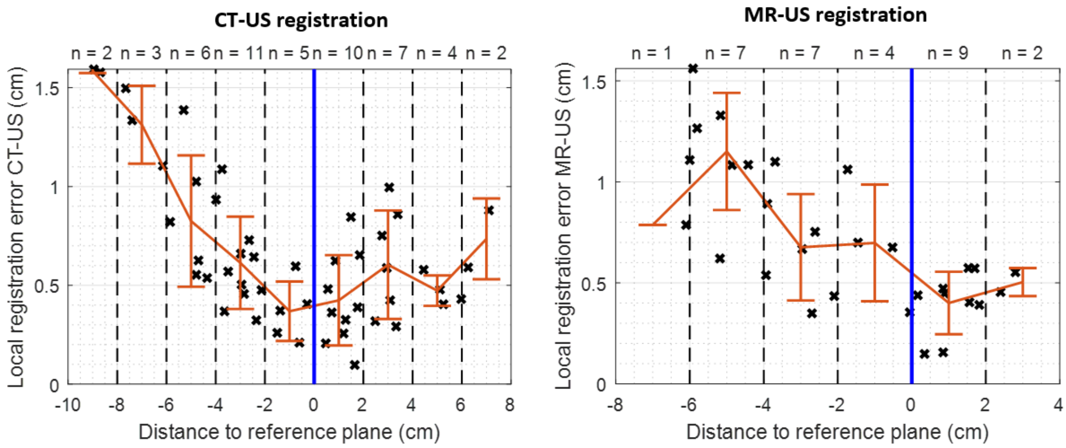

FIGURE 2.11: Experiment A - Plane-based registrations acquired with a linear transducer resulting in local registration errors of CT-US fusion (left, n=50) and MR-US fusion (right, n=30). Error bar shows ±1 SD in each 2 cm region next to the plane of registration (blue). A trend line is drawn through the local mean in each 2 cm region.

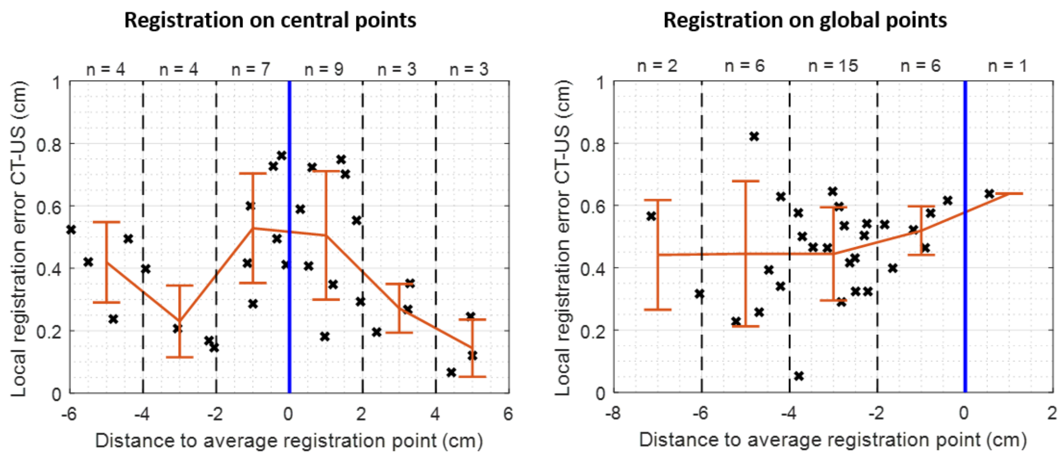

FIGURE 2.12: Experiment B - Point-based registrations acquired with a linear transducer, comparing centrally to globally selected points for registration. Error bar shows ±1 SD in each 2 cm region next to the plane of registration (blue). A trend line is drawn through the local means of each 2 cm region.

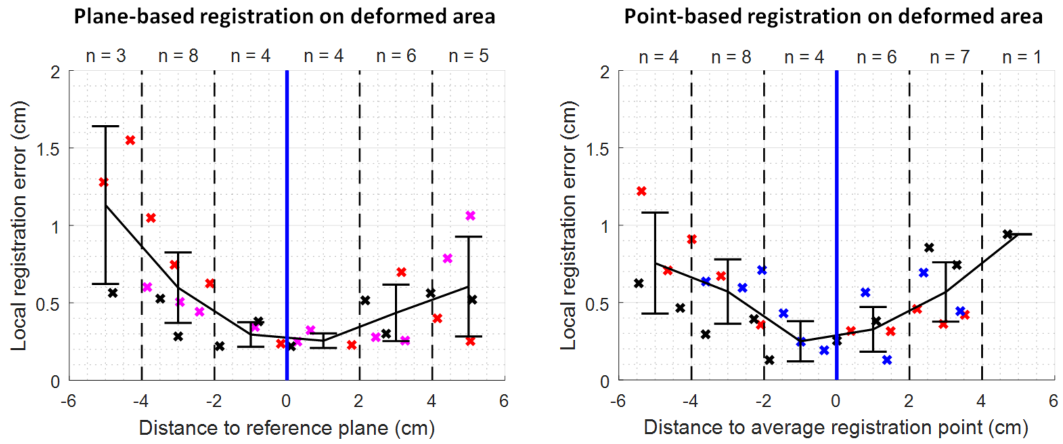

FIGURE 2.13: Experiment C - Comparison of plane-based registration (left) and point-based registration (right) on a deformed area. Once again, error bar shows ±1 SD in each 2 cm region next to the plane of registration (blue). A trend line is drawn through the local means of each 2 cm region. Scattered points belong to the same measurement and registration in one graph.

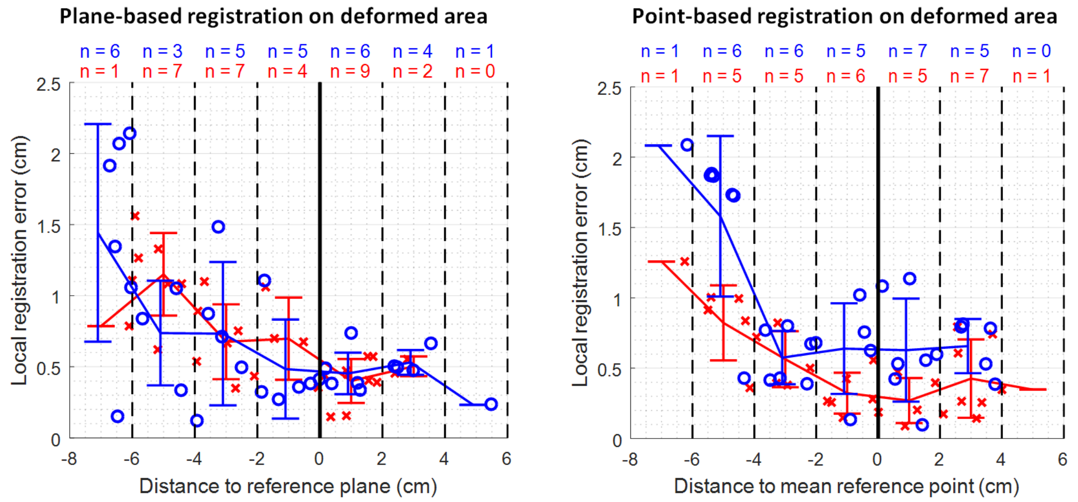

FIGURE 2.14: Experiment D - Deformation effects on plane-based registration (left) and point-based registration (right), with measured errors before deformation (red) and after (blue). Once again, error bar shows ±1 SD in each 2 cm region next to the plane of registration (black). A trend line is drawn through the local means of each 2 cm region.

2.4 Discussion

Using the proposed materials and techniques, a suitable liver phantom is fabricated that was in compliance with the requirements of mainly deformation and multimodal imaging. As regards deformation, the phantom was successfully subjected to deformations after which it could recondition to its original state with ease. As regards multimodality, distinction between structures was possible, but not ideal. Firstly, due to a lacking permeability of the 3D-printed vessels for ultrasound waves resulting in acoustic impedance differences, only the upper border of the vessel wall is imaged. This inhibited the possibility of vessel extraction for automatic co-registration, which absence is a major shortcoming. Secondly, a submillimeter thin layer of air bubbles during phantom fabrication which can be misleading during co-registration and post-processing.

Basic knowledge of the options for image registration is required to investigate feasibility of intraoperative image fusion during liver surgery. In a first step towards implementation, the Philips PercuNav navigation software is investigated in a phantom environment instead of a clinical setting, hence the implications of this phantom study are deficient for clinical settings. Despite obvious differences between phantom environment and clinical environment, some findings might also apply and serve as an indication for clinical application.

Whereas other investigations use tissue registration error, fiducial registration error or root-mean-square error [69–72], interests lay in how accuracy is distributed in relation to the registration area. Therefore, the term of local registration error (LRE) was introduced which was a useful concept in this research.

The registration method of the used software assumes rigidity of the phantom during co-registration. In case of non-deformation measurements, results were as expected for the plane-based registration, though a higher number of measurements might provide a higher reliability. Local registration errors of less than 5 mm are in accordance with accuracy measurements of other studies where live ultrasound is co-registered with other modalities in phantoms [73–75]. More than 4 cm away from the center of registration, LREs tend to increase quickly. Based on this phantom research, we are in agreement that these registration methods are considered sufficient in case of local application in the registration of real-time US to diagnostic CT or MR data.

The comparison of centrally and globally selected registration points in the point-based registration of experiment B is difficult for interpretation. First of all, measurements in the global point registration are distributed unilateral to the center of registration while for central point registration distribution is equally. Next to that, more measurements should have been performed since a lack of consistency in point selection for accuracy measurement presumably made results difficult. Nevertheless, errors around 5mm are acceptably low in point-registration.

Experiment C shows that the LRE remains the same when registration takes place on a deformed phantom in the -2 to +2 cm area of the registration center, for both types of registrations. As seen in experiments A and B, LRE increase when the distance to the registration center is increased. When measuring more than 4 cm away from the registration center, LREs start to get larger than 10 mm.

The effects of deformation during experiment D might be larger than depicted in Figure 2.14 due to the relatively unreliable post-processing method. Increased error bars in the areas more distant from the registration area indicate that registration accuracy becomes unreliable due to effects of deformation at this distances. However, at the -2 to +2 cm area increases of LREs mostly lie within an acceptable range of 10 mm. An increase from 3.0 ± 1.5 mm to 6.3 ± 3.5 mm is noticed in the ± 2 cm region for the point-based registration. These results are promising in relations to further research, when a maximum acceptable registration error of 10 mm is taken into account.

In the case of translation to in-patient use, it can be said that plane-based registration might become cumbersome since an identical axial plane on the US image has to be matched to the preoperative data. However, with this research, this is not substantiated. To limit possibly harmful effects of this registration method, the ultrasound transducer must be placed only in the nearby area, i.e., ± 2 cm of the reference plane. From the results of the plane-based registration with deformation, errors are still acceptably low in these regions. However, this method's chance of incorrect registration during surgery suggest to prefer the option of point-based registration with an expected lower chance of this error.

The impossibility for raw data analysis led to the need of an alternative post-processing method that become very sensitive to errors. Euclidean distances would have been easier and more reliable to calculate when raw data is analyzed. When orientation and location of the EM-tracked transducer are unknown, it is impossible to provide a direct link between coordinates in the ultrasound and MR volume. While performing the measurements, it was known that the transducer had to be moved at a slow and linear pace during the ultrasound sweep. Nevertheless, the rescaling in z-axis is a cumbersome assumption and prone for errors. Rescaling all fiducials' z-coordinates based on linking the two most outer fiducials to the original MR volume, assumes linearity in temporal and spatial space between these two fiducials. Next to that, the assumption that the ultrasound transducer moves with a constant pace is sensitive to fluctuation and dependent on the user.

Let us illustrate this assumption. The distance between start and end position is divided by the total duration of the 3D sweep. The ultrasound transducer is moved over the phantom surface with an approximate constant speed of 2.0 cm/s. With the impression that movement is at constant speed, for instance a rough fluctuation of 25% of the speed is present, i.e., speed is within 1.5-2.5 cm/s boundaries. In case of this quite big fluctuation, a deviation in z-axis registration is estimated as maximally 5 mm. This might be overcome by manually assigning a z-coordinate to each pair of registration points. Nevertheless, errors in z-direction are not specifically larger than errors in the x- or y-direction.

Notwithstanding difficulties and assumptions during post-processing, results of this research show room for functionality and applicability with an acceptable accuracy. Even when a vessel visible in the MR volume is incorrectly superimposed on a vessel in the ultrasound slice, it might be of functional information in finding a tumor during surgery. For intraoperative image registration with the purpose to act as surgical navigation technology, registration errors are acceptable in the range of 5 to 10 mm as consensus of surgeons involved in this project. From that perspective, results based on this phantom study are in compliance with these expectations. Following these results, simulating just the relatively small deformation of 30°, an acceptable registration error is promising, between -2 to +2 cm from the registration center and perhaps also within -4 to +4 cm. In these settings and circumstances, acceptable safety margins lay between -2 to +2 cm along the z-direction of the registered volume. Further research is necessary in terms of *ex vivo* and *in vivo* application, as well as for investigation of automatic co-registration which was not examined here.

2.5 Conclusion

A deformable liver phantom was constructed and subjected to accuracy measurements after multimodal image co-registration. In cases with and without deformation, plane-based as well as point-based registration of US to MR and CT resulted in an acceptable registration accuracy less than 0.5 mm in the adjacent phantom volume. This research indicates local possibilities for *in vivo* liver applications, however, further research is necessary to test the described possibilities.

Chapter 3

Ex vivo experiments

Summary

Subsequent to experiments in a controlled phantom environment, further investigation of co-registration of preoperative MR with live ultrasound is performed in an *ex vivo* setting. The goal was to perform point-based and plane-based registrations in an *ex vivo* setting and subsequently to assess accuracy of these registrations. Three specimens were obtained after different hepatectomies, all containing at least one lesion. Preoperative MR scans from these specimens were used for co-registration with live ultrasound. Deformation was minimized when possible during these experiments. Several point-based and plane-based registrations were performed. Raw data retrieval was impossible; hence an alternative post-processing method was developed. In addition to the methods of the phantom experiments (link), a SIFT-based method was used to detect features for accuracy assessment. Registration accuracy was high directly at the lesion borders. High deformation of the specimen in the ultrasound images in comparison to the preoperative situation was clearly noticeable towards edges of the specimens. Deformation caused by vessel collapse, blood outflow and extracorporeal displacement of the specimen contributed negatively. Additionally, the SIFT-based method was not applicable as a just accuracy assessment in these settings. *In vivo* experiments are required to describe more feasibility for intraoperative application.

3.1 Introduction

In the previous chapter the options for co-registration of intraoperative ultrasound with preoperative MR scans in a controlled phantom environment were explored, it is necessary to further investigate options towards eventual intraoperative implementation. For that reason, the focus of this research is shifted into using co-registration of a preoperative modality with live ultrasound in an *ex vivo* liver setting.

Previously performed research on the constructed liver phantom has given us insights in registration options and restrictions in terms of local registration accuracy. With these observations, it is desired to see whether results are translatable towards *in vivo* application. With this imaging-based navigation as a new technology in oncological liver surgery, *ex vivo* experiments on resected liver specimens are desired prior to intraoperative use of MR-US fusion.

Fusion of preoperative imaging with live ultrasound on *ex vivo* liver specimen has been performed previously in order to determine feasibility of local ablation [73, 76]. In these studies, CT scans to co-register the ultrasound to were acquired after resection of the (calf) livers. However, in the current research, instead of scans after resection we are combining MR scans before resection with live ultrasound.

In this chapter, we describe the findings concerning co-registration of live ultrasound and preoperative MR scans in several *ex vivo* liver specimens after surgical resection, using a fusion imaging system that can combine live ultrasound with different preoperative modalities based on previously described and used co-registration methods in case of the phantom studies. The goal is to perform point-based and plane-based registrations in an *ex vivo* liver setting and to assess accuracy of these registrations.

Visual inspection of the performed registrations is not sufficient in terms of qualitative assessment, accordingly a quantitative measure for registration accuracy assessment is required. As described earlier (Section 1.2.5), manual influences in this accuracy assessment cause a high sensitivity for errors due to inter-observer and intra-observer variability. Therefore, automatic feature detection with help of the SIFT algorithm is explored for application in for assessment of registration accuracy between images from different modalities.

3.2 Materials and Methods

3.2.1 Inclusion of Specimens

For *ex vivo* experiments, specimens were obtained after different hepatectomies. To enlarge chances of functional measurements, surgical resections had to result in relatively big parts of resected human liver, e.g., as is the case in hemi-hepatectomies or segmentectomies. At least one lesion of radiologically distinguishable size was required to be present in these resected specimens. An MR scan with an mDIXON scan after 20 minutes needed to be accessible. Concerning these scans, it was necessary that quality was good enough that co-registration was expected to be feasible, i.e., vessels and lesion(s) can be distinguished from liver parenchyma. All *ex vivo* measurements were coordinated with the department of pathology and were performed within the first two hours after resection of the specimen at the department of radiology.

3.2.2 Experiment Setup

The same ultrasound machine is used for the *ex vivo* experiments as for the previously performed phantom experiments, i.e., the ultrasound platform EPIQ7 (Philips Healthcare, Best, The Netherlands). The connection between the preoperative MR scan and the live ultrasound is established by the software module PercuNav, with help of an Aurora electromagnetic tracking system (NDI, Waterloo, Ontario, Canada). The resected liver specimen is positioned in such a way that we can perform a registration. Also, deformation is minimized in comparison with the intraoperative state. For this, no additional positioning tools or support is used. An EM patient tracker is fixed underneath the liver specimen, providing a reference for the tracked ultrasound probe (Figure 3.1). The planar electromagnetic field generator is placed and fixed above the work field. In this way, the reference tracker, the resected liver specimen and the tracked US transducer are positioned within the field of view of the EMFG. Metal-like objects are kept away from this field of view to limit any possible distortion of the electromagnetic field.

In each of the performed experiments, point-based and plane-based registrations were performed upon the resected specimen. Dependent of the permitted time to spend measurements on the specimens (due to the limited availability), linear and curved transducers were used to acquire data. Several images and videos were acquired per specimen after registration has taken place.

3.2.3 Post-processing

Qualitative assessment of registration accuracy by visual inspection is not sufficient, therefore accuracy assessment in a quantitative way is necessary. As described during the phantom study (Section 2.2.7), possibilities of determining this accuracy are limited in the software package of PercuNav: the Registration Fit Value limits us in analysis of the raw data and causes a lack of information. Therewith, an accurate analysis of MR-US registration is inhibited. Alternative methods are therefore required to analyze local registration errors.

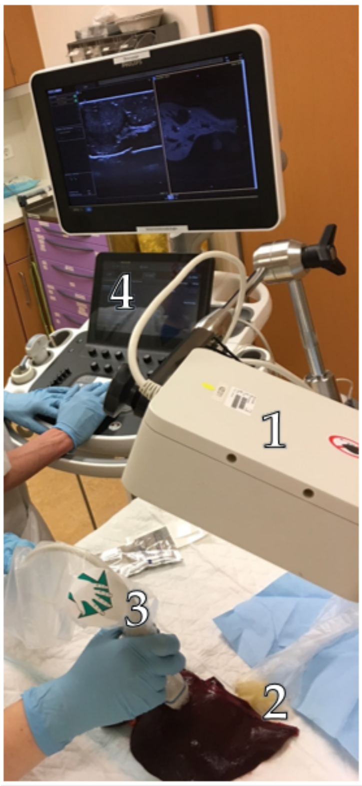

FIGURE 3.1: Overview of the setup of an *ex vivo* measurement, with elements of the setup 1) the planar EMFG, 2) the EM reference tracker under the liver specimen, 3) the EM-tracked US transducer and 4) the ultrasound system.

Calculation methods for the quantitative registration accuracy assessment took place with different methods. First, the manual calculation took place in the way it was used in the registration accuracy assessment of the phantom study (Section 1.2.5). This method resulted in two error measurements; a 2D RMSE without the temporal to spatial z-axis conversion, and a 3D RMSE with the temporal to spatial z-axis conversion. Opposite to these two methods, the options for a third method with a semi-automatic intention were explored, based on scale-invariant feature transform. This third method consists of four steps, i.e., i) slice selection, ii) feature extraction with SIFT, iii) feature match inspection, and iv) z-coordinate extraction. A post-processing pipeline for these steps is constructed in Matlab (version 9, R2017a, The MathWorks, Natick, MA, USA).

As in the manual method, the input is a video constructed as a DICOM file. Just as in the phantom research, points in each slice are described with x- and y-coordinates and for z a temporal unit. Each slice from this file is composed of 4 quadrants, namely one quadrant with an ultrasound slice, one with the co-registered MR slice, one with a fusion overlay of the previous two and one with a 3D rendering of the US probe with respect to the patient's body (Figure 3.2, step 1).

It was desired to extract a fiducial from the ultrasound slice, and correlate it to a corresponding fiducial in the co-registered MR. In case of an imperfect co-registration, the corresponding fiducial is not in the co-registered MR slice but in that MR slice of adjacent to this slice. To find the corresponding fiducial in an MR slice different from the co-registered slice, in case of imperfect co-registration, an ultrasound slice was compared to multiple slices from the co-registered MR volume. To facilitate comparison, first, multiple MR and US images were extracted. This was performed in the region where we are interested in the registration accuracy, for which upper and lower boundaries are indicated (Appendix B for pseudocode). Each fifteenth ultrasound slice is compared with each fifth slice within the selected boundaries (Figure 3.2, step 2). Cropping of the ultrasound image is performed to limit the area to search for features.

After slice selection, each extracted MR image is sharpened by subtracting a blurred version of the image itself. For the blurring, a Gaussian low-pass filter with a sigma of 2 pixels was used. Subtraction of the blurred version of the image results in edge enhancement of the original. Each extracted ultrasound image was applied with square-shaped 2D 5x5 median filter to reduce remaining speckle noise while preserving the edges [77]. The median filter replaces each input pixel with an output pixel containing the median value of the 5x5 neighborhood around the input pixel. These two procedures are performed to bring the two types of images closer together and attempt to more easily find corresponding SIFT features.

Consequently, feature extraction with SIFT took place to find useful landmarks in the selected US and MR slices. As described in the introduction chapter, the SIFT algorithm is used to detect and describe local features in images. These features are stored as keypoints with its location, scale and orientation in radians. Corresponding descriptors are stored in a 128-dimensional vector.

In the DoG scale space five octaves with three levels per octave are searched for keypoints. The non-edge selection threshold is set at 10 pixels. A peak threshold and normalization and descriptor normalization threshold are not further specified. The variance of the Gaussian window that determines the descriptor support is set at two spatial bins. The descriptor magnification factor is kept at a default setting i.e., three, meaning that the scale of the keypoint is multiplied by this factor to obtain the width (in pixels) of the spatial bins [78].

Inspection was needed to assess whether a match by the SIFT algorithm is indeed acceptable as a match (i.e. false positive matches reduction). This results in acceptation of a match pair only when detection of that match pair is performed by the algorithm and when visual inspection after detection assessed this match. A match was accepted as correct if locations of the features were assigned to the same anatomical fiducial in both US and MR images. Differences in x- and y-coordinates between two fiducials of a match were calculated without difficulty by translation of the MR quadrant to US quadrant.

To accomplish the calculation for the 3D registration error, the z-coordinate was added in the fourth step of the algorithm. The z-coordinate was necessary to be retrieved for the feature in the MR image and the feature in the US image. For that, the location of the detected keypoint in MR is retrieved by manually finding the corresponding location in the original MR volume that was used as input for the co-registration). The z-coordinate of the US fiducial is chosen by linking the initially co-registered MR slice to the corresponding location in the original MR volume.

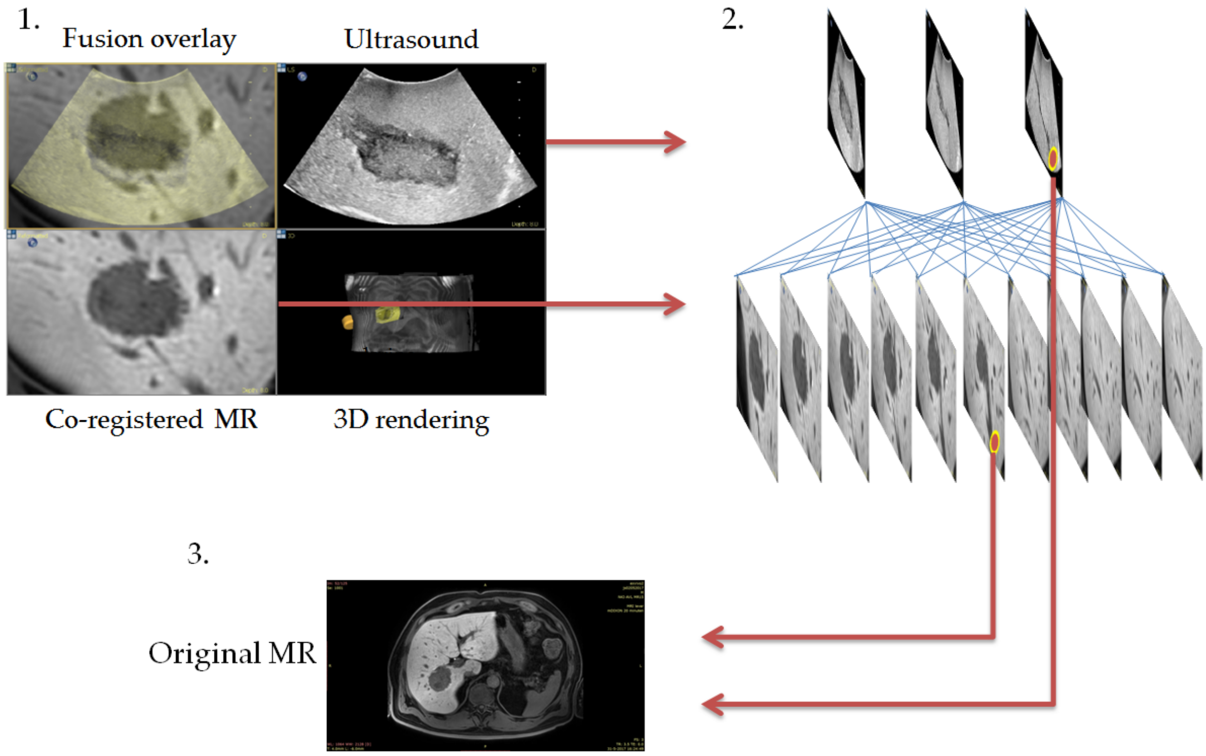

FIGURE 3.2: Schematic overview of the post-processing method. The input image is positioned in the upper left part, consisting of four quadrants. The co-registered MR quadrant and ultrasound quadrant are used for the SIFT algorithm. As an example, in this image a feature is found in an MR slice, as well as one in an ultrasound slice. With the x- and y-coordinates of these images already known, the z-coordinate is retrieved from the corresponding location in the original MR volume.

3.3 Results

For the experiments, three resected specimens were used. The first specimen was collected after a left hemihepatectomy (consisting of segment II, III and IV) with a solitary colorectal liver metastasis (CLM) with a maximum diameter of 38 mm in segment IV (Figure 3.3). The second specimen was collected after a right hemihepatectomy (consisting of segment V to VIII) containing a CLM with a maximum diameter of 54 mm on the border of segment of the consisting segments. The third and last specimen was collected after a right posterior hepatectomy (segment VI and VII), consisting of two CLMs with maximum diameters of 22 and 7 mm.

During experiments on the first and third specimens, only the linear transducer was used. Measurements on the second specimen were performed with the curved probe and linear transducer. Decisions in the use of transducers were made to get experience and insights for both transducers, the limited time inhibited more use of both transducers as well. A registration error was 'successful' when co-registration of US and MR was assessed as sufficient after visual inspection by the two or three users during the experiments.

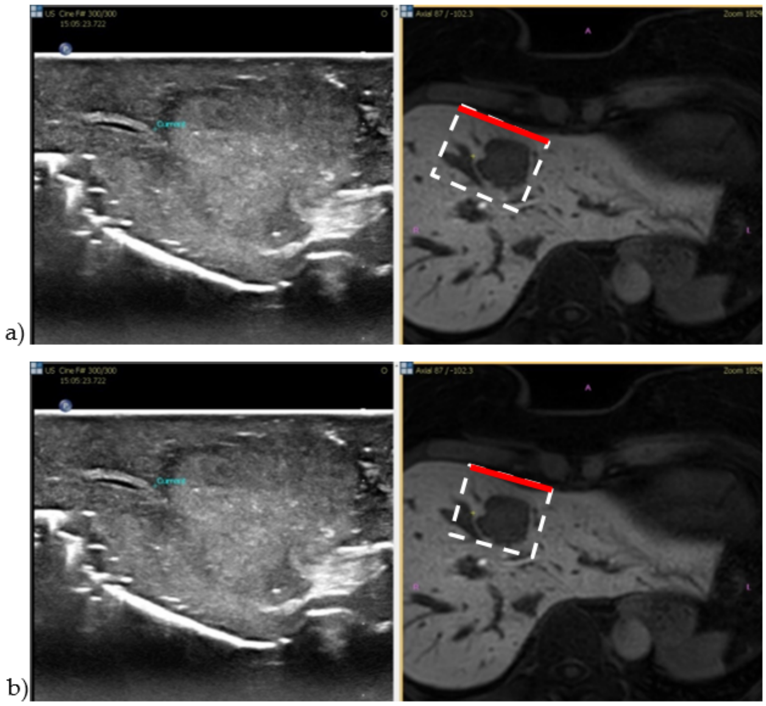

FIGURE 3.3: Points used for co-registration in the first *ex vivo*, after a left hemihepatectomy of the segments II, III and IV. Two pairs of matched images for point-based registration with ultrasound on the left and MR slice on the right. The white box on the MR slice roughly corresponds with the ultrasound image on the left. Sizes of the left and right images are not the same since zooming can take place in the MR slice. Blue (ultrasound) and yellow points (MR) resemble the co-registered points.

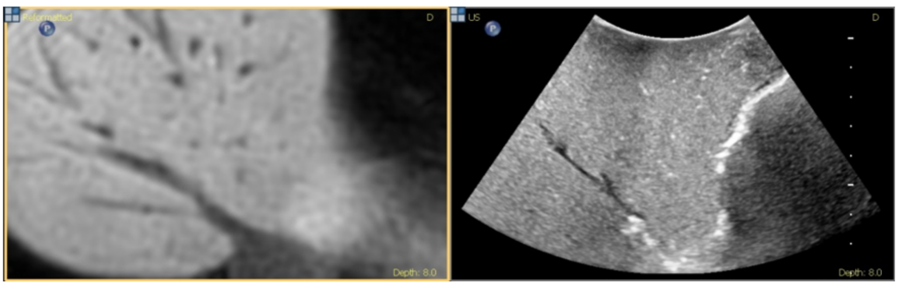

FIGURE 3.4: A screenshot from the co-registered image set (MR left, curved US right) after point-based registration in the second *ex vivo* experiment. Hyperintensities are visible at the right, the location of the resection plane. One main branch is visible in both the images, which is the right hepatic vein. The other vessels are not visible in ultrasound due to vessel collapse.

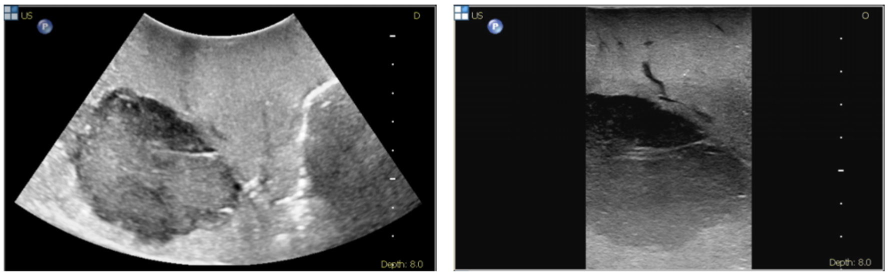

FIGURE 3.5: Comparison of the curved ultrasound probe with the linear one at the approximately same location. The lesion is clearly visible in both images, however, a difference is present in visibility of the branches superior to the lesion.

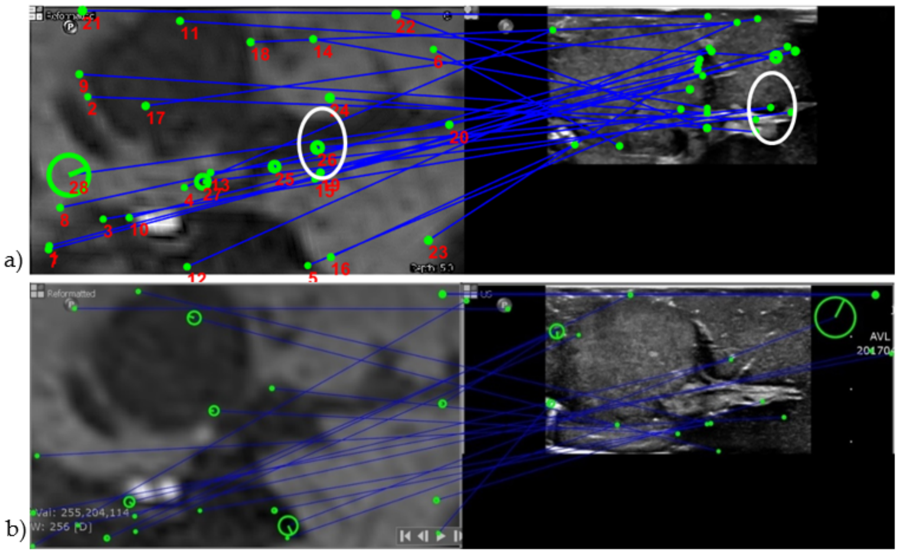

FIGURE 3.6: a) Example of a resulting image of SIFT pairs with a manually accepted match depicted by the white ellipses. b) Example of a resulting image of SIFT pairs which were accepted by the algorithm's condition, but not by manual inspection.

For the use of the 3D RMSE calculation after manual point-matching (Figure 3.7), the same points are used as in the table on the left that were used for 2D RMSE, but now the z-direction is included in the RMSE calculation. Results after a point-based registration are compared for 2D and 3D RMSE of the manual matching and 2.5D RMSE of the SIFT matching. Officially, it is not a 3D SIFT algorithm but 3D positions are approximated with help of the 2D slices, therefore the 2.5D. Results of a point-based registration in the second *ex vivo* experiment are also depicted, when a curved transducer was used (Figure 3.8). For the 2.5D RMSE based on SIFT features, the RMSE is calculated if a pair of SIFT features was accepted. If that was the case, the RMSE will be related to the US plane it corresponds to. Further data analysis on these *ex vivo* specimens is not performed.

***Ex vivo* nr. 1 – Successful point-based registration**

2D RMSE (cm) Manual matching

Fiducial	Error x	Error y	2D RMS
1	0.24	0.17	**0.29**
2	0.02	0.14	**0.14**
3	0.03	0.04	**0.05**
4	0.04	0.30	**0.30**
5	0.30	0.53	**0.60**
6	0.30	0.10	**0.31**
7	0.21	0.24	**0.31**
8	0.23	0.11	**0.26**

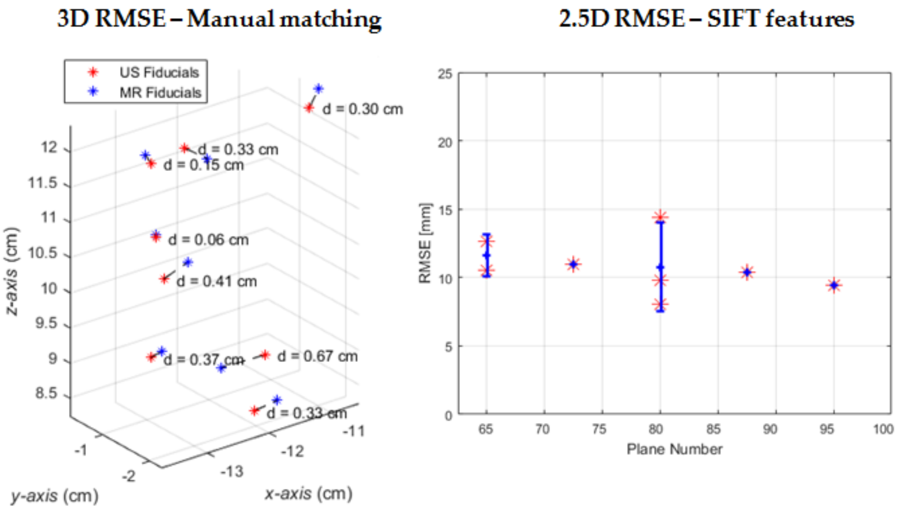

FIGURE 3.7: Results after a point-based registration, after the first *ex vivo* measurement using a linear transducer. The table on the left and the figure in the middle used the same fiducials for these calculations after manual fiducial matching, calculation difference lies in whether the z-coordinate is included for calculation. For the 2.5D SIFT method, calculated RMSEs are shown per corresponding US slice (right).

***Ex vivo* nr. 2 – Successful point-based registration**

2D RMSE (cm) Manual matching

Fiducial	Error x	Error y	2D RMS
1	0.72	0.25	**0.76**
2	0.47	0.12	**0.49**
3	0.27	0.04	**0.27**
4	0.37	0.41	**0.55**
5	0.07	0.42	**0.43**
6	0.06	0.20	**0.21**
7	0.38	0.02	**0.38**
8	0.40	0.25	**0.48**

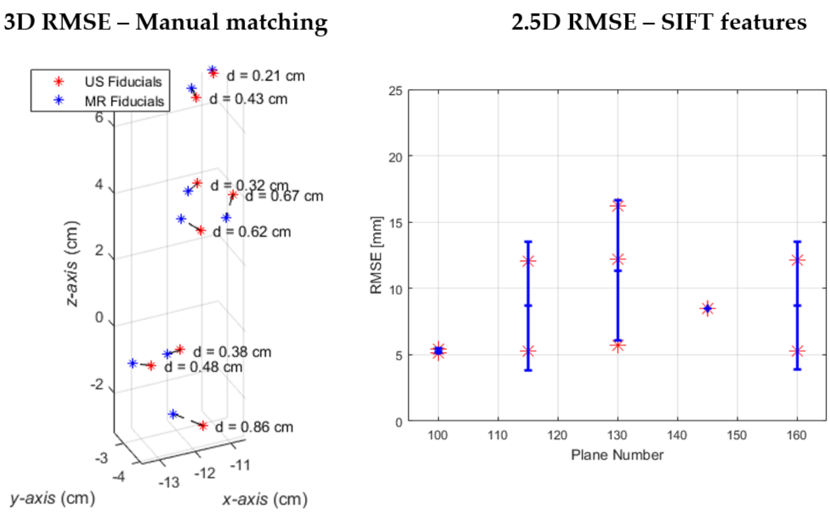

FIGURE 3.8: Results after a point-based registration, after the second *ex vivo* measurement using a linear transducer. The table on the left and the figure in the middle used the same fiducials for these calculations after manual matching, calculation difference lies in whether the z-coordinate is included for calculation. For the 2.5D SIFT method, calculated RMSEs are shown per corresponding US slice (right).

3.4 Discussion

In general, we were able to perform point-based and plane-based registrations during all three experiments, therewith it was possible to perform measurements during all experiments. Unfortunately, several logistical and organizational problems with the ultrasound machine limited our possibilities to perform experiments on *ex vivo* specimens, due to restricted flexibility and availability of the ultrasound system we require. Initially, we aimed to perform *ex vivo* measurements on more than three resected specimens. However, in retrospect, this amount was already satisfactory in terms of determining usefulness of these *ex vivo* measurements. The step to move on to *in vivo* experiments could preferably have been concluded earlier, if measurements would have been performed in quicker succession.

During some experiments, we encountered difficulties with the registration, primarily related to the limited clinical ultrasound skills of the people involved in the in the experiments. Problems were mainly present in orientation of the resected specimen with respect to the preoperative situation, or in selection of the appropriate landmarks. The second challenge presumably will be eliminated in more experienced users such as surgeons and radiologists. However, visual inspection and the 3D RMSE after manual matching still showed good matching around the tumor if co-registration based on the lesion borders took place. Additionally, orientation of the probe with respect to the liver surface in the 3D rendering was a helpful tool to visually examine if co-registration appeared to be correct. In most cases, this was appropriate.

A larger specimen did not contribute to a better experiment, as first was expected due to an increased volume and therewith number of vessels to co-register to. It is thought that the volume and its weight contribute to the collapse of vessels and the bigger chance of deformation of the specimen. The use of the curved ultrasound transducer caused an increase of the collapse of vessels and negatively contributing manipulation of the specimen's shape. The dry surface of the specimen contributed more deformation due to increased compression as well as a rough and inconsistent movement of the transducer (in particular when the curved probe was used). Movement of the transducer with a constant pace appeared to be quite difficult. Since that requirement was present for the RMSE calculation with manual fiducial selection, a comparison between 2D and 3D RMSE was made. In this way, influence of the z-coordinate was distinguishable.

Deformation due to the collapse of vessels was noticed in all measurements. Next to collapse due to the weight of the tissue, this can be explained by the lack of perfusion and blood containment in comparison with the intraoperative situation or the situation during MR scan acquisition (Figure 3.4). The resected part of the liver is no longer attached to its surroundings in the abdominal cavity and it has lost its relation to the rest of the organ. This is detrimental to successful matching since the ultrasound image is likely to look different from the preoperative MR image.

Though visual inspection might indicate a good co-registration of a preoperative scan and live ultrasound, ideally a quantification of registration accuracy is desired. A good attribute of a system would be to provide the user with a measure of registration accuracy of co-registration of the modalities. In the case of these experiments, the PercuNav system returns a Registration Fit Value "which is only a guideline to help the user obtain an accurate registration", i.e. the user must confirm accuracy by assessing the fusion images. While this system is validated in percutaneous use and such a value would satisfy, this is not the case in open surgery, hence a quantitative assessment after a performed registration was desired before intraoperative use can take place. The developed semi-automatic method using SIFT-based feature detection did not cover the desired accuracy assessment for several reasons.

SIFT has been proven to be useful in applications with different modalities [56, 57, 79]. In this performed research, the MR images are too different from the US images to find representative matching pairs. Factors that contribute to this are i) the characteristic ultrasound speckle (granular noise) in the ultrasound images and ii) the blurry edges in the MR image due to magnification of the image. It was attempted to reduce these effects with the described filtering methods. A change was visible when we compare extracted features from images with and without these filters, though the effects did not contribute enough to make the use of SIFT a successful method. Different filtering methods such as nonlocal means-based speckle filtering might contribute to improvements [80]. Settings of the current algorithms produced different types of features in US and MR, resulting in too local feature description. For that, e.g. Maximally Stable Extremal Regions (MSER) results in less local detection as a blob detection method by attaching elliptical frames to regions with co-variant intensities [81]. With this method, it might be useful to detect elliptical structures such as vessels or tumors in a set of MR and US images (Figure 3.9).

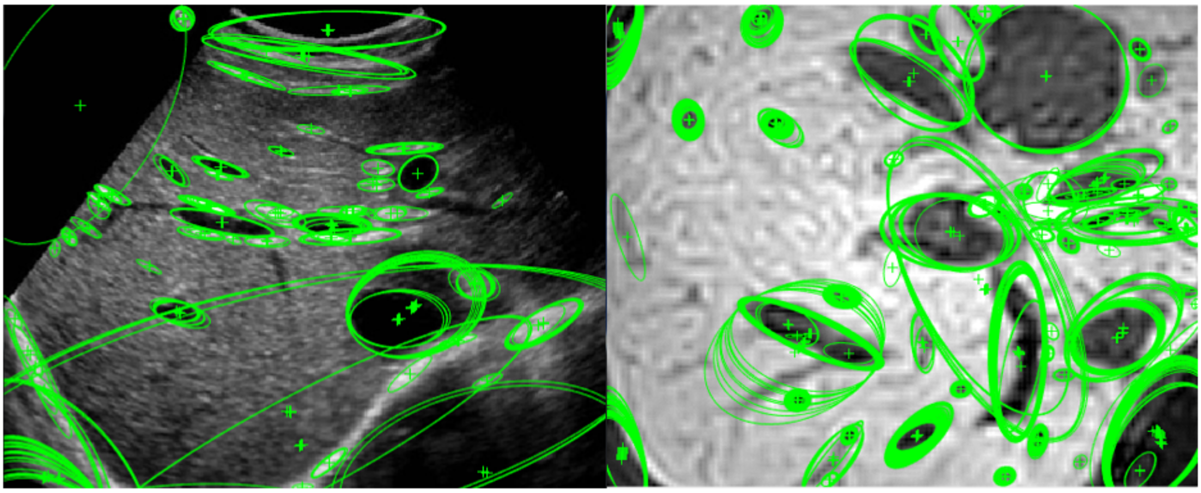

FIGURE 3.9: Example of MSER-based feature extraction in the ultrasound image (left) and MR image (right). As visible, circular and elliptical shapes are extracted with a plus sign depicted as center.

Feature selection was aimed for with the goal of automation of fiducial selection to calculate registration accuracy. Nevertheless, the used pipeline still required a lot of manual input, e.g., in z-coordinate assignment, but more important in supervision of the feature match after the SIFT algorithm. Another drawback is that the used method, with the slice selection, still is a 2D-2D comparison of features where a pair of corresponding fiducials are almost always in a set of non-co-registered US and MR images. Translation to 3D application of SIFT (or MSER) can be considered for 3D accuracy assessment of co-registration [82, 83].

Results from this research, keeping aside the SIFT method, more *in vivo* research is required. Further *ex vivo* measurements will not add in valuable information in these settings, mainly due to the great difference. Translation of this research into *in vivo* application is therefore difficult, since shape of the liver and filling of its vessels is of a great influence in the chance of a successful (and useful) registration. Though, towards *in vivo* experiments it is positive that the lesions present in the resected specimens were successfully matched, with locally a high accuracy on the borders of these lesions.

3.5 Conclusion

Co-registration of a preoperative MR scan with live ultrasound was applied in an *ex vivo* setting on human specimens after surgical resection. Though deformation largely influenced the shape of the liver in comparison to the preoperative MR situation, these experiments showed good matching of the lesions in the images. A SIFT-based method was developed in attempt to quantify the accuracy of co-registration of the two modalities, however, this method is not applicable in these settings. *In vivo* experiments are expected to contribute more in terms of describing feasibility of clinical implementation of MR-US co-registration during surgical resection of liver lesions.

Chapter 4

Towards Clinical Implementation

Summary

In the previous chapter the options for co-registration of intraoperative ultrasound with pre-operative MR scans in an *ex vivo* setting were explored, now a first introduction of the used co-registration setup in the intraoperative setting is performed and discussed. Only from this one time application, we already witnessed several lacks in the current PercuNav setup. Several factors from these experiences are taken into account for the development of an in-house system. Development of an alternative system has started, to replace a currently used system as PercuNav in the future. Further steps in this development are being described, as well as challenges that need to be overcome to foresee problems in e.g. calibration and intraoperative use.

4.1 Intraoperative Introduction of PercuNav

It was not possible to investigate the options for *in vivo* application during surgery in multiple individuals, due to the previously described logistical problems. The setup as being described for the phantom and the *ex vivo* settings has only been tested on one patient during open liver surgery. This was in the case of a surgical resection, performed on a patient that had a solitary colorectal liver metastasis in segment VII/VIII. In this patient, only point-based registration measurements were performed. For the registration, one 3D ultrasound sweep was recorded with a tracked 1-5MHz curved-array ultrasound transducer. Prior to the sweep, the liver was totally mobilized. The sweep was acquired during the expiratory part of the breathing cycle, at the same time, the liver was kept in the same place with a hand of the surgeon. The organ remained fixated in the same location (i.e., with hand support) during all ultrasound-based measurements. Four anatomical fiducials were chosen for registration in this sweep, with the EM location and orientation of the ultrasound transducer being linked. Bifurcations of the hepatic vasculature were used for fiducials. Subsequently, these fiducials were matched to the corresponding locations in the MR volume that was selected for co-registration.

A 5DOF patient reference tracker (Figure 4.4) was placed on the exterior side of the abdominal wall, outside the sterile field but within the field of view of the planar field generator. This is performed as a replacement of a sensor that is directly fixated on the liver. A consequence is that there is no compensation for the patient's breathing.

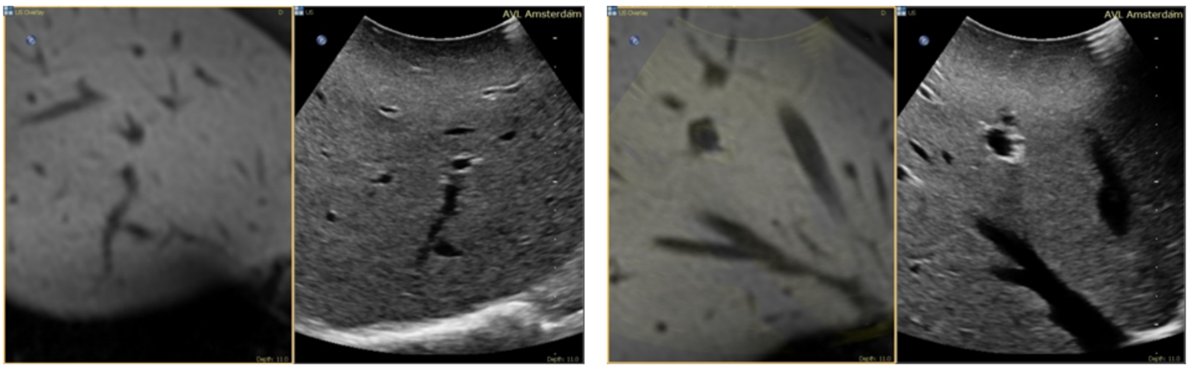

FIGURE 4.1: Two screenshots of intraoperative use of PercuNav, after point-based co-registration of a preoperative MR scan (left one of a pair) with live ultrasound (right one of a pair). Though the co-registration was imperfect, corresponding vessel structures can be recognized in both the US and MR images. Registration errors were 10.6 ± 5.5 mm and 6.4 ± 2.5 mm for the image pairs.

Several measurements were performed, resulting in a series of recorded images. Instead of displaying images with four quadrants as in the previous chapters, only the live US image with the co-registered MR were shown in accordance with the preferences of the operating surgeon (Figure 4.1). Whilst using point-based registration, we were able to link the preoperative MR volume to the live ultrasound images. Visual inspection of these co-registered images was assessed as reasonably good, based on several factors. First of all, the liver contours matched in a decent way. With that, orientation of the transducer with respect to the MR volume was correct. Lastly, main branches in the US matched properly with the co-registered MR slices. Postoperative accuracy assessment was performed by assessing the MR-US co-registration of anatomical fiducials, for bifurcations and centers of vessel cross-sections. In the left image of Figure 4.1 a 2D RMSE of 10.6 ± 5.5 mm was calculated, based on four point pairs of anatomical

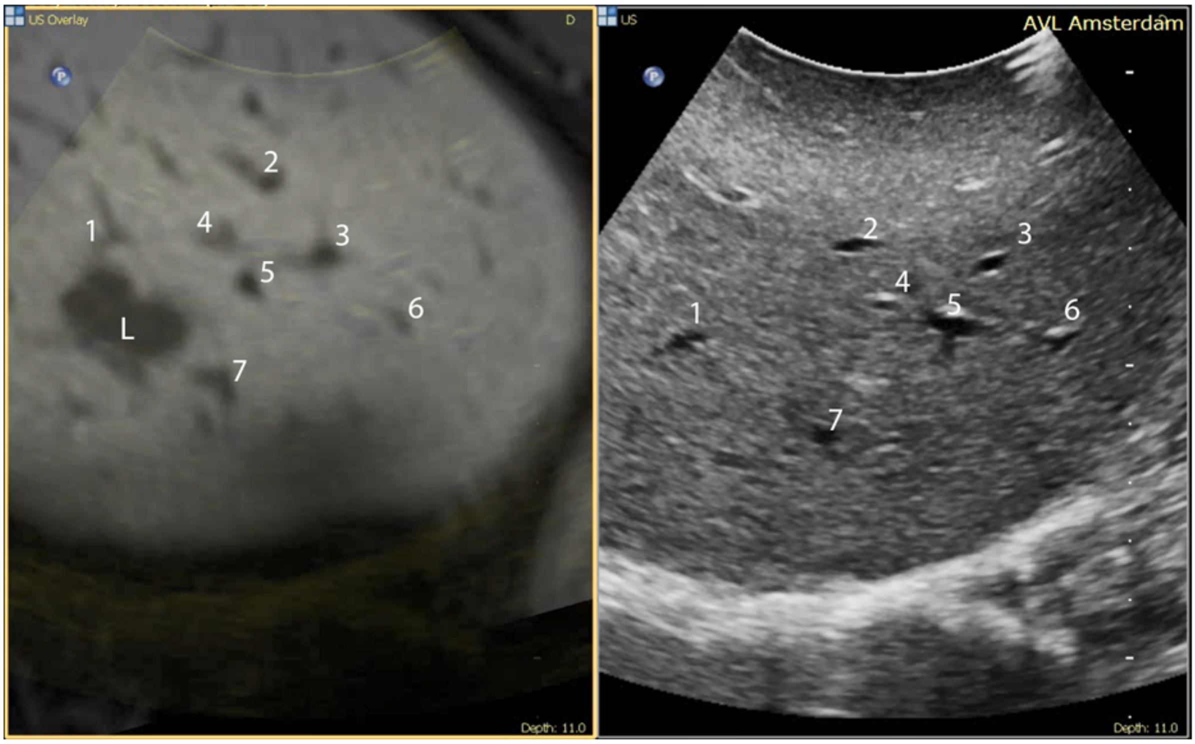

FIGURE 4.2: A captured image of the one *in vivo* use with the ultrasound (right) and the co-registered MR image (left). Seven pairs of vessels are numbered, with in the co-registered MR slice the lesion (L) visible while in this ultrasound image it is not present. This is an exemplary case of an isoechoic lesion.

fiducials in both MR and US. In the right image of Figure 4.1, the 2D RMSE was 6.4 ± 2.5 mm (also based on four point pairs). A 3D registration error could not be calculated in these cases.

With this patient being the first registered intraoperative application of the PercuNav during liver surgery, potential benefits were illustrated immediately. In ultrasound imaging, a lesion may appear as isoechoic, i.e., distinction from the surrounding healthy liver parenchyma is not possible due to the same echogenicity. This occurs in focal nodular hyperplasia and also frequently in colorectal liver metastases [84]. This particular patient had an isoechoic CLM, the surgeons could not distinguish the lesion intraoperatively from the healthy liver parenchyma. With co-registration of modalities, we could link the location of the CLM visible in MR to the expected location in US.

In patients who are treated with neoadjuvant chemotherapy, a good response causes a decrease in volume of the lesion. This can result in a complete radiological response in some patients (i.e., “vanishing lesions”). These lesions, when they remain further untreated, can cause recurrence [85]. This is why we aim to remove the tissue area of where the tumor presented itself. As one can imagine, this can be cumbersome. Therefore, the combination of live ultrasound with a preoperative MR scan might be of additional value. In this case, the location of the colorectal liver metastasis was in MR is now linked to the intraoperative location where we could expect any pathological remnant of the lesion (Figure 4.2). If this patient did not have an isoechoic lesion but a complete radiological response, the MR-US co-registration would have been a clear benefit as well. Accuracy was assessed by using the centers of the vessel pairs for RMSE calculation, resulting on a registration error of 14.2 ± 3.7 mm based on the seven used and visualized pairs. Despite this accuracy, the potential intentions for application of such a system are illustrated with this case.

To summarize, we can say that this solitary intraoperative introduction has shown additional insights to assess its feasibility. The setup was not ideal, e.g., with the use of the patient reference tracker outside the body. Nevertheless, a decent co-registration was performed between preoperative MR and intraoperative ultrasound. The potential benefits were demonstrated immediately in this case of an isoechoic lesion.

4.2 Limitations of Using PercuNav

This *in vivo* experiment was carried out while using a curved transducer. Since PercuNav is initially developed for percutaneous use only, a 1-5 MHz curved-array transducer and a 5-12 MHz linear-array transducer are the only compatible options for intraoperative use. This means that the intraoperative transducer cannot be used in this setup and is therefore excluded for possible use, leading to a missed absence of its functionality and its reach. With the compatible transducers being of a considerable size, ultrasound imaging of the posterior segments or near the dome of the diaphragm now is not possible even with extensive mobilization of the liver. Even if a PercuNav-compatible intraoperative transducer was available, being much smaller than the other compatible transducers, at this moment a clip-on tool for fixation of the EM sensor is not available for such an intraoperative transducer. Next to that, the use of a curved-array transducer as was used here causes deformation since good image quality requires forcefully applying the transducer on the liver surface.

During the described intraoperative introduction of the PercuNav setup, an EM reference sensor (previously described as the patient reference tracker [Figure 4.4]) was placed on the side of the patient instead of directly on the liver surface. Not only does the liver move during surgery by mobilization and other movements by the surgeon, it is also susceptible to movement due to the breathing cycles. The need for a sensor on the liver is described with the following experiment.

For a percutaneous experiment in a healthy volunteer, an mDIXON scan was available (acquired with the same scanning protocols as in the *ex vivo* experiments). One ultrasound sweep was performed in which secondary bifurcations of the hepatic and portal veins were used for co-registration with corresponding fiducials in the MR volume. A 3D ultrasound sweep for co-registration was acquired during inspiration, so that the liver was available for easier imaging when the transducer was placed subcostally towards the liver. The match was accepted and showed a decent registration. Thereafter, while keeping the transducer at the same position with respect to the volunteer and the EMFG, the volunteer performed a complete breathing cycle. A comparison is made between the recorded image of the inspiratory and expiratory state of the liver (Figure 4.3). This shows that while the co-registered MR image remains the same, the ultrasound image changed showing completely different segments of the liver. This experiment showed the effect of breathing on movement of the liver, thereby resulting in change of ultrasound imaging. In percutaneous interventions, a breath hold can support maintaining a correct co-registration, however, during surgery a breath hold technique is not appropriate as patients are sedated and cannot control their breathing. This strongly supports the necessity of EM sensor placement on the liver surface to track movement of the liver. In this way, we are not only able to compensate for displacement of the liver with respect to the EM field. Also, when the sensor is fixated on the liver surface in near vicinity of the volume of interest (VOI), we are able to partially compensate for local deformation and change in orientation when the transducer is pushed into liver surface with force.

The reference tracker that was used during phantom and *ex vivo* experiments was also used during the one time *in vivo* application (Figure 4.4). As stated, ideally this sensor is fixated on the liver surface, however, fixation of the specific sensor is cumbersome due to its considerable size and impracticality of temporarily fixation to the liver surface.

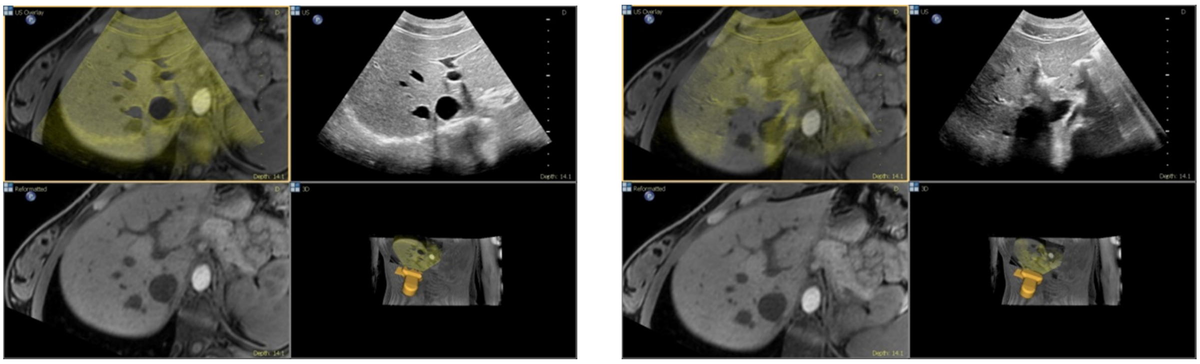

FIGURE 4.3: Comparison of inspiratory (left) and expiratory state (right). The lower left quadrants containing the co-registered MR slice stayed the same, while the ultrasound imaging has completely changed in the upper right quadrants.

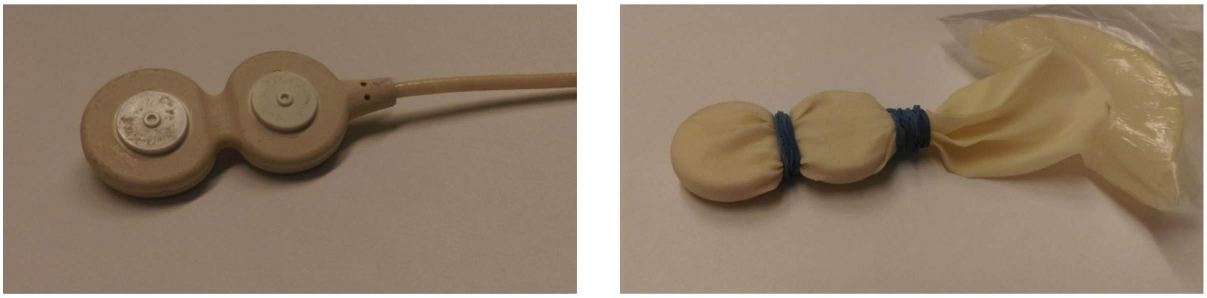

FIGURE 4.4: Patient reference tracker (left), with a sensor size of 4.5 x 2.3 cm. A latex probe cover (right) would be used when we would have made more *in vivo* introductions.

Automatic co-registration of preoperative MR to live US was desired to test, though it was not possible to test. The PercuNav software was developed for automatic co-registration of CT scans to US only, primarily based on vessel tree extraction (Section 1.2.3). Even though MR scans might contain more anatomical information being useful during surgery, it was not possible to investigate potential benefits of automatic co-registration of the MR scans as an input.

When the PercuNav system is used, we are not only limited in terms of compatibility for the choice of the ultrasound transducers. For this particular system, the only option for connection to an EMFG is the planar field generator which can be mounted on an adjustable positioning arm. However, in this institute using a TTFG is preferred above a PFG in liver surgery. This TTFG can be positioned under the patient mattress, therewith no obstruction is caused for the surgeon or the surgical work field. Research has shown that accuracy in the use of the TTFG and the use of different sensors in combination with this field generator is adequate during surgery [43, 86].

To summarize, we are limited in adjustment of several important settings in a closed system such as the PercuNav application. The limited choice in ultrasound transducers, intraoperative sensors and the compatibility with only one type of field generator, impedes direct clinical application in open liver surgery. Additionally, the automatic vessel-based co-registration is only capable to fuse preoperative CT with real-time ultrasound, and not preoperative MR with real-time ultrasound.

4.3 Development of an Alternative System

The pitfalls of current system lead to set out the options that we have. On the one hand, research could be continued, by maintaining to work with this closed system of Philips in which alterations of the current setup are limited. Another option is to develop an in-house alternative in which a lot of choices can be made to match several demands. The lack of raw data analysis, the restricted choice in types of ultrasound transducers, as well as the limited choice in EMFGs types and corresponding sensors altogether caused a change in course to start in-house development of an alternative system. Qualitative characteristics and practical considerations for the intraoperative use that the clinical implementation team is used to, contributed to this decision.

Steps for this development were started during the last half year. First of all, a switch has been made to another ultrasound system, i.e., BK Flex Focus 500 (BK Medical, Peabody, MA, USA), to enable more raw data analysis and a broad choice in transducer selection.

The transducer can be tracked by the same EMTS developed by NDI (Northern Digital Inc., Waterloo, Canada). This system has received considerable attention in the literature and has been introduced and further optimized in this institute for several other intraoperative applications as well [44, 69]. This system is needed to establish a connection between the ultrasound volume and the MR volume.

Practical development of this workflow is carried out by other researchers of this group. In this workflow, the link between the ultrasound images needs to be provided by the PlusServer from the Plus Toolkit [87]. PLUS is a public library for ultrasound. This software is developed for the readout of the NDI hardware data as well as the readout of the ultrasound image. Within PlusServer the data for the ultrasound and the EMTS (NDI) were combined into one data stream.

In-house software in terms of a processing pipeline is being developed. Right now, the first step is accomplished of establishing the link between the ultrasound and the electromagnetic field. A PNG image of a captured ultrasound slice is combined to the EM pose of the ultrasound transducer. Two ways of calibration, i.e., spatial and temporal calibration, are required as a next step in the process.

Spatial calibration is performed to compute the transformation between a phantom object coordinate system and the coordinate system of the tracking marker attached to the object. By following the fCal calibration algorithm in one single application, this can be performed by point matching using a tracked stylus [88]. For this, we use a calibration phantom to ensure reproducibility. This method is used in the PLUS project and uses a 3D printed model with multiple so-called N-fiducials. This phantom is used for pivot calibration, landmark registration and image calibration [89]. Subsequently, a temporal calibration is needed to determine the constant unknown temporal offset between data streams that are acquired by the EMTS and the US transducer. This is crucial, since temporal misalignment would result in spatial errors when the tracked tools are moving. This part of calibration is included in the named and used calibration software fCal.

4.3.1 Prospective Steps

A correct and precise calibration is essential. Accuracy of a consequent image co-registration is depending on a correct calibration of the tracked ultrasound transducer's pose. Therefore, tracking of this transducer needs to be executed in a consistent and reliable way. This results in the need of fixation of the sensor onto the transducer. The fixation must be performed in such a way that a change in the orientation or the position due to movement of the sensor with respect to the transducer is prevented. Firstly, this contributes to a repeatable and consistent calibration procedure, and secondly, to a preservation of this orientation when the transducer will be applied for intraoperative use. Transducers with corresponding clip-on tools from e.g. the PercuNav setup or other systems than the BK ultrasound cannot be used for the application that is aimed for right now. Adjustments are necessary in terms of designing a new clip-on tool to mount an EM sensor to the ultrasound transducer.

We need to fixate an EM sensor to a clip-on tool, which will be 3D printed for exact fitting on the ultrasound transducer. Inspiration for this can be sought in different existing types of ultrasound clip-on tools. Since the NDI Aurora tracking system is used for as EMTS, chosen is to use the Aurora 6DOF Cable Tool (Northern Digital Inc., Waterloo, Canada). The tool consists of a flexible cable with a 6DOF sensor in its tip that can be connected to the SIU (Figure 4.5). When the tip of this cable tool is glued on the 3D printed clip-on tool, a fixed transformation matrix of the ultrasound transducer to the EM coordinate system can be established. During surgery, the Cable Tool is expected to be clearly visible and less fragile than its alternatives.

As an alternative, an EM sensor can also be used which is compatible with the NDI Aurora system and already has a fixed orientation. This sensor is normally used in combination with a clip-on tool for the Philips PercuNav application of percutaneous biopsy. The already fixed orientation of the sensor might be beneficial, though this sensor cannot withstand autoclave circumstances. Therefore, the combination of a 3D printed clip-on tool with the cable tool is preferred since after a glued fixation the tool will be sterilized or cleaned for 20 procedures, before being disposed.

Several choices must be considered before development of the EM sensor and its attachment to the ultrasound transducer starts. Demands are that the attachment does not affect functionality and convenience during surgery. The clip-on tool must not influence the shape of the ultrasound transducer too much, since the surgeon must be able to hold it with ease and move it freely during intraoperative assessment of the liver. Therefore, the shape of the clip-on tool must not protrude too much. Additionally, the clip-on tool must hold the EM sensor in such a way that it does not damage the cable or the sensor in the tip by excessive bending or twisting. So, the sensor must be fixated onto the tool, though it may not break. The EM sensor must stay in a constant position after this fixation. Exactly the same position on the US transducer must be achieved every time it is attached since a small translational or rotational error will strongly propagate in the US image.

For the first steps in development, a BK curved-array transducer is used while ultimately, development of the application will be shifted towards an intraoperative probe. A clip-on tool has been developed to permanently fixate the 6DOF Cable Tool on a BK curved-array 8830 transducer (Figure 4.5). For development and fine-tuning of the calibration method it suffices to use a curved-array transducer for abdominal application instead of an intraoperative one. For now, the clip-on tool has been 3D printed of a simple plastic material. The tool will be printed in PEEK material when the final step to application in surgery will be performed [90]. This material is suitable for autoclave sterilization, i.e., the PEEK plastic is unaffected when it is exposed to saturated vapor at a temperature of 134° Celsius. The NDI Cable Tool that is mounted on this clip-on tool can stand these circumstances as well.

When the Cable Tool has been used 20 times, a new Cable Tool has to be attached to the old clip-on tool with corresponding costs. It can also be that the clip-on tool needs to be printed again when the old clip-on tool needs to be replaced, therewith also certain costs are at hand. When such a tool is used for 20 times, these costs become distributed over 20 used procedures making it more affordable. However, when a change between ultrasound transducers is necessary, a new clip-on tool needs to be developed for another type of ultrasound transducer.

Fixation of the Philips patient reference tracker directly on the liver surface is excluded for

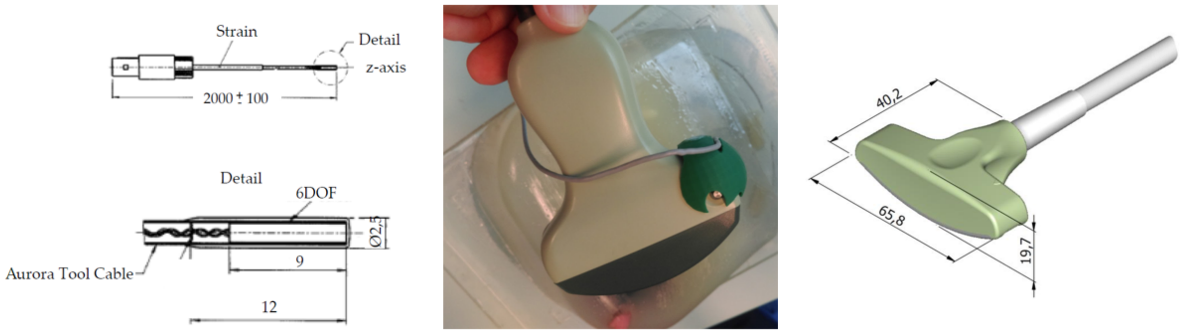

FIGURE 4.5: On the left, the Cable Tool from NDI is shown. The tip consists of the 6DOF electromagnetic sensor, attached to a 2 meter cable with a connector. In the middle picture, this Cable Tool is anchored in a 3D-printed clip-on tool, which is attached to the curved-array 8830 ultrasound transducer from BK Ultrasound. The right image shows the intraoperative transducer which will be used during liver surgery, implementation steps will be developed for this transducer type.

use during surgery due to the size and autoclave incompatibility. During the current liver navigation study, a small 6DOF EM sensor was used. Though this sensor is autoclavable and fixable on the liver surface, the wire is very fragile and rupture or clamping of this sensor caused several failures during surgery. Hence, the Cable Tool is considered as a safe and reliable for liver tracking as well. Partial compensation of liver deformation caused by the patient's breathing or surgical manipulation can be solved by fixation of this sensor in a clip-on tool that can be glued or stitched to the liver surface.

4.3.2 Development of an Automated MR-US Co-registration Method

Proceeding to the next step of MR-US co-registration can take place when the EM coordinates and orientation are continuously assigned to the live ultrasound images. For this, we want to co-register a 3D MR volume to a 3D US volume. First, a 3D ultrasound sweep is necessary. First, to construct a 3D US dataset, it is important to obtain sufficient angular data sampling of the liver from the 2D tracked US data. The US volume reconstruction method in PLUS, adopted from previous work of Gobbi and Peters [91], and Boisvert *et al*. [92], constructs a 3D Cartesian volume from a set of 2D US frames that are sweeping across a region. First, the 2D image slices are inserted into a 3D volume, by placing each pixel of all 2D slices into a volume voxel. Second, hole filling takes place since the acquired 2D slices may vary in orientation and spacing. While acquisition of the 2D US slices may vary in orientation and the spacing between them, the reconstructed 3D US volume has uniform spacing along each axis.

Instead of the manual point-based or plane-based methods, during surgery automatic MR-US co-registration is preferred. In the case of intermodality registration, there is no simple relationship between the intensities in the US image and the MR image. In literature, the use of intramodal similarity measures are described for intermodality co-registration, e.g., remapping intensities of modality A to the intensities of modality B or registration based on intensity ridges from scale-space derivatives [93]. These methods cannot easily be applied to the case of MR-US co-registration due to the big differences in image quality and presence of noise. An important similarity that is used, is the presence of circular and tubular structures in both MR and US images. Though, there is no single segmentation method that can extract the vasculature from every medical image modality.

In 2D US images the vessel extraction can take place by different mathematical methods of circular or ellipsoid detection [94]. However, preferred is to extract ellipsoid structures in our reconstructed 3D US volume instead of in 2D slices. To achieve this, a multiscale Hessian-based vesselness filter developed by Frangi *et al*. will be used [95]. A Hessian matrix describes the second-order structure of local intensity variations around each point in the image. Therewith, the vesselness filter makes a distinction between line-like, blob-like and plate-like structures by observing the relationships between the eigenvalues of the Hessian matrix in each voxel of the volume. The vesselness measure that is obtained by this filter is based on all eigenvalues of the Hessian matrices. This method is already used, e.g. for vessel extraction in MRI images for electroporation which resulted in sufficient detection compared to manual vessel segmentation by an expert radiologist [96]. As a final step, matching takes place after matching the US extracted vessel tree to the MR extracted vessel tree. The extracted vessel trees can be co-registered with the help of their centerlines, as performed by Bauer *et al*. [97] and Alhonnoro *et al*. [98]. The optimal co-registration is accomplished by minimizing the RMSE between centerlines of the vessels in the US and MR datasets, performed by an iterative algorithm. The additional time of this automatic registration for intraoperative application needs to be low with respect to the total surgery time. Initial expectation is that an acceptable registration accuracy is possible within a 4.0x4.0x4.0 cm volume of liver parenchyma.

Normally, the ultrasound image is continuously shown on ultrasound device while the surgeon moves the transducer over the liver surface. When co-registration has taken place, we want to continuously show the co-registered MR image as well. To that end, it is useful to display both these images on secondary screens that are mounted on the OR ceiling pendants with the possibility to position as one prefers. The same is done during navigation surgery procedures of current studies in this institute, where the visual software output is shown on monitors positioned at the cranial side of the patient (Figure 4.6). The way of displaying the co-registration must be intuitive for the surgeon the interpret, i.e., the interface must not be too complex.

In the ongoing navigation surgery studies in this institute, a preoperative MR or CT scan is co-registered to an intraoperative cone-beam CT scan. Delineations of a 3D segmentation model based on this preoperative scan are intraoperatively shown, superimposed on the corresponding scan in in-house developed software. With help of EM tracking, the surgeon is provided with the location of a surgical tool with respect to the location in the scan [44]. During the intraoperative use of this software, a screen shows an interface consisting of four quadrants: an axial, sagittal and coronal slice of the co-registered volume, and a fourth quadrant with a 3D rendering of the tracked surgical tool. The real-time location of the tip of a tracked EM pointer is visible in the quadrants (Figure 4.6). This current setup of information is already intuitive for the surgeons who have used it, however, this exact way of representation is advised differently in the case of US-based navigation. If we would continue with this software in exactly the same way with US-based navigation, it would be required to use the ultrasound transducer in the exact axial, coronal or sagittal views to use the preoperative data. This would not only be a difficult but also inconvenient and restricting way of using the ultrasound transducer. Therefore, an interface such as the visual output of PercuNav is advised as shown previously throughout this work. The interface for the surgeon needs to consist of at least the live ultrasound image and the co-registered MR slice right next to it. For that, the co-registered MR volume needs to undergo interpolation between slices when the ultrasound transducer is positioned under different angles (Figure 4.7). Additionally, a fusion image might be of added value, with the ultrasound image transparently projected on top of the co-registered MR image.

These images must be displayed to the surgeons during surgery. In-house development of 3D segmentation of the liver is expected to contribute to the surgeons by making preoperative information directly available [99]. The delineations of 3D segmentation models are already used during other pelvic, colorectal and liver navigation surgery studies [44, 100]. Superimposition on the axial, coronal and sagittal slices as in these studies demonstrated additional value, therefore, superimposition of delineations on top of the co-registered MR scan is expected to be of additional value. Next to that, the positioning of the ultrasound transducer with respect to the preoperative model (based on a preoperative scan) gives an indication if the performed co-registration is successful and makes sense orientation-wise. Therefore, a 3D rendering of the segmentation model with a rendering of the ultrasound transducer must be possible (Figure 4.8).

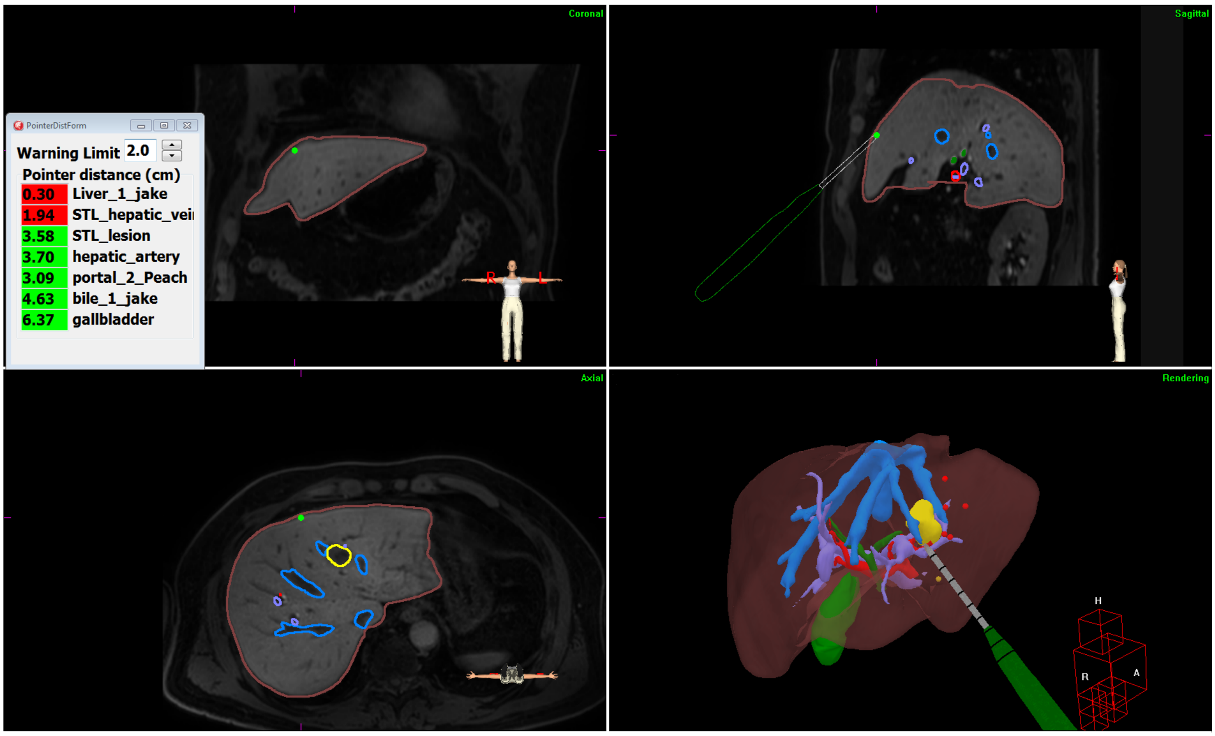

FIGURE 4.6: A screenshot of the current navigation software during tracking of a liver lesion. After acquisition of the intraoperative cone-beam CT and accepted registration, a 3D model and its delineations on top of the co-registered MR are shown. The location and orientation of the surgical tool with respect to the model are iteratively updated with help of EM tracking. Closest distances to a delineation can be shown.

To summarize, the transition to development of an in-house built system for co-registration of MR with US provides us with the freedom to select the appropriate intraoperative ultrasound transducer together with a newly developed sterilizable clip-on tool with a fixated EM sensor. An accessory benefit is the possibility to use the tabletop field generator positioned underneath the patient's mattress. A robust calibration method contributes to a safe and consistent application, after the suitable development of the clip-on tool. When the software is completed for automatic detection of vasculature in both the MR and US volumes, it is expected that automatic co-registration between the two will become possible. These steps must be tested and validated before live ultrasound combined with preoperative MR data can be used intraoperatively.

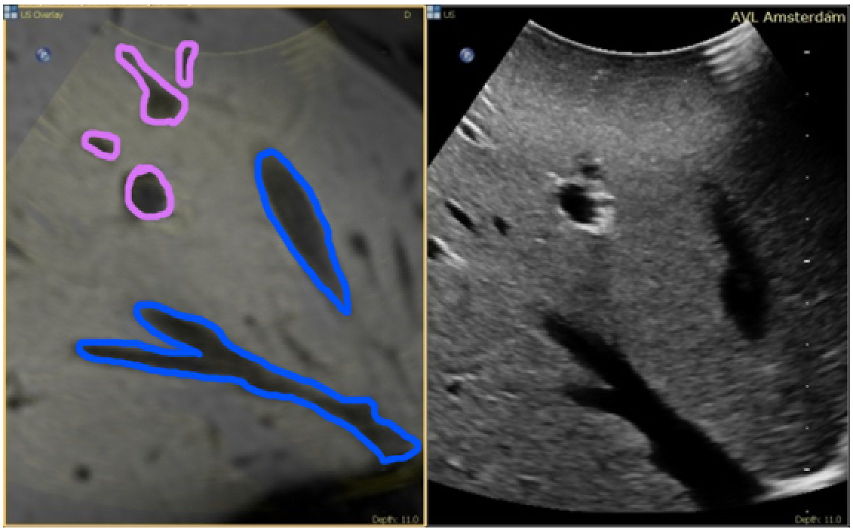

FIGURE 4.7: This image shows an alternative layout of a sketched ideal intraoperative visualization. In contrast to the previous Figure 4.8, only the live ultrasound and co-registered MR slice are shown. Delineations from the 3D model based on the MR segmentation are superimposed on the MR image (portal veins in magenta, hepatic veins in blue).

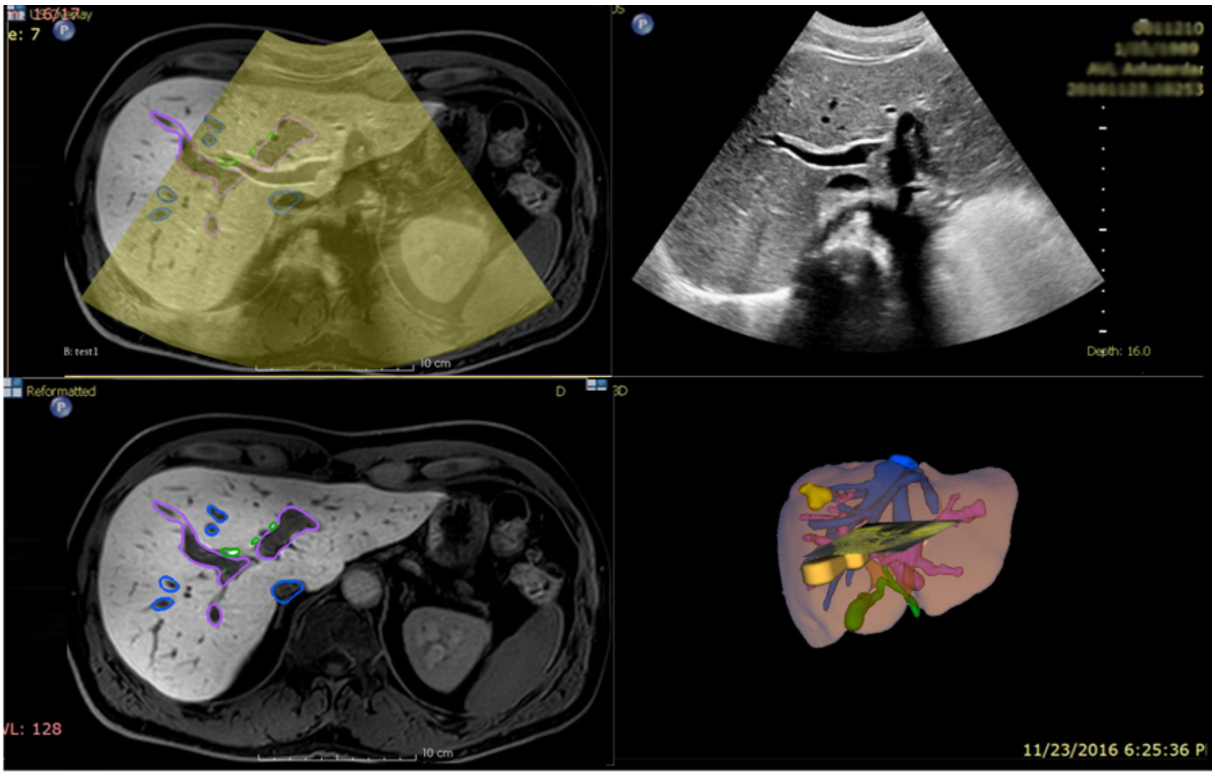

FIGURE 4.8: In here, a possible layout of to be adjusted navigation software is shown. Based on the PercuNav layout, we have an US image, co-registered MR image, fusion image and 3D rendering. Improvements are the superimposed delineations and the rendering of the 3D model instead of a rendering of the MR volume (portal veins in magenta, hepatic veins in blue, biliary ducts in green).

Chapter 5

Recommendations

Ultimately, the goal of MR-US co-registration is that the preoperative MR image will provide the surgeon with additional information since the use of solely live ultrasound does not suffice. Other institutes are exploring options for this intraoperative application as well. Beller *et al*. developed 3D US-based optoelectronic navigation for intraoperative orientation that results in parenchyma-preserving liver surgery [27]. This method, using optical tracking, did not include delineations of 3D models based on preoperative scans and was used with an abdominal (hence not a small intraoperative) probe. Banz *et al*. described the use of CAS-One liver navigation system (CASCination AG, Switzerland) for surgical removal of liver metastases [101]. This system also uses manual point-based registration and is currently lacking a robust quantitative assessment for alignment accuracy of the preoperative and intraoperative vessel trees [102]. None of these described studies are using an intuitive way of superimposed delineations. Despite the fact that they are currently further in terms of development and clinical implementation, they use optical tracking while electromagnetic tracking is preferred in this institute. Next to that, their point-based registration methods are performed manually. Li and Zhu (Hitachi, Ltd., Research & Development Group, Tokyo, Japan) have developed a machine-learning-based method to automatically co-register preoperative CT to intraoperative US [103]. In this way, they were able to co-register these volumes with a RMSE on the annotated branches of 5.8 mm while manual registration by the surgeon was noted as 11.4 mm. The described studies here show that there are possibilities for the application, though several conditions are different than the setup we aim for.

There are technical challenges to overcome. For now, it is wise to persist the development of rigid co-registration since clinical validation of non-rigid registration is a very challenging task in itself. Additionally, this has not been reviewed as fully reliable in literature [104]. Updating the preoperative 3D model with knowledge of the deformation, after quantification of this by a 3D swipe, might be of additional value. For that, elasticity scans of the liver might be useful as well. Next to the challenge to overcome deformation issues, Lange *et al.* encountered problems with development of a reliable automatic vessel segmentation from US that caused the need to manually match vessel branches during surgery [29]. A safe and reliable method is essential before automatic vessel-based registration is possible.

Investigating the possible application of this thesis' subject was described for purposes in open surgery. These open procedures are now often preferred as described earlier (Sec. 1.1). However, in the nearby future, the use of US-based navigation is desired for feasibility study in laparoscopic liver procedures as well. Research performed by Lange *et al.* has demonstrated that several options are available for minimally invasive surgery [105].

For development of the in-house system we can take into account from previous research that it is realistic to develop and apply such a system for intraoperative use. The other research groups demonstrated their possibilities, as well as their pitfalls. For the in-house system of this institute, we have set the same demands, though it will be constructed with other components. Experience and good results with the navigation software is present in this institute, what can be taken into account since the same EMTS will be used as in ongoing studies. With this good framework as a starting point, we can continue working with the rigid transformations for now.

In this institute, the current study for navigation during liver surgery is performed by using intraoperative contrast-enhanced cone beam CT instead of radiation-free ultrasound [100]. Even though this study shows development and successful applications after approximately 20 performed navigations, there are some unsolved problems and lacks of this current setup. First of all, we clearly see that the surgical opening of the abdomen and consequently the mobilization by the surgeon, both cause substantial deformation. Therewith, it is more difficult to co-register the intraoperative scan to the preoperative scan. Second, the intraoperative use of contrast during cone beam CT did not always effectively contribute to the distinction of vessels, making vessel-based co-registration cumbersome. Other problems (e.g., a limited FOV) also caused a suboptimal image quality of the cone beam CT. Additionally, with the intraoperative cone beam CT insights of local deformation are not present.

On the contrary, these problems are absent with intraoperative ultrasound. No additional contrast is required, since all vasculature is clearly visible. All cone beam CT related problems can be neglected. While the cone beam CT only gives information about the main vasculature, thus restricting possibilities during vessel-based matching, intraoperative ultrasound gives more detailed vasculature information. The use of ultrasound gives direct information about local deformation, therewith enabling the chance of a more accurate local registration.

Primary endpoint of the current liver navigation study is the accuracy, by comparing the distances between the border of the lesion and the resection plane measured by the navigation software with the distance measured by pathology. In multiple cases, the measured distances did not correlate. The influence of deformation must be bigger than it initially was expected. Next to that, only information about the location of the tumor can be tracked if the exact location of the lesion is already known. This leads to the fact that in these performed surgeries, the location of the lesion was already recognized, while ideally the location of the lesion is retrieved with help of the surrounding anatomy. With US-based navigation, this is expected to be more feasible and of additional value.

When development of the ultrasound-based navigation system is completed, it is advised to start extensive accuracy assessments of the automatic MR-US co-registration. This is required to assure a safe and accurate deployment of such a system during surgery. Bifurcation points of the vessel centerlines can be extracted from both MR and US and used for RMSE calculation. The accuracy assessment first must take place in a controlled environment with the developed multimodal liver phantom from this research. It is advised to repeat, or possibly extend where necessary, experiments as performed in Chapter 2. With that, it is suitable to measure effects of simulated deformation on the registration accuracy. Instead of *ex vivo* experiments, accuracy assessment must be performed in the intraoperative situation (note, surgeons must not use the output of the system as guidance before validation has taken place).

Consequently, if accuracy is acceptable, a navigation study must be started to further investigate the potentially additional value. Instead of the current liver navigation study, it is expected to be of functional support in the case of finding unpalpable lesions with unknown exact localization, and additionally also in vanished or isoechoic lesions. The use of this intraoperative navigation aims for a decrease in the number of inadequate surgical removals or unsuccessful ablations. Vanishing liver metastases are an increasing problem in modern medicine due to the successful neoadjuvant treatment. Therewith, we directly aim for a decrease in recurrence rates by using this intraoperative US-based navigation techniques. Additionally, the delineations of bile ducts and arteries (next to the hepatic and portal vasculature) are expected to contribute in a decrease in complications. Clinically relevant endpoints such as a shorter time of surgery, the rate of R0 resections, a decreased recurrence rate or a decrease in complications can not take place in the first studies and are reserved for later investigation.

Chapter 6

General Conclusions

This thesis posed the question to determine the feasibility of ultrasound-based navigation for surgical resection of liver lesions. Surgical navigation is needed for precise localization of liver lesions and the surrounding structures, however, conventional navigation is not applicable. Therefore, navigation for liver surgery requires real-time fusion of preoperative surgery plans (based on MR) with intra-operative ultrasound.

An in-house developed multimodal deformable liver phantom was used for accuracy measurements. Clear insights were obtained, and this has resulted in acceptable registration errors of less than 0.5 cm after point-based and plane-based registration between -2 and +2 cm from the registration center. Consequently, these measurements were performed in *ex vivo* circumstances. Despite vessel collapse and blood effusion from the resected specimens, an accurate co-registration with good matching of preoperative MR with live US was performed directly around the lesions. For proof of principle, only one intraoperative application was successfully performed.

Based on all performed experiments, it is concluded that ultrasound-based navigation by means of electromagnetic tracking is possible and shows feasibility for its intraoperative introduction during open liver surgery. During this research, the only available option to test the feasibility was the PercuNav system, in which several shortcomings are demonstrated during all experiments. This has impeded implementation of a complete ultrasound-based navigation routine at this moment. It is decided is to start the development of an alternative system, for which development steps have been described. Before intraoperative introduction can take place, validation of the described components must have been performed. Intraoperative introduction of an improved system, as it will be developed, is expected to give satisfactory accuracy of 5-10 mm in a 4.0x4.0x4.0 cm volume as is demonstrated with the current setup. In this way, the use of a rigid transformation of an MR to an US volume is expected to be sufficient and reliable after careful and controlled mobilization of the liver.

Appendix A

Appendix A - Pseudo codes

A.1 Post-processing, Matlab pipeline

These steps were performed during the 3D RMSE calculations in the phantom and *ex vivo* experiments, after manual selection of useful fiducials.

1. Choose fiducials in US and CT/MR
2. Translate xy-coordinates of CT/MR window to US window
3. Determine the two outer points of the fiducial sets
4. Find z-coordinate of these points in original CT/MR volume
5. Normalize all fiducial z-coordinates between these two z-coordinates
6. Determine cm/pixel scale; rescale fiducials to cm
7. Calculate Euclidean distance between all fiducial pairs

A.2 2.5D RMSE post-processing with SIFT algorithm

These steps were performed during the 2.5D RMSE calculations in the *ex vivo* experiments, after semi-automatic detection of points pairs by an adjusted SIFT algorithm.

1. Load volume V
2. Select lowest and highest boundaries
   For US images (US_L and US_H)
   For MR images (MR_L and MR_H)
3. For m = US_L : 15 : US_H
   Select US slice from volume V
   Apply median filter
   End
4. For n = MR_L : 5 : MR_H
   Select MR slice from volume V
   Select co-registered US slice from volume V
   Apply sharpening filter
   End
5. Check for matching SIFT pairs between all possible combinations of slices:
   For m=US_L : 15 : US_H
   For MR_L : 5 : MR_H
   Calculate SIFT features in both images
   If UBCmatch algorithm detects match
   Store match
   End
   End
   End
6. Manually check if match is acceptable
   If *false*:
   Discard match
   If *true*:
   Find z-coordinate in original volume For
   Match point in MR
   Match point in co-registered MR that corresponds to US
   End
   End
7. Calculate RMSE

Appendix B

Appendix B - Accepted SIFT Pairs

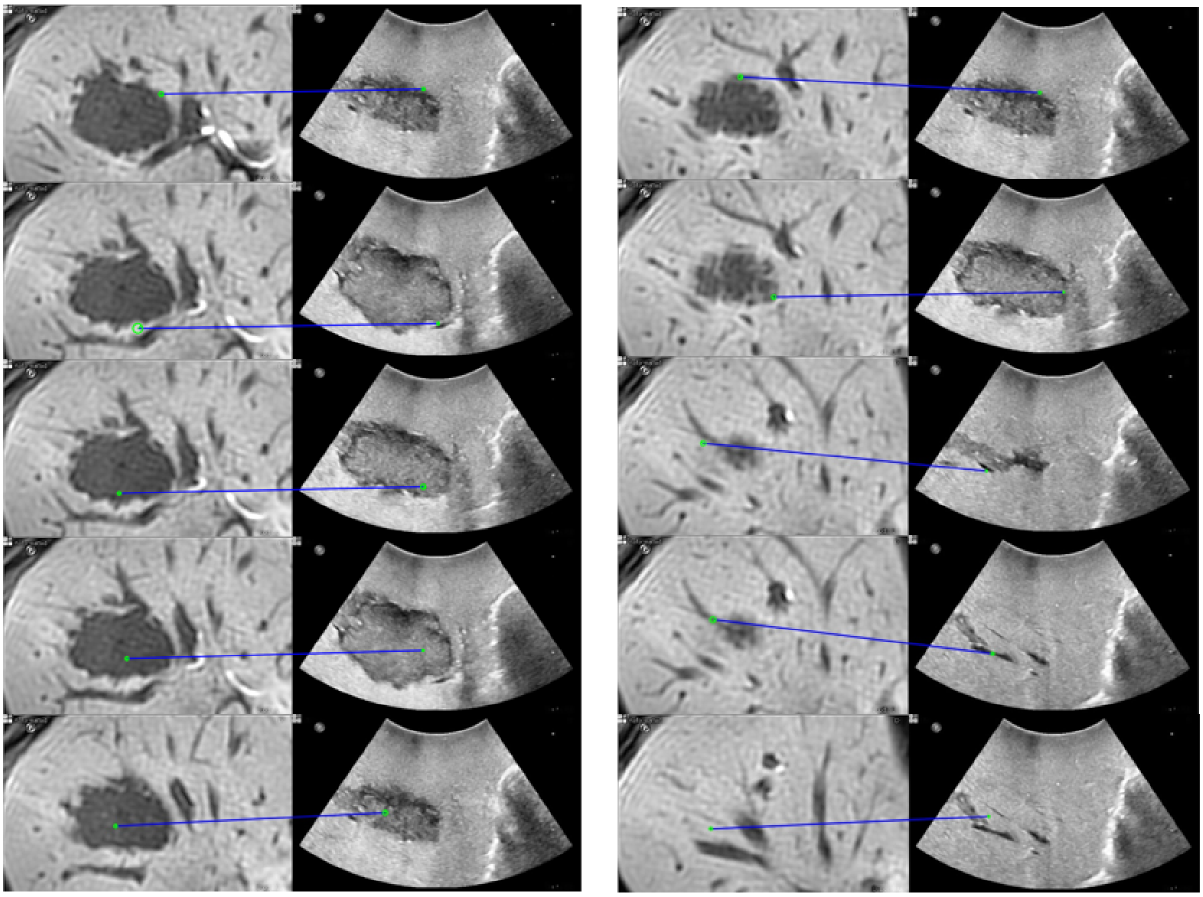

FIGURE B.1: Ten pairs of found SIFT features that were accepted by visual inspection after the SIFT algorithm. The blue line connects the found feature in the MR slice with the found feature in the US slice.

Bibliography

[1] E. Van Cutsem, A. Cervantes, B. Nordlinger, and D. Arnold, "Metastatic colorectal cancer: ESMO Clinical Practice Guidelines for diagnosis, treatment and follow-up.", *Annals of oncology : Official journal of the European Society for Medical Oncology / ESMO*, vol. 25 Suppl 3, no. suppl 3, pp. iii1–9, 2014.

[2] U. Stein and P. M. Schlag, "Clinical, biological, and molecular aspects of metastasis in colorectal cancer.", *Recent results in cancer research. Fortschritte der Krebsforschung. Progrès dans les recherches sur le cancer*, vol. 176, pp. 61–80, 2007.

[3] N. Kemeny and F. Fata, "Arterial, portal, or systemic chemotherapy for patients with hepatic metastasis of colorectal carcinoma", *J Hepatobiliary Pancreat Surg*, vol. 6, no. 1, pp. 39–49, 1999.

[4] B. E. Van Beers, C. M. Pastor, and H. K. Hussain, "Primovist, eovist: What to expect?", *Journal of Hepatology*, vol. 57, no. 2, pp. 421–429, 2012.

[5] M. H. Lee, S. H. Kim, M. J. Park, C. K. Park, and H. Rhim, "Gadoxetic acid-enhanced hepatobiliary phase MRI and high-b-value diffusion-weighted imaging to distinguish well-differentiated hepatocellular carcinomas from benign nodules in patients with chronic liver disease", *American Journal of Roentgenology*, vol. 197, no. 5, 2011.

[6] R. Hammerstingl, A. Huppertz, J. Breuer, T. Balzer, A. Blakeborough, R. Carter, L. C. Fusté, G. Heinz-Peer, W. Judmaier, M. Laniado, R. M. Manfredi, D. G. Mathieu, D. Müller, K. Mortelè, P. Reimer, M. F. Reiser, P. J. Robinson, K. Shamsi, M. Strotzer, M. Taupitz, B. Tombach, G. Valeri, B. E. Beers, and T. J. Vogl, "Diagnostic efficacy of gadoxetic acid (Primovist)-enhanced MRI and spiral CT for a therapeutic strategy: Comparison with intraoperative and histopathologic findings in focal liver lesions", *European Radiology*, vol. 18, no. 3, pp. 457–467, 2008.

[7] J. H. Yoon, J. M. Lee, M. H. Yu, E. J. Kim, J. K. Han, and B. I. Choi, "Fat-suppressed, three-dimensional T1-weighted imaging using high-acceleration parallel acquisition and a dual-echo Dixon technique for gadoxetic acid-enhanced liver MRI at 3 T.", *Acta Radiologica*, 2014.

[8] J. Huiskens, T. M. van Gulik, K. P. van Lienden, M. R. W. Engelbrecht, G. A. Meijer, N. C. T. van Grieken, J. Schriek, A. Keijser, L. Mol, I. Q. Molenaar, C. Verhoef, K. P. de Jong, K. H. C. Dejong, G. Kazemier, T. M. Ruers, J. H. W. de Wilt, H. van Tinteren, and C. J. A. Punt, *Treatment strategies in colorectal cancer patients with initially unresectable liver-only metastases, a study protocol of the randomised phase 3 CAIRO5 study of the Dutch Colorectal Cancer Group (DCCG).* 2015.

[9] T. C. Chua, A. Saxena, W. Liauw, A. Kokandi, and D. L. Morris, "Systematic review of randomized and nonrandomized trials of the clinical response and outcomes of neoadjuvant systemic chemotherapy for resectable colorectal liver metastases.", *Annals of surgical oncology*, vol. 17, no. 2, pp. 492–501, 2010.

[10] G. D. Leonard, "Neoadjuvant Chemotherapy Before Liver Resection for Patients With Unresectable Liver Metastases From Colorectal Carcinoma", *Journal of Clinical Oncology*, vol. 23, no. 9, pp. 2038–2048, 2005.

[11] R. C. Auer, R. R. White, N. E. Kemeny, L. H. Schwartz, J. Shia, L. H. Blumgart, R. P. Dematteo, Y. Fong, W. R. Jarnagin, and M. I. D'Angelica, "Predictors of a true complete response among disappearing liver metastases from colorectal cancer after chemotherapy", *Cancer*, vol. 116, no. 6, pp. 1502–1509, 2010.

[12] M. G. van Vledder, M. C. de Jong, T. M. Pawlik, R. D. Schulick, L. A. Diaz, and M. A. Choti, "Disappearing Colorectal Liver Metastases after Chemotherapy: Should we be Concerned?", *Journal of Gastrointestinal Surgery*, vol. 14, no. 11, pp. 1691–1700, 2010.

[13] M. Høyer, A. Swaminath, S. Bydder, M. Lock, A. Méndez Romero, B. Kavanagh, K. A. Goodman, P. Okunieff, and L. A. Dawson, "Radiotherapy for liver metastases: A review of evidence", *International Journal of Radiation Oncology Biology Physics*, vol. 82, no. 3, pp. 1047–1057, 2012.

[14] P. Liang, Y. Wang, X. Yu, and B. Dong, "Malignant liver tumors: treatment with percutaneous microwave ablation–complications among cohort of 1136 patients.", *Radiology*, vol. 251, no. 3, pp. 933–940, 2009.

[15] K. T. Nguyen, T. C. Gamblin, and D. A. Geller, "World review of laparoscopic liver resection-2,804 patients.", *Annals of surgery*, vol. 250, no. 5, pp. 831–41, 2009.

[16] S. L. Wong, P. B. Mangu, M. a. Choti, T. S. Crocenzi, G. D. Dodd, G. S. Dorfman, C. Eng, Y. Fong, A. F. Giusti, D. Lu, T. a. Marsland, R. Michelson, G. J. Poston, D. Schrag, J. Seidenfeld, and A. B. Benson, "American Society of Clinical Oncology 2009 clinical evidence review on radiofrequency ablation of hepatic metastases from colorectal cancer.", *Journal of clinical oncology : Official journal of the American Society of Clinical Oncology*, vol. 28, no. 3, pp. 493–508, 2010.

[17] X. J. Cai, J. Yang, H. Yu, X. Liang, Y. F. Wang, Z. Y. Zhu, and S. Y. Peng, "Clinical study of laparoscopic versus open hepatectomy for malignant liver tumors.", *Surgical endoscopy*, vol. 22, no. 11, pp. 2350–6, 2008.

[18] C. Simillis, V. A. Constantinides, P. P. Tekkis, A. Darzi, R. Lovegrove, L. Jiao, and A. Antoniou, "Laparoscopic versus open hepatic resections for benign and malignant neoplasms - a meta-analysis", *Surgery*, vol. 141, no. 2, 2007.

[19] C. Charnsangavej, B. Clary, Y. Fong, A. Grothey, T. M. Pawlik, and M. A. Choti, "Selection of Patients for Resection of Hepatic Colorectal Metastases: Expert Consensus Statement", *Annals of surgical oncology*, vol. 13, no. 10, pp. 1261–1268, 2006.

[20] J. S. Gold, C. Are, P. Kornprat, W. R. Jarnagin, M. Gonen, Y. Fong, R. P. DeMatteo, L. H. Blumgart, and M. D'Angelica, "Increased use of parenchymal-sparing surgery for bilateral liver metastases from colorectal cancer is associated with improved mortality without change in oncologic outcome: trends in treatment over time in 440 patients.", *Annals of Surgery*, vol. 247, no. 1, pp. 109–117, 2008.

[21] R. Smithuis and E. E. D. Lange, *Anatomy of the liver segments*. [Online]. Available: `http://www.radiologyassistant.nl/en/p4375bb8dc241d/anatomy-of-the-liver-segments.html` (visited on 05/01/2017).

[22] W. R. Jarnagin, M. Gonen, Y. Fong, R. P. DeMatteo, L. Ben-Porat, S. Little, C. Corvera, S. Weber, and L. H. Blumgart, "Improvement in perioperative outcome after hepatic resection: analysis of 1,803 consecutive cases over the past decade.", *Annals of surgery*, vol. 236, no. 4, 397–406; discussion 406–7, 2002.

[23] J. Belghiti, R. Noun, R. Malafosse, P. Jagot, A. Sauvanet, F. Pierangeli, J. Marty, and O. Farges, "Continuous versus intermittent portal triad clamping for liver resection: A controlled study.", *Annals of surgery*, vol. 229, no. 3, p. 369, 1999.

[24] J. Belghiti, R. Noun, E. Zante, T. Ballet, and A. Sauvanet, “Portal triad clamping or hepatic vascular exclusion for major liver resection. A controlled study.”, *Annals of surgery*, 1996.

[25] N. N. Rahbari, M. N. Wente, P. Schemmer, M. K. Diener, K. Hoffmann, E. Motschall, J. Schmidt, J. Weitz, and M. W. Büchler, “Systematic review and meta-analysis of the effect of portal triad clamping on outcome after hepatic resection”, *British Journal of Surgery*, 2008.

[26] T. M. Pawlik, R. D. Schulick, and M. a. Choti, “Expanding criteria for resectability of colorectal liver metastases.”, *The oncologist*, vol. 13, no. 1, pp. 51–64, 2008.

[27] S. Beller, M. Hünerbein, T. Lange, S. Eulenstein, B. Gebauer, and P. M. Schlag, “Image-guided surgery of liver metastases by three-dimensional ultrasound-based optoelectronic navigation”, *British Journal of Surgery*, vol. 94, no. 7, pp. 866–875, 2007.

[28] O. Heizmann, S. Zidowitz, H. Bourquain, S. Potthast, H. O. Peitgen, D. Oertli, and C. Kettelhack, “Assessment of intraoperative liver deformation during hepatic resection: Prospective clinical study”, *World Journal of Surgery*, vol. 34, no. 8, pp. 1887–1893, 2010.

[29] T. Lange, N. Papenberg, S. Heldmann, J. Modersitzki, B. Fischer, H. Lamecker, and P. M. Schlag, “3D ultrasound-CT registration of the liver using combined landmark-intensity information”, *International Journal of Computer Assisted Radiology and Surgery*, vol. 4, no. 1, pp. 79–88, 2009.

[30] D. M. Cash, M. I. Miga, S. C. Glasgow, B. M. Dawant, L. W. Clements, Z. Cao, R. L. Galloway, and W. C. Chapman, “Concepts and preliminary data toward the realization of image-guided liver surgery”, *Journal of Gastrointestinal Surgery*, vol. 11, no. 7, pp. 844–859, 2007.

[31] M. Hayashibe, N. Suzuki, S. Kobayashi, N. Nakata, A. Hattori, and Y. Nakamura, “Development of a 3D visualization system for surgical field deformation with geometric pattern projection.”, *Studies in health technology and informatics*, vol. 111, pp. 172–7, 2005.

[32] D. K. Bae and S. J. Song, “Computer assisted navigation in knee arthroplasty”, *Clinics in Orthopedic Surgery*, vol. 3, no. 4, pp. 259–267, 2011.

[33] I. D. Gelalis, N. K. Paschos, E. E. Pakos, A. N. Politis, C. M. Arnaoutoglou, A. C. Karageorgos, A. Ploumis, and T. a. Xenakis, “Accuracy of pedicle screw placement: a systematic review of prospective in vivo studies comparing free hand, fluoroscopy guidance and navigation techniques”, *European Spine Journal*, vol. 21, no. 2, pp. 247–255, 2012.

[34] P. Grunert, K. Darabi, J. Espinosa, and R. Filippi, “Computer-aided navigation in neurosurgery”, *Neurosurgical Review*, vol. 26, no. 2, pp. 73–99, 2003.

[35] C. Senft, C. T. Ulrich, V. Seifert, and T. Gasser, “Intraoperative magnetic resonance imaging in the surgical treatment of cerebral metastases”, *Journal of Surgical Oncology*, vol. 101, no. 5, pp. 436–441, 2010.

[36] M. J. Zinser, H. F. Sailer, L. Ritter, B. Braumann, M. Maegele, and J. E. Zöller, “A paradigm shift in orthognathic surgery? A comparison of navigation, computer-aided designed/computer-aided manufactured splints, and "classic" intermaxillary splints to surgical transfer of virtual orthognathic planning”, *Journal of Oral and Maxillofacial Surgery*, vol. 71, no. 12, 2013.

[37] A. Ferrero, S. Langella, F. Giuliante, L. Viganò, M. Vellone, G. Zimmitti, F. Ardito, G. Nuzzo, and L. Capussotti, “Intraoperative liver ultrasound still affects surgical strategy for patients with colorectal metastases in the modern era”, *World Journal of Surgery*, vol. 37, no. 11, pp. 2655–2663, 2013.

[38] S. Jin, Q. Fu, G. Wuyun, and T. Wuyun, “Management of post-hepatectomy complications”, *World Journal of Gastroenterology*, vol. 19, no. 44, pp. 7983–7991, 2013.

[39] H. Rhim and H. K. Lim, “Radiofrequency ablation of hepatocellular carcinoma: Pros and cons”, *Gut and Liver*, vol. 4, no. SUPPL. 1, 2010.

[40] M. C. Russell, “Complications following hepatectomy”, *Surgical Oncology Clinics of North America*, vol. 24, no. 1, pp. 73–96, 2015.

[41] G. Mauri, L. Cova, S. De Beni, T. Ierace, T. Tondolo, A. Cerri, S. N. Goldberg, and L. Solbiati, “Real-Time US-CT/MRI Image Fusion for Guidance of Thermal Ablation of Liver Tumors Undetectable with US: Results in 295 Cases”, *CardioVascular and Interventional Radiology*, vol. 38, no. 1, pp. 143–151, 2014.

[42] H. Neshat, D. W. Cool, K. Barker, L. Gardi, N. Kakani, and A. Fenster, “A 3D ultrasound scanning system for image guided liver interventions”, *Medical physics*, vol. 40, no. 11, p. 112 903, 2013.

[43] J. Nijkamp, B. Schermers, S. Schmitz, S. de Jonge, K. Kuhlmann, F. van der Heijden, J.-J. Sonke, and T. Ruers, “Comparing position and orientation accuracy of different electromagnetic sensors for tracking during interventions”, *International Journal of Computer Assisted Radiology and Surgery*, vol. 11, no. 8, pp. 1487–1498, 2015.

[44] J. Nijkamp, K. Kuhlmann, J.-J. Sonke, and T. Ruers, “Image-guided navigation surgery for pelvic malignancies using electromagnetic tracking and intra-operative imaging”, *International Journal of Computer Assisted Radiology and Surgery*, vol. 11, no. 1, S107–S108, 2016.

[45] *Philips White Paper - Autoregistration brings simplicity to image fusion.pdf*.

[46] F. Kral, E. J. Puschban, H. Riechelmann, and W. Freysinger, “Comparison of optical and electromagnetic tracking for navigated lateral skull base surgery”, *International Journal of Medical Robotics and Computer Assisted Surgery*, vol. 9, no. 2, pp. 247–252, 2013.

[47] NDI, *Aurora EM Tracking System*. [Online]. Available: `http://www.ndigital.com/medical/wp-content/uploads/sites/4/2013/12/Aurora.pdf` (visited on 11/01/2016).

[48] J. Yoo, S. Schafer, A. Uneri, Y. Otake, A. J. Khanna, and J. H. Siewerdsen, “An electromagnetic "tracker-in-Table" configuration for X-ray fluoroscopy and cone-beam CT-guided surgery”, *International Journal of Computer Assisted Radiology and Surgery*, vol. 8, no. 1, pp. 1–13, 2013.

[49] T. J. Ward, R. E. Goldman, and J. L. Weintraub, “Electromagnetic navigation with multimodality image fusion for image-guided percutaneous interventions”, *Techniques in Vascular and Interventional Radiology*, vol. 16, no. 3, pp. 177–181, 2013.

[50] K Krissian, G Malandain, N Ayache, R Vaillant, and Y Trousset, “Model-Based Detection of Tubular Structures in 3D Images”, *Computer Vision and Image Understanding*, vol. 80, no. 2, pp. 130–171, 2000.

[51] J. B. Maintz and M. A. Viergever, “A survey of medical image registration.”, *Medical image analysis*, vol. 2, no. 1, pp. 1–36, 1998.

[52] J. McGrath, D. N. Siegel, and D. L. Waldman, “Ultrasonography and GPS technology”, *Ultrasound Clinics*, vol. 8, no. 2, pp. 201–212, 2013.

[53] D. G. Lowe, “Distinctive image features from scale-invariant keypoints”, *International journal of computer vision*, vol. 60, no. 2, pp. 91–110, 2004.

[54] T. Lindeberg, “Scale-space theory: a basic tool for analyzing structures at different scales”, *Journal of Applied Statistics*, vol. 21, no. 1, pp. 225–270, 1994.

[55] K. Mikolajczyk, K. Mikolajczyk, C. Schmid, and C. Schmid, "A performance evaluation of local descriptors", *IEEE Transactions on Pattern Analysis and Machine Intelligence*, vol. 27, no. 10, pp. 1615–1630, 2005.

[56] Z. Ghassabi, J. Shanbehzadeh, A. Sedaghat, and E. Fatemizadeh, "An efficient approach for robust multimodal retinal image registration based on UR-SIFT features and PIIFD descriptors", *EURASIP Journal on Image and Video Processing*, vol. 2013, no. 1, p. 25, 2013.

[57] S. W. Teng, M. T. Hossain, and G. Lu, "Multimodal image registration technique based on improved local feature descriptors", *Journal of Electronic Imaging*, vol. 24, no. 1, p. 13, 2015.

[58] M. Brown and D. G. Lowe, "Invariant Features from Interest Point Groups", *In British Machine Vision Conference*, pp. 656–665, 2002.

[59] M. O. Culjat, D. Goldenberg, P. Tewari, and R. S. Singh, "A review of tissue substitutes for ultrasound imaging", *Ultrasound in Medicine and Biology*, vol. 36, no. 6, pp. 861–873, 2010.

[60] B. W. Pogue and M. S. Patterson, "Review of tissue simulating phantoms for optical spectroscopy, imaging and dosimetry", *Journal of Biomedical Optics*, vol. 11, no. 4, pp. 041 102–041102–16, 2006.

[61] L. C. Cabrelli, P. I.B.G. B. Pelissari, L. P. Aggarwal, A. M. Deana, A. a. O. Carneiro, and T. Z. Pavan, "Oil-based gel phantom for ultrasound and optical imaging", *Proc. of SPIE, Opto-Acoustic Methods and Applications in Biophotonics II*, vol. 9531, p. 95310L, 2015.

[62] K. J. M. Surry, H. J. B. Austin, A Fenster, and T. M. Peters, "Poly(vinyl alcohol) cryogel phantoms for use in ultrasound and MR imaging", *Physics in Medicine and Biology*, vol. 49, no. 24, pp. 5529–5546, 2004.

[63] A. Hellerbach, V. Schuster, A. Jansen, and J. Sommer, "MRI Phantoms - Are There Alternatives to Agar?", *PLoS ONE*, vol. 8, no. 8, 2013.

[64] T. Ungi, G. Gauvin, A. Lasso, C. T. Yeo, P. Pezeshki, T. Vaughan, K. Carter, J. Rudan, C. J. Engel, and G. Fichtinger, "Navigated Breast Tumor Excision Using Electromagnetically Tracked Ultrasound and Surgical Instruments", *IEEE Transactions on Biomedical Engineering*, vol. 63, no. 3, pp. 600–606, 2016.

[65] Materialise, *Datasheet Laser Sintering Materials Properties TPU 92A-1*. [Online]. Available: `https://i.materialise.com/3d-printing-materials/rubber-like/technical-specifications` (visited on 11/02/2016).

[66] Philips, "mDIXON being developed to simplify and accelerate MRI", *Field Strength issue*, no. 41, pp. 31–33, 2010.

[67] J. Krücker, S. Xu, A. Venkatesan, J. K. Locklin, H. Amalou, N. Glossop, and B. J. Wood, "Clinical utility of real-time fusion guidance for biopsy and ablation", *Journal of Vascular and Interventional Radiology*, vol. 22, no. 4, pp. 515–524, 2011.

[68] *Tracking brackets for Philips ultrasound transducers - CIVCO Medical Solutions*. [Online]. Available: `http://civco.com/mmi/products/needle-tracking.htm` (visited on 05/13/2017).

[69] A. M. Franz, T. Haidegger, W. Birkfellner, K. Cleary, T. M. Peters, and L. Maier-Hein, *Electromagnetic tracking in medicine -A review of technology, validation, and applications*, 2014.

[70] P. Markelj, D. Tomaževič, B. Likar, and F. Pernuš, "A review of 3D/2D registration methods for image-guided interventions", *Medical Image Analysis*, vol. 16, no. 3, pp. 642–661, 2012.

[71] J. Much, "Error Classification and Propagation for Electromagnetic Tracking", p. 102, 2008.

[72] B. Zitová and J. Flusser, "Image registration methods: A survey", *Image and Vision Computing*, vol. 21, no. 11, pp. 977–1000, 2003.

[73] L. Crocetti, R. Lencioni, S. Debeni, T. C. See, C. D. Pina, and C. Bartolozzi, "Targeting liver lesions for radiofrequency ablation: an experimental feasibility study using a CT-US fusion imaging system.", *Investigative radiology*, vol. 43, no. 1, pp. 33–39, 2008.

[74] C. Ewertsen, K. Ellegaard, M. Boesen, S. Torp-Pedersen, and M. Bachmann Nielsen, "Comparison of two co-registration methods for real-time ultrasonography fused with MRI: A phantom study", *Ultraschall in der Medizin*, vol. 31, no. 3, pp. 296–301, 2010.

[75] T. Wendler, M. Feuerstein, J. Traub, T. Lasser, J. Vogel, F. Daghighian, S. I. Ziegler, and N. Navab, "Real-time fusion of ultrasound and gamma probe for navigated localization of liver metastases.", *Medical image computing and computer-assisted intervention : MICCAI ... International Conference on Medical Image Computing and Computer-Assisted Intervention*, vol. 10, no. Pt 2, pp. 252–260, 2007.

[76] X. Yu, F. Liu, P. Liang, A. D. Era, Z. Cheng, and Z. Han, "Microwave ablation assisted by a computerised tomography-ultrasonography fusion imaging system for liver lesions: an ex vivo experimental study", *Int.J Hyperthermia*, vol. 27, no. 1464-5157 (Electronic), pp. 172–179, 2011.

[77] R. Czerwinski, D. Jones, and J. O'Brien W.D., "Ultrasound speckle reduction by directional median filtering", *Proceedings., International Conference on Image Processing*, vol. 1, pp. 358–361, 1995.

[78] VLFeat, *VL Feat SIFT documentation*, 2013. [Online]. Available: `http://www.vlfeat.org/matlab/vl{\_}sift.html` (visited on 05/30/2017).

[79] A. Kelman, M. Sofka, and C. V. Stewart, "Keypoint descriptors for matching across multiple image modalities and non-linear intensity variations", in *Proceedings of the IEEE Computer Society Conference on Computer Vision and Pattern Recognition*, 2007.

[80] P. Coupé, P. Hellier, C. Kervrann, and C. Barillot, "Nonlocal means-based speckle filtering for ultrasound images", *IEEE Transactions on Image Processing*, vol. 18, no. 10, pp. 2221–2229, 2009.

[81] J. Matas, O. Chum, M. Urban, and T. Pajdla, "Robust wide-baseline stereo from maximally stable extremal regions", in *Image and Vision Computing*, vol. 22, 2004, pp. 761–767.

[82] P. Scovanner, S. Ali, and M. Shah, "A 3-dimensional sift descriptor and its application to action recognition", pp. 357–360, Jan. 2007.

[83] M. Donoser and H. Bischof, "3d segmentation by maximally stable volumes (msvs)", vol. 1, pp. 63–66, Jan. 2006.

[84] C. J. Harvey and T. Albrecht, "Ultrasound of focal liver lesions", *European Radiology*, vol. 11, no. 9, pp. 1578–1593, 2001.

[85] S. Benoist, A. Brouquet, C. Penna, C. Julié, M. El Hajjam, S. Chagnon, E. Mitry, P. Rougier, and B. Nordlinger, "Complete response of colorectal liver metastases after chemotherapy: Does it mean cure?", *Journal of Clinical Oncology*, vol. 24, no. 24, pp. 3939–3945, 2006.

[86] L Maier-Hein, A. M. Franz, W Birkfellner, J Hummel, I Gergel, I Wegner, and H. P. Meinzer, "Standardized assessment of new electromagnetic field generators in an interventional radiology setting", *Med Phys*, 2012.

[87] A. Lasso, T. Heffter, A. Rankin, C. Pinter, T. Ungi, and G. Fichtinger, "PLUS: Open-source toolkit for ultrasound-guided intervention systems", *IEEE Transactions on Biomedical Engineering*, vol. 61, no. 10, pp. 2527–2537, 2014. [Online]. Available: `https://www.assembla.com/spaces/plus/wiki`.

[88] A. Lasso, T. Heffter, C. Pinter, T. Ungi, and G. Fichtinger, *PLUS applications User Manual - Project website*. [Online]. Available: `http://perk-software.cs.queensu.ca/plus/doc/nightly/user/ApplicationfCal.html` (visited on 08/01/2017).

[89] T. K. Chen, A. D. Thurston, R. E. Ellis, and P. Abolmaesumi, "A Real-Time Freehand Ultrasound Calibration System with Automatic Accuracy Feedback and Control", *Ultrasound in Medicine and Biology*, vol. 35, no. 1, pp. 79–93, 2009.

[90] Curbell Plastics Inc., *PEEK material characteristics*, 2017. [Online]. Available: `https://www.curbellplastics.com/Research-Solutions/Materials/PEEK` (visited on 08/10/2017).

[91] D. G. Gobbi and T. M. Peters, "Interactive Intra-operative 3D Ultrasound Reconstruction and Visualization", *Medical Image Computing and ComputerAssisted Intervention—MICCAI 2002*, vol. 2489, no. 2489, pp. 156–163, 2002.

[92] J. Boisvert, D. Gobbi, and S. Vikal, "An open-source solution for interactive acquisition, processing and transfer of interventional ultrasound images", *The MIDAS Journal*, pp. 1–8, 2008.

[93] D. L. Hill, P. G. Batchelor, M Holden, and D. J. Hawkes, "Medical image registration.", *Physics in Medicine and Biology*, vol. 46, no. 3, R1–R45, 2001.

[94] C. Kirbas and F. K. H. Quek, "Vessel extraction techniques and algorithms: A survey", in *Third IEEE Symposium on Bioinformatics and Bioengineering, 2003. Proceedings.*, 2003, pp. 238–245.

[95] A. F. Frangi, W. J. Niessen, K. L. Vincken, and M. a. Viergever, "Multiscale vessel enhancement filtering", *Medial Image Computing and Computer-Assisted Invervention - MICCAI'98. Lecture Notes in Computer Science, vol 1496*, vol. 1496, pp. 130–137, 1998.

[96] M. Marcan, D. Pavliha, M. M. Music, I. Fuckan, R. Magjarevic, and D. Miklavcic, "Segmentation of hepatic vessels from MRI images for planning of electroporation-based treatments in the liver.", *Radiology and oncology*, vol. 48, no. 3, pp. 267–81, 2014.

[97] C. Bauer, T. Pock, E. Sorantin, H. Bischof, and R. Beichel, "Segmentation of interwoven 3d tubular tree structures utilizing shape priors and graph cuts", *Medical Image Analysis*, vol. 14, no. 2, pp. 172–184, 2010.

[98] T. Alhonnoro, M. Pollari, M. Lilja, R. Flanagan, B. Kainz, J. Muehl, U. Mayrhauser, H. Portugaller, P. Stiegler, and K. Tscheliessnigg, "Vessel Segmentation for Ablation Treatment Planning and Simulation", in *Medical image computing and computer-assisted intervention : MICCAI International Conference on Medical Image Computing and Computer-Assisted Intervention*, vol. 6361, 2010, pp. 45–52.

[99] O. Ivashchenko, E. Rijkhorst, L. ter Beek, B. Pouw, N. Hoetjes, J. Nijkamp, K. Kuhlmann, and T. Ruers, "Automated segmentation of complete 3D liver model including arterial hepatic vasculature and biliary tree anatomy from a single multiphase MR scan", in *CARS - Computer Assisted Radiology and Surgery Proceedings of 31st International Congress and Exhibition Barcelona, Spain*, 2017, S25–S26.

[100] T. Ruers, K. Kuhlmann, J. Nijkamp, B. Pouw, and E. Klompenhouwer, *N16LNA Research protocol - Tracking of liver metastases during surgery*.

[101] V. M. Banz, P. C. Müller, P. Tinguely, D. Inderbitzin, D. Ribes, M. Peterhans, D. Candinas, and S. Weber, “Intraoperative image-guided navigation system: development and applicability in 65 patients undergoing liver surgery”, *Langenbeck's Archives of Surgery*, vol. 401, no. 4, pp. 495–502, 2016.

[102] D. Ribes, M. Peterhans, S. Anderegg, V. Banz, D. Candinas, and S. Weber, “Towards higher precision in instrument guided liver surgery: Automatic alignment of 3D ultrasound with pre-operative Mevis-CT”, *HPB*, vol. 14, p. 133, 2012.

[103] Z. Li and P. Zhu, “Liver ultrasound portal vein classification for navigation of liver-tumor resection surgery”, in *CARS - Computer Assisted Radiology and Surgery Proceedings of 31st International Congress and Exhibition Barcelona, Spain*, 2017, S101 –S102.

[104] F. P. M. Oliveira and J. M.R. S. Tavares, “Medical image registration: a review.”, *Computer methods in biomechanics and biomedical engineering*, vol. 17, no. 2, pp. 73–93, 2014.

[105] T. Langø, S. Vijayan, A. Rethy, C. Våpenstad, O. V. Solberg, R. Mårvik, G. Johnsen, and T. N. Hernes, “Navigated laparoscopic ultrasound in abdominal soft tissue surgery: Technological overview and perspectives”, *International Journal of Computer Assisted Radiology and Surgery*, vol. 7, no. 4, pp. 585–599, 2012.